Construction of Bone Anisotropic Finite Element Model from Computed Tomography (CT) Scans

By

Siamak Kazembakhshi

A thesis submitted to
the Faculty of Graduate Studies in partial fulfilment of
the requirements for the degree of
Master of Science

Department of Mechanical and Manufacturing Engineering
Faculty of Engineering
University of Manitoba
Winnipeg, Manitoba

Fall 2014

Abstract

The thesis proposes a new procedure to describe bone anisotropy in the finite element model using computed tomography (CT) images. First, bone density was correlated to CT numbers using the empirical function established in previous studies; pointwise bone density gradient was then calculated from interpolation functions of bone densities. Second, principal anisotropic directions were defined using the bone density gradient. Third, the magnitude of bone density gradient was incorporated to an existing bone elasticity-density correlation established by experiments.

A method was also introduced to assign the anisotropic material properties to finite element models in Abaqus. The effect on the predicted von Misses stresses and principal strains in the bone by adopting the anisotropic or isotropic material model was investigated by finite element simulations using Abaqus.

Acknowledgments

During my study in University of Manitoba, I have received guidance and support from a lot of people. Firstly, I would like to express my immense appreciation to my supervisor, Dr. Yunhua Luo for his support and insightful guidance in my research, his door was always open to my countless enquiries. This thesis would not have been possible without all of his guidance (and patience) along the way. I also thank him for his generous help in the non-academic area.

I would like to express my gratitude to Dr. Faisal for his help in improving the language of my thesis. I would also like to thank Masoud, Hossein, Yujia and Heng for all the academic discussion and happy time working with them. I shall extend my thanks to all my friends for their care, support and encouragement.

My thanks also go to my beloved parents for their love and great encouragement to me through all these years. Thanks to my wife Elahe for her understanding and love during the past seven years. Thank you very much for your deep love.

Contents

List of Tables

List of Figures

List of Copyrighted Material

Figure 2.2 Permission of using that figure was obtained on Jun 09, 2014.

Available from URL: http://www.eorthopod.com/content/sacral-insufficiency-fractures

Figure 2.5 Permission of using that figure was obtained on Jun 10, 2014.

Available from URL:

http://www.endolab.biz/content_detail_master.asp?sid=21006&Id=&langsel=EN

Figure 5-5 and 5-6 was cited from “San Antonio, T., et al., Orientation of orthotropic material properties in a femur FE model: A method based on the principal stresses directions. Medical Engineering & Physics. **34**(7): p. 914-919.”. The permission was obtained on September 1, 2014.

List of Symbols

$\nabla\rho$	Density Gradient
σ	Total Stress
ε	Total Strain
ν	Poisson's ratio
ρ	Bone Apparent Density
C	Compliance Tensor or Matrix
CT	CT number
D	Stiffness Tensor or Matrix
E	Young's modulus
G	shear modulus

List of Acronyms

2D	Two-Dimensional
3D	Three-Dimensional
AP	Anterior-Posterior
CT	Computed Tomography
CV(RMSE)	Coefficient of Variation of the RMSE
DV	Density Variation
FD	Finite Difference
FE	Finite Element
FEA	Finite Element Analysis
HU	Hounsfield Unit
MIL	Mean Interface Length
ML	Medial-Lateral
RMSE	Root Mean Square Error
SVD	Star Volume Density
SLD	Star Length Density
SP	Superior-Posterior

Chapter 1

Introduction

Bone is a composite living material with complex anisotropic and heterogeneous micro-structures and material properties. Anisotropic materials are stiffer when loaded along some directions than the others, and heterogeneous materials are not uniform in their material properties. The complex micro-structure of bone makes the determination of its material properties challenging. The determination of bone material properties is a prerequisite to assess bone fracture or to design implants and prostheses using numerical methods. Finite element analysis (FEA) has been widely used to computationally solve a wide range of biomedical problems such as designing artificial joints and assessing bone fracture [1-6]. The FEA is also a useful tool for the simulation of bone remodelling and healing processes [7-10]. However, the validity of FE analysis results is dependent on the accuracy of the material properties assigned to the FE models. Therefore, the definition of the precise material properties of bone is highly important for FE analyses [1, 11-20]. Consequently, development of an accurate method to describe anisotropic and heterogeneous material properties of bones has received considerable attention from researchers in the field of Biomedical and Biomechanical Engineering [21-30].

In general, most of the experimental methods such as tensile, compression, bending, torsional and indentation have been designed to characterize mechanical properties of industrial materials such as steels and composites. The aforementioned tests are also used to characterize the mechanical properties of biological materials such as wood, cartilage, bones and many others. These experimental methods are based on the fundamental principles of mechanics. Experimental studies have shown the dependence of the mechanical properties of bones on various factors, for example, species, age, sex, disease, and skeletal site [1, 26-28, 31-33]. In addition, bones have large variations in their shape and mechanical properties. Hence, bone mechanical properties change between different individuals and anatomical sites. Therefore, researches have been conducted to assess mechanical properties of *in-vivo* bones [21, 22, 27, 28]. *In-vivo* patient-specific FE analysis of bones has been also found a promising tool for fracture risk evaluation and surgery design [34-37].

Computed Tomography (CT) images contain three-dimensional (3D) information on detailed topology of the heterogeneous micro-structures of *in-vivo* bone. CT images provide a specific value for each part of bone structure corresponding to a basic unit of the CT image. The basic unit is CT voxel; and the specific number is proportional to radiodensity of the corresponding part of bone structure. The radiodensity refers to the relative inability of X-rays to pass through a particular material. The values extracted from CT images are scaled to the Hounsfield Unit (HU) using the standard procedure [26, 38-40]. The scaled value is known as the CT number. A combination of the experimental methods and statistical studies has been developed to determine the correlation between CT numbers and the heterogeneous mechanical properties of bones. For example, linear

correlations have been established between apparent bone density and CT numbers [27, 41]. Exponential and linear relations between Young's modulus and apparent bone density have been established. The defined mathematical correlations have been used to describe heterogeneous mechanical properties of *in-vivo* bones in subject-specific finite element (FE) models [26, 42, 43].

The relationships substantially differ from one to another and the source of such differences in elasticity-density relationships is unclear [43]. In addition, most of them do not consider the anisotropic behaviour of bones. In a limited number of studies anisotropy has been considered; anatomical axes, i.e., the sagittal, coronal and axial axis, have been assumed as the principal anisotropic directions [24, 26, 27, 41, 44-46]; different correlations (exponential or linear) between elasticity moduli and bone apparent density have been adopted for different anatomical directions to consider bone anisotropic behaviour [26, 27]. However, the anatomical axes may considerably deviate from the actual principal material axes (principal anisotropic directions), which may be up to 40° and cause underestimation of the elastic constants by 30–40% [43, 47]. Previous studies have shown both of the principal anisotropic directions and the elastic constants in bones may change from point to point [16, 17, 19, 48-50]. Therefore, the lack of a comprehensive description of *in-vivo* bone anisotropy may be a source of the differences in the proposed elasticity-density relationships; and it could generate considerable errors in the predicted bone mechanical behaviour. In this study, we propose a procedure to describe the anisotropy and heterogeneity of *in-vivo* bones using CT images.

The procedure consists of the following steps: (i) to define the principal anisotropic orientations; and (ii) to determine the elasticity constants along the orientations. In the

literature [1, 11, 12, 14-16], various CT based methods have been developed to find the orientations of the principal anisotropy axes. The Mean Interface Length (MIL), the Star Volume Density (SVD) and the Star Length Density (SLD) are the most frequently used methods to find the anisotropic directions of bone [1, 11-20, 41, 46, 49, 51]. These methods have mostly been used to find anisotropic directions of spongy bone because of their assumption on discontinuity of bone structure. Since these methods are very sensitive to the resolutions of the image, they are mostly applied to micro-CT images [43, 52-54]; and require high computational costs to process the large volume of micro-CT image data [17, 18]. Moreover, variations of the anisotropic orientations have not been incorporated in the magnitudes of anisotropic elasticity constants. Schneider *et al*. [55] recently developed a method known as density-variation (DV) which can be applied to both spongy and continuous structures. It has been suggested that the principal anisotropic directions are parallel to the orientations of the maximum and the minimum variation of bone apparent density at a point. The basis of this idea came from star length or star volume distribution methods. In this study, DV method was extended by defining density gradient parameter from discrete data extracted from CT images using the finite difference method. Then, the corresponding heterogeneous Young's moduli of bone in each principal anisotropic direction are modified from the existing empirical expressions. The Young's moduli are obtained by incorporating the information of the density gradient to the existing empirical functions which correlate the bone elasticity moduli and bone density. As a result, the density gradient is defined to link the principal anisotropic directions and heterogeneous magnitudes of elastic constants in each local region of the

bone. Defining a procedure to assign this anisotropic material property to a finite element (FE) model is another objective of this research.

1.1 Objective of the Reported Research

The objectives of this dissertation are as follow:

(i) To develop a new algorithm to describe pointwise anisotropy with CT scans. In the algorithm, we purpose to incorporate the effects of the pointwise anisotropy on the magnitudes of anisotropic elasticity constants. Gradient of bone density is introduced as an effective parameter to describe the pointwise anisotropic material properties of bone. For this purpose, existing empirical functions that correlate elasticity constants and bone density are improved by incorporating information of the bone density gradient.

(ii) To introduce a procedure to assign the pointwise anisotropic material properties to a finite element model.

(iii) To evaluate the effects of the anisotropy on the obtained results of bone FEAs. Fifty four finite element models are generated using both the proposed anisotropic and the conventional isotropic material models. The obtained stresses and strains distributions using both material models are then recorded and discussed.

1.2 Outline of the Reported Research

This thesis is organized as follows. In Chapter 2, first, theories of anisotropic material properties and computed tomography images are briefly explained. Second, anisotropic

behaviour of bones is reviewed. Third, conventional methods to determine principal anisotropic directions using CT images are briefly described. Fourth, possibility of extending existing density-elasticity correlations to describe bone anisotropic material properties is discussed.

In the first part of Chapter 3, a procedure is introduced to determine principal anisotropic directions using density variation. As previous experiments have established that a linear correlation exists between CT number and bone density, the proposed method uses CT numbers in place of bone density. First, a continuous function (CT function) is constructed from the discrete CT numbers. With the function the density in each voxel of CT image is considered as a variable, not a constant anymore. Then, density gradients are calculated from the constructed function. As bone density gradient is parallel to the maximum bone density variation, it represents the principal anisotropic direction at the point. Because there is no density variation in the plane normal to bone density gradient, bone behaviour in the plane (plane of isotropy) is considered isotropic. Therefore, a transversely isotropic model of material is adopted for the femur bone. The second part of Chapter 3 describes how bone density gradient is incorporated into existing empirical functions that correlate bone elasticity modulus and bone density. The new equation is obtained by modifying the empirical function and considering effects of density gradient in each voxel of CT image.

In Chapter 4, a procedure to perform FE analysis using the defined mechanical model is introduced. A measurement procedure is defined to evaluate the accuracy of the anisotropic model versus the conventional isotropic model using FE analysis.

In Chapters 5 and 6, the results of FE modeling are presented and discussed. The orientations of the isotropic plane in different sections of bone specimens are defined at the beginning of Chapter 5. The results of isotropic and anisotropic finite element simulations of virtual specimens (with the same sizes as the actual specimens used in compression tests) are also presented and discussed in this chapter.

In Chapter 6, important outcomes and the limitations of the study are discussed. Recommendations for improving the mechanical model of bone by more numerical studies and performing statistically enough experiments are discussed at the end of Chapter 6.

Chapter 2

Theory Review

This chapter explains the general theories of anisotropic material properties and computed tomography images. Then, anisotropic behaviour of bone material is reviewed; and conventional methods to describe anisotropy in bones are discussed.

2.1 Anisotropic Materials

Anisotropic materials are stiffer when loaded along some directions than the others. As opposed to isotropic materials which have identical properties in all directions, anisotropic material properties are directionally dependent [46]. The general equations for an anisotropic material are extended from the Hooke's Law. Generally, the linear elastic material behavior is defined based on the Hook's Law given by [47],

$$\sigma_{ij} = D_{ijkl}\varepsilon_{kl} \ , \tag{2.1}$$

where σ_{ij} are the components of the total stress σ, ε_{ij} are the components of the total strain ε; and D is the symmetric elastic tensor. The total stress and strain are usually written in vector form as [47]

$$\sigma = \begin{bmatrix} \sigma_{11} \\ \sigma_{22} \\ \sigma_{33} \\ \sigma_{12} \\ \sigma_{13} \\ \sigma_{23} \end{bmatrix} \text{ and } \varepsilon = \begin{bmatrix} \varepsilon_{11} \\ \varepsilon_{22} \\ \varepsilon_{33} \\ \varepsilon_{12} \\ \varepsilon_{13} \\ \varepsilon_{23} \end{bmatrix}. \tag{2.2}$$

The number of independent elastic coefficients for a general anisotropic linearly elastic material is 21. The elasticity tensor, consisting of 21 independent constants, can be written in a matrix as [56]:

$$D_{\text{Anisotropic}} = \begin{bmatrix} D_{1111} & D_{1122} & D_{1133} & D_{1112} & D_{1113} & D_{1123} \\ & D_{2222} & D_{2233} & D_{2212} & D_{2213} & D_{2223} \\ & & D_{3333} & D_{3312} & D_{3313} & D_{3323} \\ & & & D_{1212} & D_{1213} & D_{1223} \\ & Sym. & & & D_{1313} & D_{1323} \\ & & & & & D_{2323} \end{bmatrix}. \tag{2.3}$$

If two orthogonal planes of symmetry exist in the material (Figure 2.1), the material is orthotropic. If the applied load is perpendicular to one of the planes, only normal strains occur in the load direction [55]. If the elasticity tensor is transformed into the directions perpendicular to the symmetry planes, the number of elasticity constants is reduced to nine [56]. The normal orientations to the orthogonal plane are principal anisotropic directions; and the elasticity matrix has the following form:

$$D_{\text{Orthotropic}} = \begin{bmatrix} D_{11} & D_{12} & D_{13} & 0 & 0 & 0 \\ & D_{22} & D_{23} & 0 & 0 & 0 \\ & & D_{33} & 0 & 0 & 0 \\ & & & D_{1212} & 0 & 0 \\ & Sym. & & & D_{1313} & 0 \\ & & & & & D_{2323} \end{bmatrix}, \tag{2.4}$$

where $D_{ik} = D_{iikk}$.

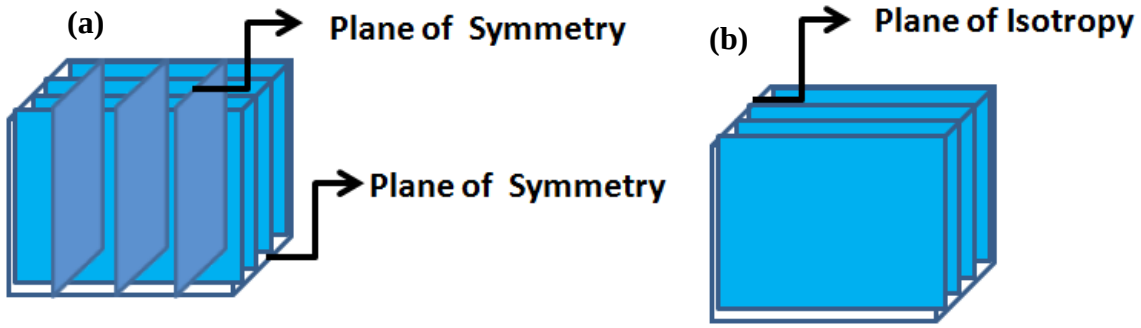

Figure 2.1: (a) Orthotropic, (b) transversely Isotropic material.

A transversely isotropic material is a special case of orthotropic materials which has a plane of isotropy. The transversely isotropic material possesses one axis of symmetry (normal to the plane of isotropy), the material properties are identical in all directions in a plane perpendicular to the axis. If a load is applied in the axis of symmetry, the material can be rotated about the axis without changing the material responses. The first principal anisotropic direction is parallel to the axis of symmetry, and the other two orthonormal anisotropic directions are arbitrary in the plane of isotropy. If the elasticity matrix is defined in the principal anisotropic directions, the number of independent coefficients decreases from nine to five for this type of material, i.e. [56],

$$D_{Transversally\_Isotropic} = \begin{bmatrix} D_{11} & D_{12} & D_{12} & 0 & 0 & 0 \\ & D_{22} & D_{23} & 0 & 0 & 0 \\ & & D_{22} & 0 & 0 & 0 \\ & & & D_{1212} & 0 & 0 \\ & Sym. & & & D_{1212} & 0 \\ & & & & & \frac{1}{2}(D_{22} - D_{23}) \end{bmatrix}. \quad (2.5)$$

An isotropic material possesses elastic properties which are independent of the orientation of the axes. Therefore, there are only two independent constants following the constitution matrix [56],

$$D_{Isotropic} = \begin{bmatrix} D_{11} & D_{12} & D_{12} & 0 & 0 & 0 \\ & D_{11} & D_{12} & 0 & 0 & 0 \\ & & D_{11} & 0 & 0 & 0 \\ & & & \frac{1}{2}(D_{11} - D_{12}) & 0 & 0 \\ & Sym. & & & \frac{1}{2}(D_{11} - D_{12}) & 0 \\ & & & & & \frac{1}{2}(D_{11} - D_{12}) \end{bmatrix}. \quad (2.6)$$

The two independent constants are the elasticity or Young's modulus, E, and the Poisson's ratio, *v*. Under a uni-axial loading condition, Young's modulus can be obtained by dividing the axial stress with the axial strain; and Poisson's ratio is the negative ratio of transverse to axial strain [56], i.e.,

$$\sigma_{11} = E\varepsilon_{11} \text{ and } \nu = -\frac{\varepsilon_{22}}{\varepsilon_{11}}. \quad (2.7)$$

The compliance tensor is the inverse of the elasticity tensor. The compliance tensor is mostly applied in engineering studies since the stress-strain relationships can be expressed in terms of Young's modulus and Poisson's ratio by using the compliance

tensor. In orthotropic and transversely isotropic material, the compliance matrixes are expressed by Young's moduli, Poisson's ratio and shear modulus in principal anisotropic directions as [56],

$$C_{Orthotropic} = \begin{bmatrix} \frac{1}{E_1} & \frac{-\nu_{12}}{E_1} & \frac{-\nu_{13}}{E_1} & 0 & 0 & 0 \\ & \frac{1}{E_2} & \frac{-\nu_{23}}{E_2} & 0 & 0 & 0 \\ & & \frac{1}{E_3} & 0 & 0 & 0 \\ & & & \frac{1}{G_{12}} & 0 & 0 \\ & Sym. & & & \frac{1}{G_{13}} & 0 \\ & & & & & \frac{1}{G_{23}} \end{bmatrix} \text{ and} \tag{2.8}$$

$$C_{Trans.Iso.} = \begin{bmatrix} \frac{1}{E_1} & \frac{-\nu_{12}}{E_1} & \frac{-\nu_{12}}{E_1} & 0 & 0 & 0 \\ & \frac{1}{E_2} & \frac{-\nu_{23}}{E_2} & 0 & 0 & 0 \\ & & \frac{1}{E_2} & 0 & 0 & 0 \\ & & & \frac{1}{G_{12}} & 0 & 0 \\ & Sym. & & & \frac{1}{G_{13}} & 0 \\ & & & & & \frac{2(1+\nu_{23})}{E_2} \end{bmatrix}. \tag{2.9}$$

The theory of anisotropic material specifies that for orthotropic or transversely isotropic materials, determination of the principal anisotropic directions is a prerequisite to define the elasticity or compliance matrix in terms of engineering constants such as Poisson's ratio, Young's modulus and shear modulus. Determination of the anisotropic

engineering constants in the principal anisotropic directions is the second step to define the elasticity or compliance matrix.

2.2 Anisotropy in bones

Bone is a living complex composite material with heterogeneous and anisotropic micro-structure [1, 57, 58]. From a macro-structure point of view, bones are classified as cortical and trabecular bone. Cortical bone is compact and has larger load bearing capacity and impact resistance. Cortical bone acts as the primary load-bearing part in femurs and tibias [59]. On the other hand, trabecular (or cancellous, spongy) bone has higher porosity and exhibits lower strength than cortical bone. Trabecular bone mainly exists in the cuboidal bones and at the ends of long bones, at places such as the trochanteric region or the knee condyles in femur bones [1]. Trabecular bone provides damping to loads and acts as an energy-absorption structure [45]. Figure 2.2 shows the micro-structure of cortical bone and trabecular bone.

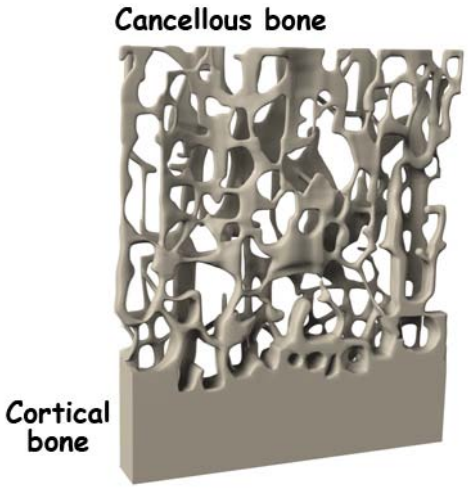

Figure 2.2: Micro-structure of trabecular and cortical bone [60].

Extensive experimental studies have been conducted to determine bones mechanical properties [25-28]. Experimental results have shown that the mechanical properties of both cortical and cancellous bones are dependent on the loading directions in experiments [26, 34, 44, 45]. For instance, experimental studies have shown that the longitudinal or weight bearing direction of long bones has the highest yield stress and Young's modulus and the radial direction has the lowest strength and elasticity modulus [23, 27, 28, 46, 61, 62]. In the other studies, different strength and elastic modulus of bone have been measured in SI (superior-interior), AP (anterior-posterior), and ML (medial-lateral) directions [26, 27]. The results showed that the mean of Young's modulus in the SI direction is about two and half times of the value in the AP direction at the mid-shaft of human femur [31].

Bone anisotropy has been extensively studied [16, 49, 50, 63-65]. Researchers have investigated the relation between bone anisotropic mechanical properties and the axial distribution of bone minerals [63, 65]. Experiments have demonstrated that more than 80% of the variance in bone mechanical behavior is related to its density variation and the anisotropy in its micro-architecture [66-68]. The effects of trabecular connectivity and morphology on the anisotropy of spongy bones have been reported in the literature [69-71]. In addition, micro-scale studies have revealed that the orientation of mineral crystals and collagen fibrils in bones is responsible for the tissue directional variation in elastic properties or cause mechanical anisotropy [59].

2.3 Computed Tomography (CT) Image

A set of CT scans of human body are a number of two-dimensional (2D) images; each 2D image represents a section of the body [1]. The movement of an X-Ray source in one direction and photographic film in opposite direction scans the image of the targeted cross-section.

Voxel is the basic unit in CT scans. The size of a voxel depends on the resolution of CT image. Data extracted from the CT images consist of a set of numbers representing the intensity of X-ray. The numbers are proportional to the X-ray absorption coefficient (radio density) [59]. Normally, the numbers are transformed linearly to a standard scale (Hounsfield Unit-HU), with the radiodensity of water at standard pressure and temperature defined as zero Hounsfield Units (HU), and the radiodensity of air at the same condition defined as -1000 HU [55].

CT images contain information of heterogeneous structures in the bone. CT images have been used for examining bone structure, geometry, destruction and remodelling during fracture healing [1, 73]. CT images have been also used for evaluating the density and the mechanical properties of bone. In addition, the information extracted from the CT images (CT number) has been used to determine bone mechanical properties. Linear correlations have been established between bone apparent density and CT numbers [27, 41]. Exponential and linear relations have been established between Young's modulus and bone apparent density [21, 22, 26].

CT based methods have been also developed to find orientations of principal anisotropic directions [1, 11, 12, 14-16]. CT numbers have been processed using different

methodologies to find preferential alignment of bone structures. The preferential alignment of bone structures is utilized to find structural anisotropic directions. The structural anisotropic directions have been found closely parallel to principal mechanical anisotropic directions [12, 20, 50, 64, 74]. The next section explains different methods to process the CT image data to find the principal anisotropic directions.

2.4 Principal Anisotropic Directions in Long Bones

In the 19th century, Meyer and Wolf *et al.* observed the influence of mechanics on bone architecture [65]. Bone structural anisotropy has been observed as the consequence of adaptive response to the applied load; and bone structure has shown preferential alignments parallel to the direction of the applied load. Based on the relation between mechanics and architecture of bone, different methods have been developed to define bone mechanical anisotropy using its structural anisotropy [12, 15, 16, 48, 49].

The link between the structural and the mechanical anisotropy of bone has been established by Cowin *et al.* [12]. The mechanical anisotropy refers to the variations of mechanical properties such as elasticity modulus or strength in different directions. The directions in the maximum and the minimum mechanical properties are taken as the principal mechanical anisotropic directions. The ratio of the maximum to the minimum elasticity modulus is called mechanical anisotropy ratio. The term of fabric tensor has been introduced to correlate structural and mechanical anisotropy. Cowin *et al.* defined fabric tensor as the inverse of the MIL (Mean Intercept Length) tensor. The degree of

anisotropy is obtained from the eigenvalues of the fabric tensor [12]. Other methods have been also developed to determine the mechanical anisotropic directions of bone by extracting information of anisotropic architecture from CT images [13, 16, 19, 20, 41, 46, 49, 51]. The common CT based measurement methods, which are used to determine the anisotropic directions, are described later in this chapter.

2.4.1 The Mean Intercept Length (MIL) Method

The MIL method has been developed by Whitehouse *et al.* to quantify the structural anisotropy of cancellous bone using CT image data. The MIL method is used to find the preferential alignment of bone structure or structural anisotropic direction in bones. The MIL method was also applied by Harrigan and Mann *et al.* to 3D objects using CT images [48, 49, 51].

The MIL method is defined as the average distance between two bone/morrow interfaces [14, 51]. Segmentation of the interfaces between phases (bone/marrow or bone/surrounding soft tissue) and construction of binary data from CT images are two important steps in the MIL method [1, 75, 76].

In the MIL method, MIL components with respect to the direction of $\vec{w}$ ($MIL(\vec{w})$) must be measured, where $\vec{w}$ is a unitary vector with an arbitrary orientation. First, a set of parallel line to the direction of $\vec{w}$ is drawn in order to measure $MIL(\vec{w})$. The number of intersections between these lines and the bone/morrow interfaces, $I(\vec{w})$, is counted (Figure 2.3(a)). Finally, the MIL component with respect to $\vec{w}$, is calculated as:

$$MIL(\vec{w}) = \frac{L}{I(\vec{w})} \ , \tag{2.10}$$

where L is the total length of all drawn lines in the orientation of $\vec{w}$. It can be seen that the values of MIL components are inversely proportional to the number of intersections between a set of parallel lines and bone/morrow interfaces [1, 48, 49].

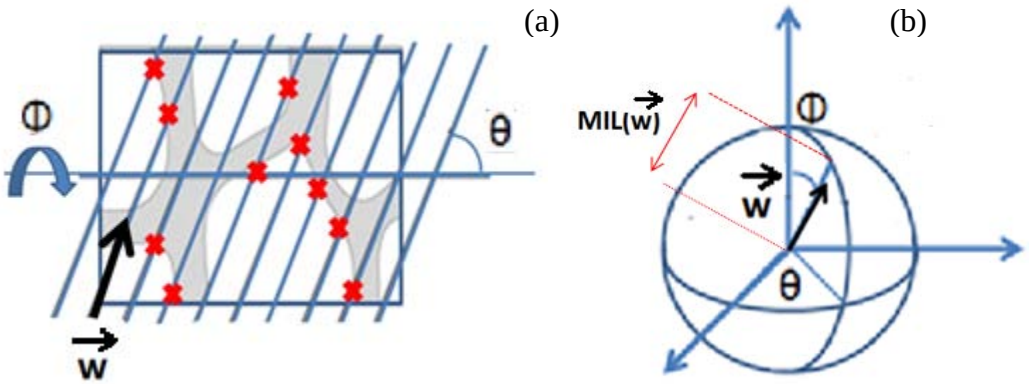

Figure 2.3:(a) The intercepts between the set of parallel lines and the interface between phases (The gray and white areas represent bone and morrow, respectively). (b) The rose diagram of MIL components for any arbitrary directions.

To obtain principal anisotropic directions and ratio, a MIL tensor is computed from MIL components. In order to obtain the MIL tensor in a two-dimensional case, the MIL components for different directions ($\vec{w}$**)** are plotted in a rose diagram. Each MIL component is plotted as a radius from the origin at the angle of measurement (the angle of $\vec{w}$). Whitehouse *et al.* have found that $MIL(\vec{w})$ in the rose diagram can be approximately represented by an ellipse equation for trabecular bone [1, 48]. Harrigan and Mann *et al.* have extended this result in the three-dimensional space and they have found that *MIL(w)* in the rose diagram could have been estimated with an ellipsoid surface equation (Figure 2.3(b)). The ellipse equation in 2D studies or the ellipsoid surface equation in 3D studies can be estimated with a small error by a fitting algorithm such as least-squares fitting [1].

The MIL tensor must be derived from the ellipse or ellipsoid equations to determine anisotropic directions and ratio in a region of interest. In 3D studies, the following

procedure has been utilized to derive the MIL tensor from the ellipsoid surface equation. The general formula of the surface of an ellipsoid is [51]:

$$\mathrm{A}x_1^2 + \mathrm{B}x_2^2 + \mathrm{C}x_3^2 + 2\mathrm{D}x_1x_2 + 2\mathrm{E}x_1x_3 + 2\mathrm{F}x_2x_3 = 1. \quad (2.11)$$

Equation (2.11) can be represented in a matrix form. Each MIL components can be plotted as a radius with respect to Cartesian coordinates by [1, 51]:

$$x_1 = MIL(\vec{w}) \times w_1 \, , x_2 = MIL(\vec{w}) \times w_2 \text{ and } x_3 = MIL(\vec{w}) \times w_3 \, , \quad (2.12)$$

where w_1, w_2 and w_3 are the dimensions of the projections of the $\vec{w}$, in the directions of Cartesian coordinates axes. Using Equation (2.12), the Equation (2.11) is rewritten as:

$$MIL(\vec{w})^2(\mathrm{A}w_1^2 + \mathrm{B}w_2^2 + \mathrm{C}w_3^2 + 2\mathrm{D}w_1w_2 + 2\mathrm{E}w_1w_3 + 2\mathrm{F}w_2w_3) = 1. \quad (2.13)$$

Equation (2.13) in a matrix form is represented as:

$$\vec{w}.M.\vec{w} = \frac{1}{MIL(\vec{w})^2} \, , \quad (2.14)$$

where *M* is the MIL tensor [1]; and the MIL tensor consists of the following coefficients:

$$M = \begin{bmatrix} A & D & E \\ D & B & F \\ E & F & C \end{bmatrix}. \quad (2.15)$$

The MIL tensor is used to obtain the fabric tensor, $H = M^{-1/2}$, introduced by Cowin [12]. The eigenvectors of the fabric tensor coincides with the anisotropic directions and its eigenvalues represent the anisotropy ratio in the structure of the materials [12, 13, 51].

2.4.2 The Star Volume Distribution (SVD) and Star Length Distribution (SLD) Methods

The concept of volume orientation has been developed by Odgaard [16]. The total volume of the material is divided to a number of local volumes; the orientation of the

longest arbitrary line which passes a local region of bone without intercepts is the local volume orientation [1, 15, 49]. The length of the longest lines without intercepts within each region is shown by *L*; and the local star volume is computed by:

$$\overline{V_v} = \frac{1}{3}\pi L^3. \tag{2.16}$$

Star Volume Distribution (SVD) method has been defined using the concepts of the local volume orientation and the star volume [1, 11, 49]. If a set of parallel lines in a particular direction ($\vec{w}$) is traced to each local volume, the SVD component in the direction of $\vec{w}$ can be expressed as follow:

$$SVD(\vec{w}) = \frac{\pi}{3}\frac{\sum_{i=1}^{n}(Li(\vec{w}))^4}{\sum_{i=1}^{n}Li(\vec{w})}\ , \tag{2.17}$$

where *n* is the number of intersections between the lines and the interface between two phases at the direction of $\vec{w}$ (as shown with crosses in Figure (2.4)) and *Li* is the length of the bone measured along a line parallel to the direction of $\vec{w}$ for ith intersection (as shown with red line in Figure (2.4)) [49, 77, 78].

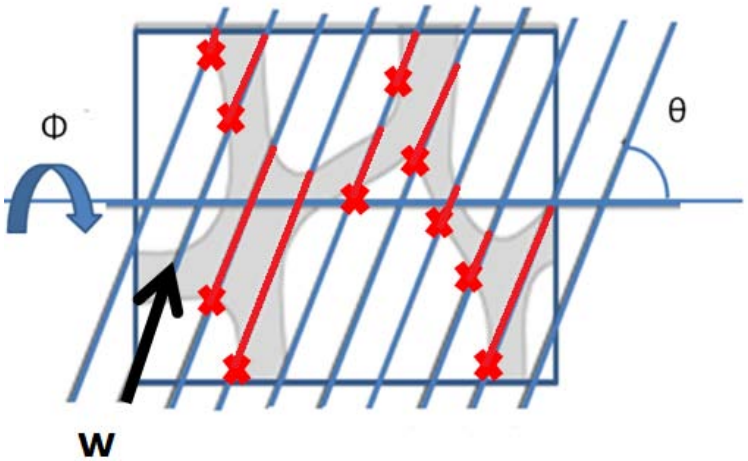

Figure 2.4: The crosses represent the intercepts between a set of parallel lines and the interface between phases. Red lines show the length of the bone for each intersection. Gray and white colors represent bone and morrow, respectively

The best fit ellipsoid to the SVD components is computed by calculation of the magnitudes of the SVD components in all directions. Then, the corresponding SVD tensor is obtained to determine principal anisotropic directions and ratios similarly to the MIL method.

The star length distribution (SLD) method has been introduced by Odgaard by making slight modification on the SVD method. The length is computed in the SLD method instead of the volume in the SVD method [1, 49]. With tracing a set of parallel lines to an arbitrary direction ($\vec{w}$), the SLD components can be expressed by:

$$SLD(\vec{w}) = \frac{\sum_{i=1}^{n}\left(Li(\vec{w})\right)^2}{\sum_{i=1}^{n} Li(\vec{w})} \ , \qquad (2.18)$$

where *n* is the number of intersections between the lines and the interface between two phases at the direction of $\vec{w}$ (as shown with crosses in Figure (2.4)); *Li* is the length of the bone measured along a line parallel to the direction of $\vec{w}$ for i^{th} intersection (as shown with red line in Figure (2.4)). The best ellipsoid fit on the SLD components in all directions, is used to compute the SLD tensor; and the ratio and the directions of anisotropy within each local region of bones are obtained from SLD tensor similarly to the MIL and the SVD methods [49].

2.4.3 Remarks

The binarization of the image data is a necessary and primary step in the described methods. The interfaces between phases (bone and surrounding soft tissue) must clearly be defined from CT images. Binary data must be constructed from CT images to employ the methods for the determination of the structural anisotropic orientations of bones. As

the segmentation and binarization of the images are sensitive to the resolution and noise of the image data, applications of the techniques on low-resolution clinical images cause significant errors [18]; and the application of the methods on the micro-CT (μCT) images of the object is preferred. However, it requires high computational operations and in some cases it is not possible in the clinical environments to apply the complex algorithm of the methods on huge amount of μCT data [14, 17]. In addition, it is not practical to use the methods in cortical bone since the cortical bone has approximately continuous micro-structure.

A new method to determine the anisotropic directions of bones is introduced in the next chapter (Chapter 3) to rectify the mentioned restrictions of the existing techniques. The technique is used to determine the principal anisotropic directions of both cortical and cancellous bones from clinical CT images.

2.5 Bone Elasticity Constants

In order to characterize mechanical properties of an anisotropic material, physical testing must be performed after identifying principal anisotropic directions. The physical testing of bone has been designed to determine the elasticity moduli of bone specimens under different loading conditions. In general, the most of the experiments are commonly designed based on standard procedures used to find the same parameters of industrial materials such as steels, woods and composites; these experimental methods are based on fundamental principles of mechanics. The mechanical tests such as tensile, compression, bending, torsional and indentation are common methods which have been used to obtain

Young's modulus of bones. For instance, to determine the nine independent elastic coefficients of bones as an orthotropic material the following mechanical tests are required: (i) tensile or compressive tests in each of three mutually perpendicular material directions; (ii) three lateral deflection tests to obtain Poisson's ratios; and (iii) three torsional tests to obtain shear moduli [1, 24, 79-83]. Figure 2.5 shows the compression test setup of a dumbbell shape specimen.

Figure 2.5: Set up of compression test on a dumbbell shape specimen [84].

Ultrasonic techniques are also used to determine bone elastic constants. Ultrasonic techniques have significant advantages over mechanical testing methods in the determination of the elastic properties of bone. The procedure of this method is relatively simple and allows using smaller and simple shape specimen [1]. Several mechanical properties can also be measured from a single specimen using this method. The method has advantages in handling in-homogeneity, anisotropy, and size limitations of bones [1,

23, 25, 30]. When density and principal anisotropic directions of a bone specimen are defined the elastic properties of the specimen can be determined from the velocity measurement of shear and longitudinal waves propagating in the concerned directions. The relations between the velocity and the elastic properties follow the theory of small-amplitude elastic wave propagation in anisotropic solids [1]. Although bone material has shown different material properties under tensile and compression loads, this method is not able to differentiate their differences.

Results of the physical tests have shown that bones have large variations in their shape and material properties. Bone material properties are dependent on various parameters such as species, age, sex, disease, and skeletal site [1, 26-28]. Linear correlations between bone density and CT numbers have been established in the previous studies [2, 3]. These correlations motivate the following research to correlate the bone density to elastic constants to estimate local material properties of bones [43, 85].

Commonly, statistically significant numbers of bone specimens have been cut out from whole bones and they have been loaded in material testing machines to determine the elasticity–density relationships. The load–displacement curve has been recorded during the tests; and the stiffness constant has been then calculated from the curve. The original data consisting of calculated mean density of the specimens and the corresponding Young's modulus have been collected and pooled from several mechanical tests. Then, statistical methods have been used to derive elasticity–density relationships for different specimens orientations and tensile/compressive conditions [43]. Based on the established linear correlation between CT numbers and bone density, the elasticity-density functions correlate CT numbers and elasticity constants of bones.

A number of mathematical relationships between measured density and mechanical properties have been proposed in the literature [21, 22, 26, 43]. Selection of the function that correlates bone density and Young's moduli depends on the value of coefficient of determination (R^2). Coefficient of determination indicates how well data points fit a proposed function; and it ranges from 0 to 1. When calculated coefficient of determination is close enough to 1, it means that the proposed elasticity-density relationship can be used to predict local elastic constants of bone from its density. Previous studies have shown that utilizing linear and exponential correlations yield the highest value of the coefficient of determination among the proposed functions [23-28, 85].

$$E = \alpha\rho^{\beta} , \tag{2.19}$$

$$E = \mathrm{A}\rho + \mathrm{B} . \tag{2.20}$$

Different correlations with varied coefficients were derived in different studies. The relationships substantially differ from one to another and the source of such differences in elasticity-density relationships is unclear. Methodological discrepancy is presented as the major reasons of the differences in different studies. However, it is unclear whether such differences in elasticity–density relationships can be entirely explained in terms of methodological discrepancies[43][43][43][43][43][43][43]. Several methodological factors have been discussed as they may have influence on the experimental results obtained by mechanical testing [43]:

1) Specimen preparation (i.e., cutting and milling)
2) Specimen aspect ratio
3) Type of support during testing

4) Specimen geometry

5) Anatomical sampling location

From another perspective, independent elasticity-density correlations for cortical and cancellous bone in different regions of bones can be considered [22, 26]. For instance, independent correlations have been proposed for different regions of skeleton such tibia, femur, humerus and mandible [26, 27]. It has been observed that density-elasticity correlations derived from cancellous bone specimens predicted very low elastic modulus when the correlations extrapolated to density ranges of cortical bone [43]. Therefore, two independent elasticity-density correlations for cancellous and cortical bone have generated more accurate elastic constants in comparison to a single elasticity-density correlation.

Independent correlations (exponential and linear) between Young's modulus and bone apparent density have been also proposed for different anatomical directions to consider anisotropic behaviour of bone [26, 27]. For example, three independent correlations have been defined in anterior-posterior, medial-lateral and superior-inferior directions for cancellous specimens and radial, circumferential and longitudinal for cortical specimens. Mostly, poor correlations have been found between moduli in radial, circumferential and longitudinal directions for cortical bone [26]. The reason of the poor correlations might be the misalignment of the anatomical axes with the principal material axes that can be up to 40°. The misalignment causes underestimation in the order of 30–40% in elasticity moduli [43, 47]. A misalignment of 10° produces an underestimation of 10% in elastic modulus, and for a misalignment of 20° an underestimation in the order of

30–40% can be expected [43, 86]. As orientations of the principal anisotropic directions change in each local region of bone material, this variation should be considered in the definition of density-elasticity correlations. The ignorance of this variation might produce considerable errors in the prediction of elasticity constants [43].

Bone density has been known as the only independent parameter to determine the Young's modulus of bone material in the conventional correlation functions. While the dependency of bone Young's modulus to the direction of applied load or bone anisotropy has not been considered in the most of the existing correlation functions. In this study, density gradient as a new parameter is incorporated to existing elasticity-density correlations to link anisotropic orientations and magnitudes of elastic constants. The details of the procedure to derive new elasticity-density correlations are explained in Chapter 3.

Chapter 3

Materials and Methods

In this chapter a procedure is described to determine: (i) principal anisotropic directions using density gradient, and (ii) the magnitudes of elasticity tensor components along the directions of principal anisotropy based on the magnitude of bone density and its gradient.

3.1 Principal Anisotropic Directions

Schneider *et al.* has used density variation method [55] to find the principal anisotropic directions of both spongy and continuous micro-structures. The main idea is to define anisotropic directions based on the maximum and minimum variations of density in a region of bone tissue. The rationale originates from the star length distribution (SLD) or star volume distribution (SVD) methods. The authors have set a threshold value for density field variables surrounding each voxel in an image of a continuous structure; and the other voxels that exceed the threshold have not been considered. Exclusion of the

density magnitudes of the voxels from density field variables leads to constructing a binary field variable. An orientation, which can move furthest before hitting the constructed void area in the constructed binary field variable, is the direction of the smallest density variation. On the other hand, an orientation that has the shortest distance to the void area is the direction of the largest density variation. The direction of the smallest density variation coincides with one of the principal anisotropic directions, while using SLD and SVD methods, the direction of the largest density variation is also coincident with second principal anisotropic directions [55]. The third principal anisotropic direction is perpendicular to both the first and second principal anisotropic directions. In this work, a new approach will be introduced to determine the largest and the smallest density variation in each voxel of 3D CT images by constructing anisotropic voxels. To determine the principal anisotropic directions, this new approach comprehends the following tasks:

(i) Defines bone density gradient by constructing anisotropic voxels,

(ii) Establishes a relationship between the smallest or the largest variations of bone density and the bone density gradient.

3.1.1 Construction of Anisotropic Voxels to Calculate Bone Density Gradient

A voxel is the basic unit of CT images; and the corresponding segment of a bone specimen to the voxel is termed as a bone voxel. Each voxel has its voxel intensity. The voxel intensity is proportional to radio density of bone voxels and is scaled using a

standard procedure. The scaled numbers are known as CT numbers. There is a linear correlation between the CT number and bone apparent density in each voxel,

$$\rho\left(\frac{g}{cm^3}\right) = a \times CT(HU) + b\ . \quad (3.1)$$

In the conventional method, it is assumed that bone density is constant in a voxel, although there may be a variation, especially if the resolution is low and the voxel size is large. Young's modulus is only defined as a function of bone apparent density in the existing mathematical correlations [26, 43], therefore, constant Young's modulus is assigned to each bone voxel. The dependency of Young's modulus on the orientation of the applied load (anisotropy) has not been considered. In this study, voxels with variable material properties (anisotropic behavior) are considered by modifying the existing elasticity-density empirical functions.

The results of image processing of bones have demonstrated that the pairs of bone voxels neighboring to each other are usually different in their CT numbers [55, 87]. Therefore, a gradual change in bone density from a voxel to its neighbours is a reasonable assumption to make. This assumption requires a variation in bone density of a bone voxel. In this study, we employ an interpolation technique to construct a linear density functions. Density variations are calculated based on the density of voxels, which surround the concerned voxel, using the finite difference method. Since the voxels with density variations exhibited anisotropic behavior, the voxels are termed as anisotropic voxels in this study.

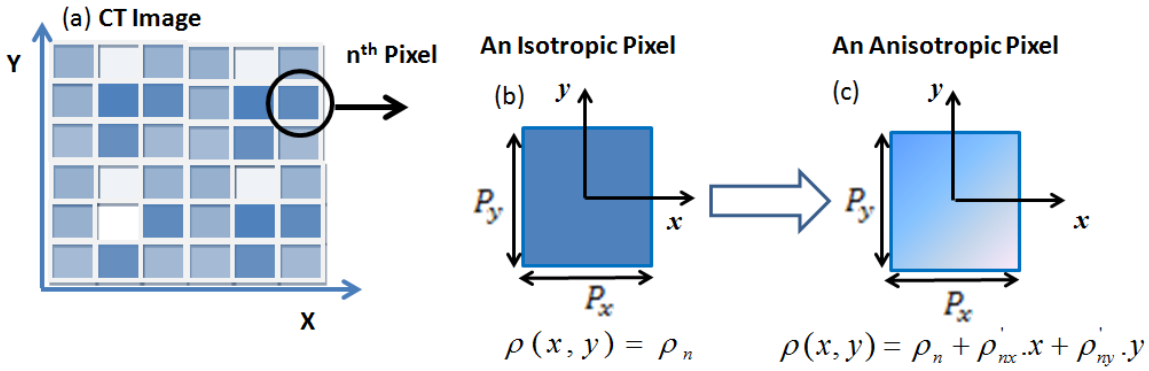

Figure 3.1: (a) A part of a CT image in the global coordinate system (X,Y) (b) the isotropic pixel with constant density in the voxel coordinate system (x,y) and (c) the anisotropic pixel with the variable density in the voxel coordinate system (x,y).

A Cartesian coordinate system is used here to construct the anisotropic voxel, one global (X,Y,Z) and two different local coordinate systems are associated with each voxel. The local coordinate systems are the voxel coordinate system (*x,y,z*) and the material coordinate system *(l,r,t)*. A plane view of the global coordinate system, the local coordinate systems (*x,y*), the isotropic and anisotropic pixels are shown in Figure 3.1. The corresponding 3D view of the voxel coordinate system (*x,y,z*) and the material coordinate system *(l,r,t)* are shown in Figure 3.2.

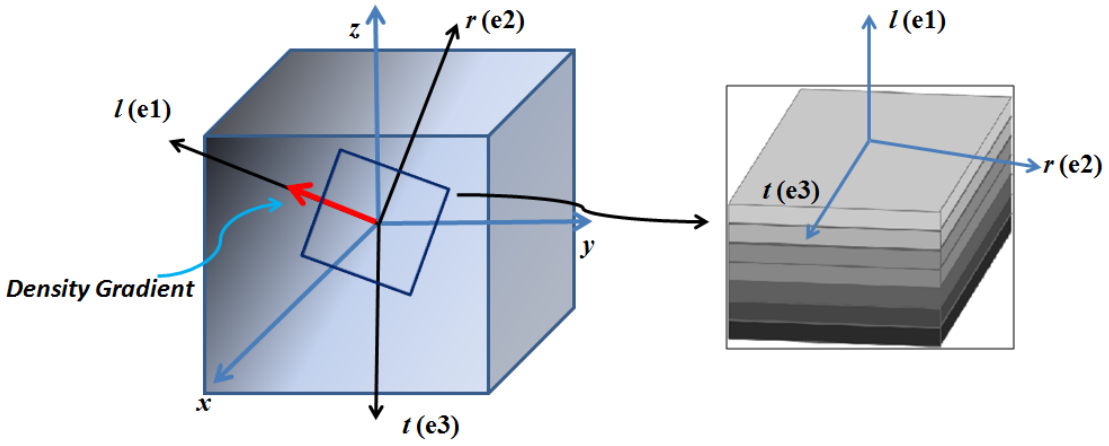

Figure 3.2: The voxel coordinate system (x,y,z), the material coordinate system *(l,r,t)* and the three principal anisotropic directions (e1,e2,e3).

The origin and the axes of the global coordinate system coincide with the origin of the constructed 3D CT images and parallel to the edges of CT voxels, respectively. Due to the small size of the voxels, a linear correlation between bone density and coordinates of each node in an anisotropic voxel is proposed in Equation (3.2):

$$\rho(X,Y,Z) = \rho_n + \rho'_{nX}.\Delta X + \rho'_{nY}.\Delta Y + \rho'_{nZ}.\Delta Z = \rho_n + \rho'_{nX}.(X - X_n) + \rho'_{nY}.(Y - Yn + \rho nZ'.Z - Zn, \quad (3.2)$$

where the subscript *n* is defined based on the location of the voxel in the global coordinate system. X_n, Y_n and Z_n are signed distances of the center of nth voxel to X, Y and Z axes; and *X*, *Y* and *Z* are signed distances of the evaluation point to the X, Y and Z axes. ρ'_{nX}, ρ'_{nY} and ρ'_{nZ} are density derivatives of nth voxel with respect to *x*, *y* and *z*.

In the voxel coordinate system: (i) the origin of the voxel coordinate system is located at the center of each voxel; and (ii) all axes are parallel to the voxel edges. If Equation (3.2) is rewritten with respect to the voxel coordinate system, it is transformed to Equation (3.3):

$$\rho(x,y,z) = \rho_n + \rho'_{nx}.x + \rho'_{ny}.y + \rho'_{nz}.z\,, \quad (3.3)$$

where *x*, *y* and *z* are signed distances of the evaluation points to x, y and z axes, respectively. *x*, *y* and *z* values vary based on the voxel dimensions ($\frac{-P_x}{2} \le x \le \frac{P_x}{2}$, $\frac{-P_y}{2} \le y \le \frac{P_y}{2}$, $\frac{-P_z}{2} \le z \le \frac{P_z}{2}$), where P_x, P_y and P_z are the voxel dimensions.

The linear correlation between CT numbers and bone density is used to calculate density derivatives with respect to *x*, *y* and *z*.

$$\rho'_{nx} = aCT'_{nx}\,, \quad (3.4.1)$$

$$\rho'_{ny} = aCT'_{ny} \text{ and} \quad (3.4.2)$$

$$\rho'_{nz} = aCT'_{nz}\,, \tag{3.4.3}$$

where CT'_{nx} , CT'_{ny} and CT'_{nz} are the directional derivatives of the CT function with respect to *x*, *y* and *z*. By substituting Equations (3.4.1), (3.4.2) and (3.4.3) in to Equation (3.3), Equation (3.5) is obtained to define the density in an anisotropic voxel using the CT numbers and their directional derivatives.

$$\rho(x,y,z) = a\left(CT_n + CT'_{nx}.x + CT'_{ny}.y + CT'_{nz}.z\right) + b, \tag{3.5}$$

where $CT_n + CT'_{nx}.x + CT'_{ny}.y + CT'_{nz}.z$ is defined as the CT function, which gives the CT number in an anisotropic voxel with respect to the voxel coordinate system

$$CT(x,y,z) = CT_n + CT'_{nx}.x + CT'_{ny}.y + CT'_{nz}.z, \tag{3.6}$$

While each point with CT number below the lowest limit of CT number range, are treated as isotropic. In this study, the CT numbers of soft tissue are considered to be a constant with the value of the lowest limit [55]. In order to calculate the CT function derivatives: (i) CT numbers from CT images are assigned to the center of each voxel, (ii) second-order finite difference (FD) method was employed using CT numbers of the neighbours of evaluation voxel.

Finite difference is a robust method, which is used to approximate differential operators. The finite difference recipes have been reported to approximate any order of derivatives and any order of accuracy on one-dimensional grid with arbitrary spacing in the literature [88]. Special cases such as centered and one-sided approximation commonly occur. Centered approximation occurs, when there is enough discrete data in both sides of an evaluation point; otherwise, one-sided approximation is applied to approximate the derivative. Equations (3.7.1) and (3.7.2) show the relation between CT

numbers and the derivatives of the CT numbers in the x direction of the anisotropic voxel. If a given voxel is located close to the edges of a bone sample, where adjacent voxels are not available to construct Equation (3.7.1), the one-sided approximation is employed (Equation (3.7.2)):

$$CT'_{nx} = \frac{CT_{(n+1)x} - CT_{(n-1)x}}{2P_x}, \quad (3.7.1)$$

$$CT'_{nx} = \frac{CT_{(n+1)x} - CT_{nx}}{P_x}, \quad (3.7.2)$$

The same procedure is applied to calculate CT'_{ny} and CT'_{nz} in the anisotropic voxels:

$$CT'_{ny} = \frac{CT_{(n+1)y} - CT_{(n-1)y}}{2P_y}, \quad (3.7.3)$$

$$CT'_{ny} = \frac{CT_{(n+1)y} - CT_{ny}}{P_y}, \quad (3.7.4)$$

$$CT'_{nz} = \frac{CT_{(n+1)z} - CT_{(n-1)z}}{2P_z} \text{ and} \quad (3.7.5)$$

$$CT'_{nz} = \frac{CT_{(n+1)z} - CT_{nz}}{P_z}, \quad (3.7.6)$$

where all the subscripts are defined based on the location of the voxel in the global coordinate system, as shown in Figure 3.3.

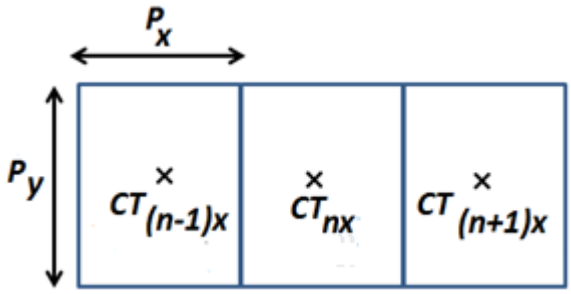

Figure 3.3: Arrangement of three pixels, which are used to find a derivative of the centered pixel from Equation (3.7.1).

3.1.2 Determination of Principal Anisotropic Directions

In order to determine the principal anisotropic directions, the largest and the smallest variation of the density in the region of interest must be determined using the density

variation method [55]. In this study, the density variation is approximated with the interpolation function (Equation 3.3) in an anisotropic voxel. The maximum and the minimum directional derivatives of density in a voxel of CT images are then used to find the principal anisotropic directions.

The maximum directional derivative of the density, which is the first principal anisotropic direction, is obtained by calculating the gradient of the interpolation function (Equation 3.3),

$$\nabla\rho(x,y,z) = \rho'_x\hat{\imath} + \rho'_y\hat{\jmath} + \rho'_z\hat{\mathrm{k}}\,, \tag{3.8}$$

where ρ'_x , ρ'_y and ρ'_z are derived from CT function definition using Equations (3.4.1), (3.4.2) and (3.4.3).

Based on the rule for scalar product of two vectors, the directional derivative is zero in the plane normal to the gradient vector. Therefore, the minimum directional derivative of the density in a voxel of CT images occurs in the plane normal to the density gradient vector. As no density variation exists in the plane normal to the density gradient vector in each voxel, the plane is assumed to be the plane of isotropy (Figure 3.4). It resembles that the material of each bone voxel possesses one axis of symmetry parallel to density gradient in the sense that all material properties at right angles to this axis are equivalent. The material can also be rotated with respect to the loading direction about the axis of symmetry without measurable effect on the material response (Figure 3.4) [55, 56]. Consequently, a transversely isotropic model of material behavior is assigned to each bone voxel. Transversely isotropic is a special case of an orthotropic material that the material contains a plane of isotropy and an axis of symmetry as shown in Figure 3.4.

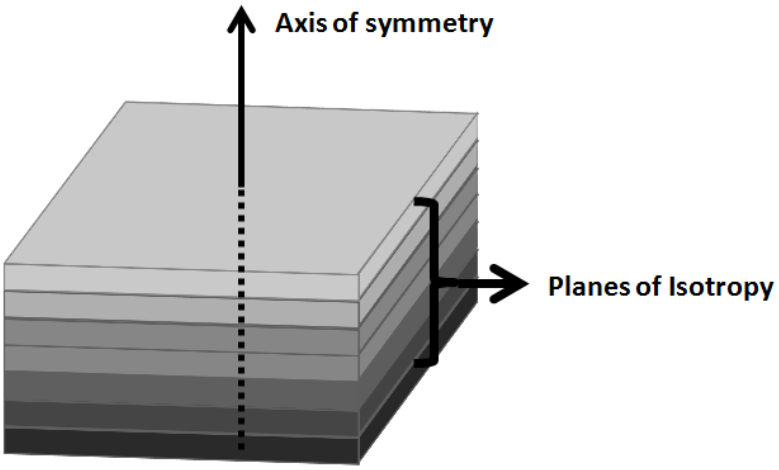

Figure 3.4: Transversely isotropic material model.

In a transversely isotropic material, principal anisotropic directions are determined by finding the axis of symmetry (e1) (the bone density gradient). Since the plane perpendicular to the axis of symmetry is isotropic, the orientation of the other two orthonormal anisotropic directions (e2 and e3) are arbitrary on the plane of isotropy [56]. Since each voxel has a plane of isotropy and an axis of symmetry with independent directions, pointwise transversely isotropic material model is defined for long bones.

3.2 Anisotropic Elasticity or Compliance Matrix

In this section, a method is introduced to determine the magnitude of elasticity tensor components in the principal anisotropic directions. The linear elastic material behavior for bones was defined as:

$$\sigma = D\varepsilon, \tag{3.9}$$

where σ is the total stress, D is elasticity matrix; and ε is the total strain. Bones are pointwise transversely isotropic. To express the elasticity or compliance matrix in terms

of engineering constants such as Poisson's ratio (v), Young's moduli (E) and shear moduli (G), the matrix must be defined in directions of axis of symmetry and plane of isotropy. As each voxel is transversely isotropic, the following conditions are provided between the components of compliance matrix: $E_1 = E_a$, $E_2 = E_3 = E_p$, $v_{12} = v_{13} = v_{ap}$, $v_{21} = v_{31} = v_{pa}$, $v_{23} = v_p$, $G_{12} = G_{13} = G_a$ and $G_{23} = G_p$, where a and p respectively stand for the axis of symmetry direction and plane of isotropy. v_{ap} and v_{pa} were not equal and they were related by:

$$\frac{v_{ap}}{E_a} = \frac{v_{pa}}{E_p}. \tag{3.10}$$

Hence, the compliance matrix for each transversely isotropic voxel of bone material reduced to:

$$D^{-1}{}_{123} = \mathrm{C}_{123} = \begin{bmatrix} \frac{1}{E_\mathrm{a}} & \frac{-v_{ap}}{E_\mathrm{a}} & \frac{-v_{ap}}{E_\mathrm{a}} & & & \\ \frac{-v_{ap}}{E_\mathrm{a}} & \frac{1}{E_\mathrm{p}} & \frac{-v_\mathrm{p}}{E_\mathrm{p}} & 0_{3\times3} & & \\ \frac{-v_{ap}}{E_\mathrm{a}} & \frac{-v_\mathrm{p}}{E_\mathrm{p}} & \frac{1}{E_\mathrm{p}} & & & \\ & & & \frac{1}{\mathrm{G_a}} & 0 & 0 \\ 0_{3\times3} & & & 0 & \frac{1}{\mathrm{G_a}} & 0 \\ & & & 0 & 0 & \frac{1}{\mathrm{G_p}} \end{bmatrix}, \tag{3.11}$$

where the Poisson's ratio is considered as a density independent parameter [81, 87, 89]. Equation (3.12.1) is proposed to determine the shear moduli from the Young's modulus and Poisson's ratio,

$$G_{iso} = \frac{E_{iso}}{2(1+v_{iso})}, \tag{3.12.1}$$

The equation is applied in the orientations of the plane of isotropy and the axis of symmetry. The following equations are adopted for the principal anisotropic directions as suggested by Schneider *et al*. [55]:

$$G_a = \frac{E_a}{2(1+v_{ap})} \text{ and} \tag{3.12.2}$$

$$G_P = \frac{E_P}{2(1+v_p)} \ . \tag{3.12.3}$$

Having known Poisson's ratios and shear moduli, Young's moduli in the principal anisotropic directions in each voxel are the other parameters required to determine compliance matrix components. To determine independent correlations between Young's moduli and the bone density in the principal anisotropic directions, a specimen were cut from a voxel and virtual compression tests were performed (Figure 3.5).

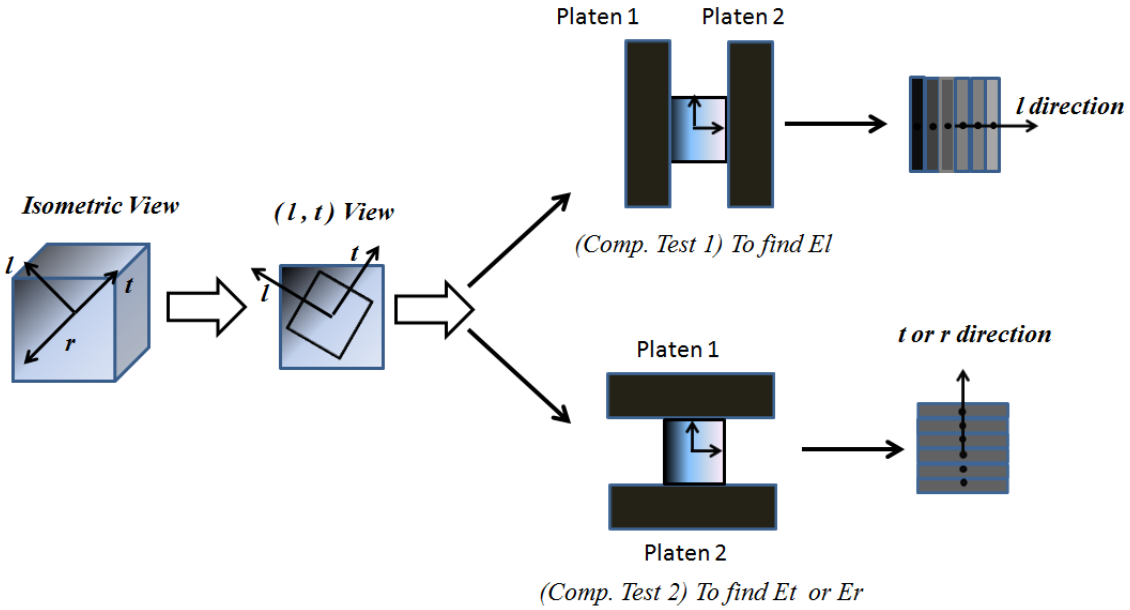

Figure 3.5: Anisotropic voxels and virtual tests.

In each loading direction, the structure of the specimen is approximated by a laminate that consists of a number of sheets. Each sheet is assumed to be homogeneous, and they

were only loaded in their plane during the virtual compression test. Therefore, the structure of the specimen is dependent on loading directions, which is explained as follows:

(i) Virtual Comp. Test No.1, load in the direction of density gradient or axis of symmetry (e1):

The structure of the specimen is simulated in the way that the layers are only loaded in their plane. The sheets are extended in the direction normal to the applied load, and each sheet is made of an independent material with homogeneous structure as shown in Figure 3.5. When the number of the sheets increased to infinity, the variation of bone density of the specimen is expressed by Equation (3.13) in the first principal anisotropic direction (e1), i.e., the direction of the density gradient (axis of symmetry):

$$\rho(l) = \rho_n + |\nabla\rho_n|.\, l. \tag{3.13}$$

(ii) Virtual Comp. Test No.2, load in the plane of isotropy (e2 and e3):

The structure of the specimen is also simulated with a number of thin sheets in the way that the layers are only loaded in their plane. The mean density of each layer is assigned to the corresponding layer. Results of the calculations showed that the mean density of each layer is constant, and it remains constant in the directions of the plane of isotropy (e2 and e3). Hence, constant density is assigned to the simulated structure in the direction of the plane of isotropy (e2 and e3) as:

$$\rho(t) = \rho(r) = \rho_n \ . \tag{3.14}$$

The exponential and linear correlations between Young's modulus and bone apparent density are proposed with the highest determination of coefficient for cancellous and cortical bone in isotropic voxel in the literature [21, 22, 26]. The same correlation, which

has been used in an isotropic voxel, is used to determine the Young's modulus in the plane of isotropy directions in this study since the density does not vary in the corresponding plane.

$$E_{p-can} = \alpha {\rho_n}^{\beta} \quad , \tag{3.15.1}$$

$$E_{p-cor} = A\rho_n + B \ , \tag{3.15.2}$$

where *can* and *cor* represent cancellous and cortical bone, respectively. As the density variation occurred along the direction of the axis of symmetry, the variation of density (bone density gradient) is also incorporated in the Young's modulus and bone density correlation function. The variation of the bone density is determined in the voxel coordinate system (Equation 3.16.1) and the material coordinate system (Equation 3.16.2) by:

$$\rho_n(x,y,z) = \rho_n + \rho_{nx}^{'}.x + \rho_{ny}^{'}.y + \rho_{nz}^{'}.z \text{ and} \tag{3.16.1}$$

$$\rho_n(l,r,t) = \rho_n + |\nabla\rho_n(x,y,z)|.l \ , \tag{3.16.2}$$

where l is a signed distance of the evaluation point from the l axis; and x,y and z are the signed distances of the evaluation point from the x, y and z axes (Figure 3.2).

Substituting Equation (3.16.2) into Equations (3.15.1) and (3.15.2), the correlations (Equations (3.17.1) and (3.17.2)) between Young's moduli, bone density and its gradient along the axis of symmetry of each anisotropic voxel are derived as,

$$E_{a-can} = \alpha(\rho_n + |\nabla\rho_n|.l)^{\beta} \text{ and} \tag{3.17.1}$$

$$E_{a-cor} = A(\rho_n + |\nabla\rho_n|.l) + \mathrm{B} \ . \tag{3.17.2}$$

Hence, Young's moduli in the three principal anisotropic directions are expressed by:

$$\mathrm{E}_{1-\mathrm{can}} = E_{a-can} \ , \tag{3.18.1}$$

$\mathrm{E}_{2-\mathrm{can}} = \mathrm{E}_{3-\mathrm{can}} = \mathrm{E}_{\mathrm{p}-\mathrm{can}}$, (3.18.2)

$\mathrm{E}_{1-\mathrm{cor}} = E_{a-cor}$ and (3.18.3)

$\mathrm{E}_{2-\mathrm{cor}} = \mathrm{E}_{3-\mathrm{cor}} = \mathrm{E}_{\mathrm{p}-\mathrm{cor}}$. (3.18.4)

Having known Young's moduli in principal anisotropic directions, the compliance matrix is constructed for each voxel from the CT image information. The inverse of the compliance matrix is the elasticity matrix, D, which gives the stresses produced by an elastic strain state. Transversely isotropic elasticity matrix of each voxel was obtained in the material coordinate system *(l,r,t)* as follows:

$$D_{123} = \begin{bmatrix} \frac{Ea(-vp^2+1)}{K} & \frac{Ep.(vap.vp+vap)}{K} & \frac{Ep.(vap.vp+vap)}{K} & 0 & 0 & 0 \\ & \frac{Ep.(-\frac{vap^2.Ep}{Ea}+1)}{K} & \frac{Ep.(\frac{vap^2.Ep}{Ea}+vp)}{K} & 0 & 0 & 0 \\ & & \frac{Ep.(-\frac{vap^2.Ep}{Ea}+1)}{K} & 0 & 0 & 0 \\ & & & Ga & 0 & 0 \\ & Sym. & & & Ga & 0 \\ & & & & & Gp \end{bmatrix}, \quad (3.19)$$

where $k = 1 - \frac{2E_2}{E_1}\left(v_{ap}{}^2 v_p - v_{ap}{}^2\right) - v_p{}^2$. The elasticity matrix is also symmetric and positive, yielding to the following restrictions: $k > 0$, $1 - v_p{}^2 > 0$ and $1 - v_{ap}{}^2 \frac{E_2}{E_1} > 0$. The elasticity matrix of bones is also pointwise transversely isotropic in the material coordinates systems with five independent constants.

In order to calculate elasticity matrix in the global coordinate system, by using elasticity matrix in material coordinate system, the transformation matrix, G, can be formed as [56]:

$$G = \begin{bmatrix} l_x^2 & l_y^2 & l_z^2 & l_x l_y & l_x l_z & l_y l_z \\ r_x^2 & r_y^2 & r_z^2 & r_x r_y & r_x r_y & r_x r_y \\ t_x^2 & t_y^2 & t_z^2 & t_x t_y & t_x t_y & t_x t_y \\ 2l_x r_x & 2l_y r_y & 2l_z r_z & l_x r_y + l_y r_x & l_z r_x + l_x r_z & l_y r_z + l_z r_y \\ 2l_x t_x & 2l_y t_y & 2l_z t_z & t_x l_y + t_y l_x & t_z l_x + t_x l_z & t_y l_z + t_z l_y \\ 2r_x t_x & 2r_y t_y & 2r_z t_z & r_x t_y + r_y t_x & r_z t_x + r_x t_z & r_y t_z + r_z t_y \end{bmatrix}, \quad (3.20)$$

where (l_x, l_y, l_z) is a unit vector in the *l*-direction (the first principal anisotropic direction or density gradient direction), described in the XYZ-coordinate system. $(\mathrm{r_x}, \mathrm{r_y}, \mathrm{r_z})$ is a unit vector in the r-direction (second principal anisotropic direction); and the $(\mathrm{t_x}, \mathrm{t_y}, \mathrm{t_z})$ is a unit vector in the t-direction (third principal anisotropic direction). As the first principal anisotropic direction is parallel to the voxel density gradient and two other principal anisotropic directions are arbitrary in the plane of isotropy, the following equations are proposed to correlate unit vectors in *(l,r,t)* axes with density gradient components:

$$(l_x, l_y, l_z) = \frac{1}{|\nabla\rho|}(\rho_x, \rho_y, \rho_z) \ , \quad (3.21.1)$$

$$(r_x, r_y, r_z) = \frac{1}{\sqrt{{\rho_x}^2 + {\rho_z}^2}}(\rho_z, 0, -\rho_x) \ \text{ and} \quad (3.21.2)$$

$$(t_x, t_y, t_z) = (l_x, l_y, l_z) \times (r_x, r_y, r_z) = \frac{1}{|\nabla\rho|\sqrt{{\rho_x}^2 + {\rho_z}^2}}\left(-\rho_x\rho_y, {\rho_x}^2 + {\rho_z}^2, -\rho_z\rho_y\right). \quad (3.21.3)$$

The transformation of stiffness properties, from the material to the global coordinate system, is performed by a tensor-like transformation,

$$D_{XYZ} = G^T D_{123} G \quad \text{and} \quad (3.22.1)$$

where the components of the matrix are functions of the following parameters,

$$D_{ijkl\_XYZ} = f_n(\rho, \rho_x, \rho_y, \rho_z, x, y, z, v_p, v_{ap}). \quad (3.22)$$

The elasticity matrix of bones has twenty one constants in the global coordinate system, where each constant is a complex function of density, density gradients and Poisson's ratios.

Chapter 4

Numerical Investigations

This chapter describes the following numerical procedures:

(i) To perform finite element (FE) analysis using the mechanical model defined in Chapter 3,

(ii) To compare the conventional isotropic FE models versus the anisotropic FE models of large specimens (with the size of actual compression tests) under virtual compression loads,

(iii) To evaluate the accuracy of the anisotropic model compared with the conventional isotropic model using FE analyses.

4.1 Construction of the Finite Element Model

The basic governing equations for an elastic problem consist of the following relations [90]:

(i) Strain-displacement relations,

$$\varepsilon_x = \frac{\partial u}{\partial x}, \tag{4.1.1}$$

$$\varepsilon_y = \frac{\partial v}{\partial y}, \tag{4.1.2}$$

$$\varepsilon_z = \frac{\partial w}{\partial z}, \tag{4.1.3}$$

$$\gamma_{xy} = \frac{\partial u}{\partial y} + \frac{\partial v}{\partial x}, \tag{4.1.4}$$

$$\gamma_{xz} = \frac{\partial u}{\partial z} + \frac{\partial w}{\partial x}, \tag{4.1.5}$$

$$\gamma_{yz} = \frac{\partial v}{\partial z} + \frac{\partial w}{\partial y}, \tag{4.1.6}$$

where u, v and w represent the deformations in x, y and z directions.

(ii) Stress-strain relations,

$$\sigma_{ij} = D_{ijmn}\varepsilon_{mn}, \tag{4.2}$$

where σ is the total stress, D is elasticity matrix; and ε is the total strain.

(iii) Equilibrium equations,

$$\frac{\partial \sigma_x}{\partial x} + \frac{\partial \tau_{xy}}{\partial y} + \frac{\partial \tau_{xz}}{\partial z} + B_x = 0\,, \tag{4.3.1}$$

$$\frac{\partial \tau_{xy}}{\partial x} + \frac{\partial \sigma_y}{\partial y} + \frac{\partial \tau_{yz}}{\partial z} + B_y = 0\,, \tag{4.3.2}$$

$$\frac{\partial \tau_{xz}}{\partial x} + \frac{\partial \tau_{yz}}{\partial y} + \frac{\partial \sigma_z}{\partial z} + B_z = 0\,, \tag{4.3.3}$$

where B_x , B_y and B_z are body forces in x , y and z directions, respectively.

(iv) Boundary conditions.

Two types of boundary conditions are basically defined: (i) essential boundary conditions where displacements are known and (ii) secondary boundary conditions where forces are given [90].

However, the exact solutions to the governing equations of bones problems are generally not available due to their complicated mechanical properties, geometry and boundary conditions. Hence, the finite element method is introduced as a valuable numerical approximation tool for the solution of the governing equations when the analytical solutions are difficult or impossible.

There are different types of commercial FE software used for FE modeling. In this work, Abaqus 6.11.1 has been used for the numerical investigation. An algorithm needs to be defined to implement the isotropic and pointwise transversely isotropic material model in Abaqus. This section explains a procedure to create both isotropic and pointwise transversely isotropic FE models in Abaqus 6.11.1 software using CT images.

The construction of the FE models is divided into two main steps. First, an in-house MATLAB code was written to generate a data set, which includes material properties of the bone specimen. Then, the constructed data set are imported to the Abaqus software to generate the FE models. Each step includes several sub-steps and they are illustrated in following chart,

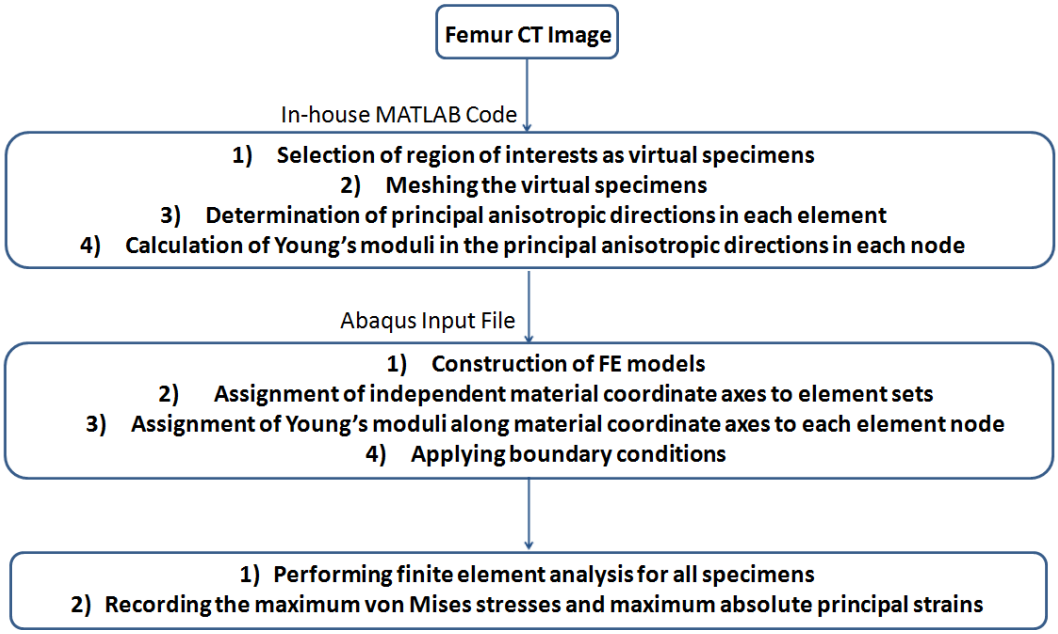

Figure 4.1: The overall procedure to construct FE models using a given CT data set for a bone specimen.

4.1.1 MATLAB Codes

The in-house MATLAB codes implement the following steps:

1) The CT image data in DICOM format are imported as a matrix into MATLAB using the function named "dicomread". Figure 4.2 schematically shows a part of a bone image consisting of 6×6 pixels and the corresponding matrix created in MATLAB software.

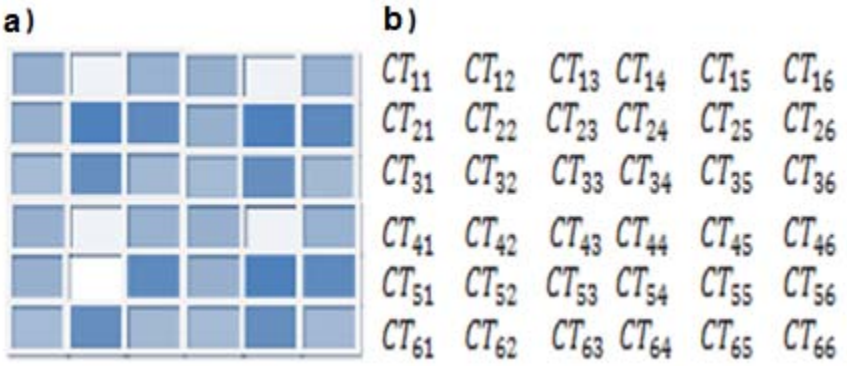

Figure 4.2: a) A part of a bone image consisting of 6×6 pixels, b) the matrix of the CT numbers in MATLAB.

2) The matrix data are converted to CT numbers in Hounsfield Units. The lowest limit of CT numbers for bone material is -115HU. The parts with CT numbers under and equal to -115HU are considered to be a constant value equals to -115HU (the lowest limit) [55].
3) The region of interest is selected in the image of the bone specimen; and the corresponding matrix associated with the region is extracted from the primary matrix.
4) The global coordinate system is defined for the bone specimen with the axes parallel to the voxel edges, where the origin is located on one corner of the specimen as shown in Figure 4.3.
5) The coordinates of the center of each voxel are calculated with respect to the global coordinate system and the corresponding CT numbers are assigned to the center of each voxel as shown in Figure 4.3.

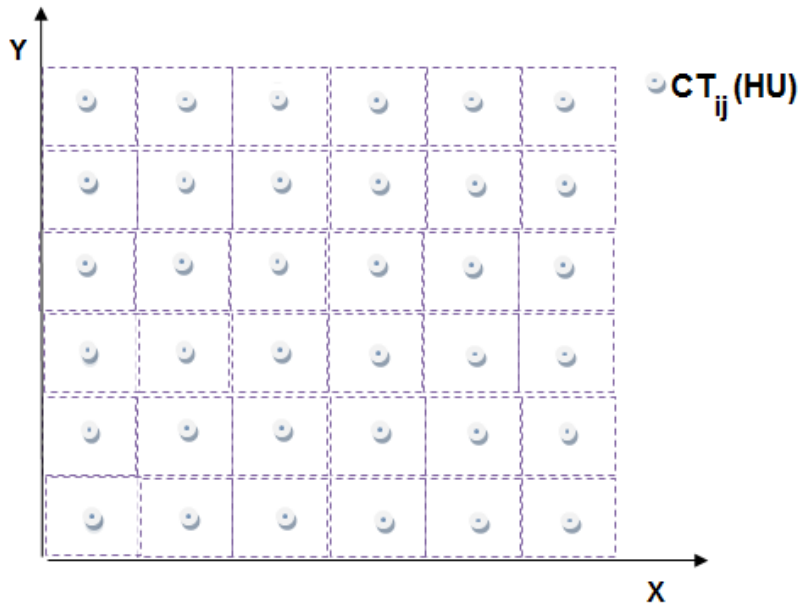

Figure 4.3: CT numbers assign to the center of each pixel.

6) The first-order derivatives of the CT numbers are calculated using the finite difference (FD) method.

   This part of the MATLAB codes was validated by applying the codes to the following 3D analytical function.

$$f(x,y,z) = \frac{\sin\left(4\sqrt{x^2+y^2+z^2}+4\right)}{8\sqrt{x^2+y^2+z^2}+8}, \tag{4.4}$$

   The function has three variables, x ,y and z, defined over the domain {-3≤x≤3, 3≤y≤3, -3≤z≤3}. The directional derivatives of the function with respect to x,y and z are calculated analytically as follows:

$$\frac{\partial f(x,y,z)}{\partial x} = \frac{4x.\cos\left(4\sqrt{x^2+y^2+z^2}+4\right)}{\sqrt{(x^2+y^2+z^2)}\left(8\sqrt{x^2+y^2+z^2}+8\right)}, \tag{4.5}$$

$$\frac{\partial f(x,y,z)}{\partial y} = \frac{4y.\cos\left(4\sqrt{x^2+y^2+z^2}+4\right)}{\sqrt{(x^2+y^2+z^2)}\left(8\sqrt{x^2+y^2+z^2}+8\right)}, \tag{4.6}$$

$$\frac{\partial f(x,y,z)}{\partial z} = \frac{4z.\cos\left(4\sqrt{x^2+y^2+z^2}+4\right)}{\sqrt{(x^2+y^2+z^2)}\left(8\sqrt{x^2+y^2+z^2}+8\right)} \text{ and} \tag{4.7}$$

$$\nabla f(x,y,z) = \sqrt{\left(\frac{\partial f(x,y,z)}{\partial x}\right)^2 + \left(\frac{\partial f(x,y,z)}{\partial x}\right)^2 + \left(\frac{\partial f(x,y,z)}{\partial y}\right)^2}. \tag{4.8}$$

   The gradient obtained using Equation (4.8) is compared with the gradient calculated based on the FD method. The results and relevant errors obtained for the function are presented and discussed in Chapter 5.

7) Eight-nodes brick element of the same size is used to construct the FE models in this study.

8) The coordinates of elements nodes with respect to the voxel coordinate system and material coordinate system are also calculated.

9) The bone density and isotropic Young's modulus are calculated for each FE element node in the following way.

   Isotropic Young's modulus of cancellous (can) and cortical (cor) parts of the bone specimens are calculated using the well-established elasticity-density correlations reported by Lotz *et al.* [21, 22]. These correlations were obtained by compression and three-point-bending tests of human femur heads with a high coefficient of determination (R^2=0.93).

   $\rho < 1.04 \left(\frac{g}{cm^3}\right)$ $\quad E_{can.}(MPa) = 1310\rho^{1.4}$ and (4.9)

   $\rho > 1.04 \left(\frac{g}{cm^3}\right)$ $\quad E_{cor.}(MPa) = 14261\rho - 13430$. (4.10)

   Bone apparent density (ρ) was calculated from the CT numbers using Equation (4.11) [21, 22]:

   $$\rho \left(\frac{g}{cm^3}\right) = 0.0012 \times CT(HU) + 0.17 \text{ .} \quad (4.11)$$

10) Principal anisotropic directions were calculated and assigned to each element as follows:

    The direction of density gradient must be calculated to determine the principal anisotropic directions in each element. As a constant density gradient is defined for each voxel, the same principal anisotropic directions are assigned to all elements located in the corresponding voxel. In order to assign the principal anisotropic directions to a set of elements located in n^{th} voxel in Abaqus software, a material coordinate system (l_n, r_n, t_n) with the axes parallel to the principal anisotropic

directions of n^{th} voxel must be defined. Since bone specimens are usually made of thousands of the voxels, construction of an independent material coordinate system for each voxel is not practical using Abaqus. Hence, the following procedure is used to assign the pointwise anisotropy with limited sets of independent material coordinate system with a good approximation.

a) Numbers of datum coordinate systems with constant interval angles in spherical coordinate system are constructed. The first axes of the datum coordinate systems are shown with two angles as follow:

$$first\ axes\ of\ datum\ coordinate\ systems = \{(1, \theta_1', \alpha_1'), (1, \theta_2', \alpha_2'), (1, \theta_3', \alpha_3'), \dots, (1, \theta_i', \alpha_i')\}$$

where θ_i' range is $0 \leq \theta_i' < 180$ and α_i' range is $0 \leq \alpha_i' < 90$.

b) The first principal anisotropic direction is defined for each voxel using the density gradient vector. The unit vector in the first principal anisotropic direction, e_{n1}, is transformed to spherical coordinate system $(\mathrm{r}, \theta, \alpha)$ for each voxel by:

$$e_{n1} = \frac{(\rho'_{nx}\mathrm{i}, \rho'_{ny}\mathrm{j}, \rho'_{nz}\mathrm{k})}{\sqrt{{\rho'_{nx}}^2 + {\rho'_{ny}}^2 + {\rho'_{nz}}^2}} = (\mathrm{r_n}, \theta_\mathrm{n}, \alpha_\mathrm{n}) =$$

$$\left(1, \mathrm{Arctg}\left(\frac{\rho'_{ny}}{\rho'_{nx}}\right), \mathrm{Arctg}\left(\frac{\rho'_{nz}}{\sqrt{{\rho'_{nx}}^2 + {\rho'_{ny}}^2}}\right)\right), \tag{4.12}$$

where θ_n range is $0 \leq \theta_n < 180$ and α_n range is $0 \leq \alpha_n < 90$ for the given gradient vector as shown in Figure 4.4.

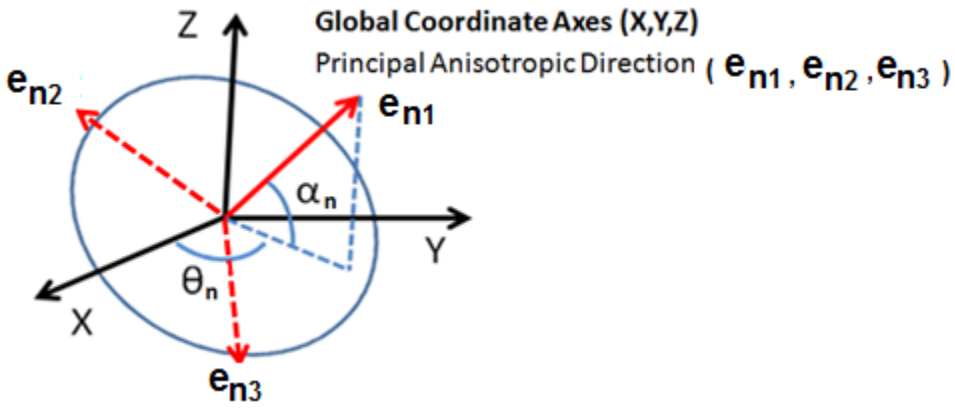

Figure 4.4: Spherical angles of the first principal anisotropic direction.

c) The first principal anisotropic direction of n^{th} voxel $(1, \theta_n, \alpha_n)$ is compared to the direction of first axes of datum coordinate systems $(1, \theta_i', \alpha_i')$. The first axis of datum coordinate systems closest to the first principal anisotropic direction (density gradient vector) of the n^{th} voxel is identified; and the corresponding datum coordinate system is assigned to the elements located in the n^{th} voxel $(1, \theta_n', \alpha_n')$. Hence, the orientation of the first axes of material coordinate system $(1, \theta_n', \alpha_n')$ for each element is selected. All elements with parallel first axis of material coordinate system are collected in an element set. Adopting this procedure, the number of the independent material coordinate systems becomes independent of the number of a bone specimen voxels.

d) In this study, according to the calculated θ_n and α_n from Equation (4.12), the corresponding θ_n' and α_n' are obtained using Table 4.1.

Table 4.1: The selected ($\boldsymbol{\theta_n'}$, $\boldsymbol{\alpha_n'}$) for different ($\boldsymbol{\theta_n}$, $\boldsymbol{\alpha_n}$) in different regimes. The datum coordinate systems intervals are 15°, 10° and 5° in regime#1, regime#2 and regime#3.

Regime #1 $Max\ Diff.\sim 7.5°$				**Regime #2** $Max\ Diff\sim 5°$)				**Regime #3** $Max\ Diff\sim 2.5°$			
θ_n	θ_n'	α_n	α_n'	θ_n	θ_n'	α_n	α_n'	θ_n	θ_n'	α_n	α_n'
0°: 15°	7.5°	0°: 15°	7.5°	0°: 10°	5°	0°: 10°	5°	0°: 5°	2.5°	0°: 5°	2.5°
15°: 30°	22.5°	15°: 30°	22.5°	10°: 20°	15°	10°: 20°	15°	5°: 10°	7.5°	5°: 10°	7.5°
…	…	…	…	…	…	…	…	…	…	…	…
165°: 180°	172.5°	75°: 90°	82.5°	170°: 180°	175°	80°: 90°	85°	175°: 180°	177.5°	85°: 90°	87.5

Table 4.1 includes (θ_n,α_n) and (θ_n',α_n') for different selected interval angles between the first axis of datum coordinate system: (i) regime #1 with interval angle of 15°, (ii) regime #2 with interval angle of 10° and (iii) regime #3 with interval angle of 5°. In the first and second columns, the ranges of the obtained θ_n from Equation (4.12) and corresponding θ_n' are tabulated. In third and fourth columns, the ranges of obtained α_n from Equation (4.12) and corresponding α_n' are also tabulated. The group of elements with the same θ_n' and $\alpha_n'$are collected in an elements set. A material coordinate system with the first axis parallel to the closest first axis of datum coordinate system (θ_n' and α_n') is assigned to each element set. A set of elements with the parallel material coordinate axes are highlighted with red color in a FE model as shown in Figure 4.5. The first, second and third axes are shown with blue, orange and yellow colors, respectively.

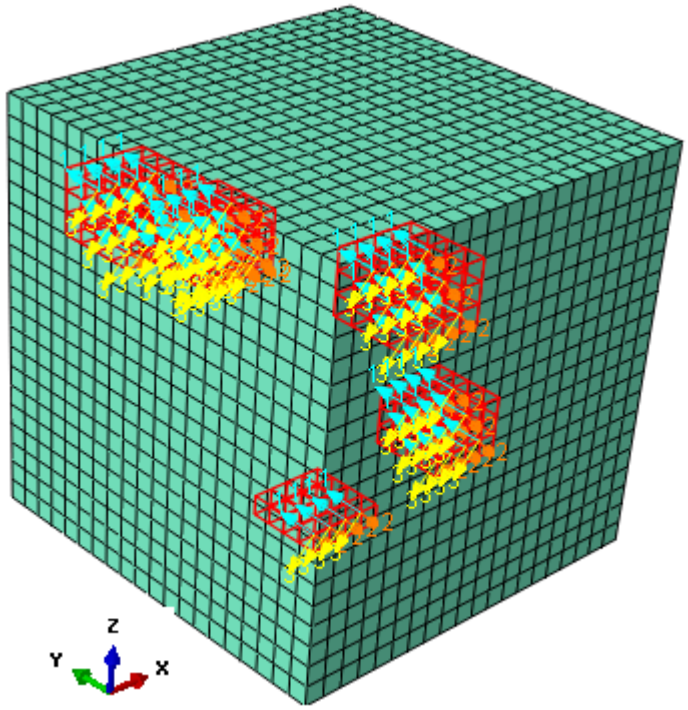

Figure 4.5: A set of FE elements with the same principal anisotropic directions are highlighted in the image.

e) The sensitivity of the stresses or strains to the number of independent material coordinate systems has been investigated to select the number of independent material coordinate systems.

11) Anisotropic Young's moduli are calculated for each FE node based on the procedure introduced in Chapter 3. Anisotropic Young's moduli of cancellous and cortical parts of the bone specimens are calculated in the principal anisotropic directions by:

$$E_{1-can} = E_{a\_can}(MPa) = 1310(\rho_n + |\nabla\rho_n|.\, l)^{1.4} \ , \qquad (4.13.1)$$

$$E_{2-can} = E_{3-can} = E_{p\_can}(MPa) = 1310{\rho_n}^{1.4} \qquad (4.13.2)$$

if $\rho < 1.04\left(\frac{g}{cm^3}\right)$; and

$$E_{1-cor} = E_{a\_cor}(MPa) = 14261(\rho_n + |\nabla\rho_n|.\, l) - 13430 \ , \qquad (4.14.1)$$

$$E_{2-can} = E_{3-can} = E_{p\_cor}(MPa) = 14261\rho_n - 13430 \ , \quad (4.14.2)$$

if $\rho > 1.04 \left(\frac{\mathrm{g}}{\mathrm{cm}^3}\right)$.

where $\rho_n + |\nabla\rho_n|.l$ can be re-expressed in the voxel coordinate system by:

$$\rho_n + |\nabla\rho|.l = \rho_n + \rho'_{nx}.x + \rho'_{ny}.y + \rho'_{nz}.z. \quad (4.15)$$

The aforementioned eleven steps are used to generate two main outputs. The first output of in-house MATLAB codes is a matrix (Node Matrix) that made of six columns and its row is equal to the numbers of FE nodes as shown:

$$\begin{bmatrix} Node\ No.\ ,\ X\ coord.\ ,\ Y\ Coord.\ ,\ Z\ Coord.\ ,\ E_p\ ,\ E_a \\ . \\ . \\ . \\ . \end{bmatrix},$$

where *Node No.* (node number), *X Coord.* (X coordinate of the node), *Y Coord.* (Y coordinate) and *Z Coord.* (Z coordinate) are determined in Step 7. *Ep* (Young's modulus in the plane of isotropy) and *Ea* (Young's modulus along the axis of symmetry) are calculated in Step 11.

The second main output of the in-house MATLAB codes is a matrix (Element Matrix) consisting of FE elements information including FE elements numbers, corresponding node numbers and material coordinate system numbers.

$$\begin{bmatrix} Element\ No.\ ,\ First\ Node\ No.\ ,\ldots Eight\ Node\ No\ ,\ Mat.Coord.Sys.No. \\ . \\ . \\ . \\ . \end{bmatrix},$$

where *Element No.* (Element number) and the corresponding node numbers were determined in Step 7; and $Mat.Coord.Sys.No$ (material coordinate system number) are determined in Step 10.

4.1.2 Abaqus Input Files

Abaqus input files are generated to construct both isotropic and anisotropic FE models from the MATLAB code outputs. To map the inhomogeneous bone mechanical properties onto the mesh in the Abaqus program, material properties are required to be field variable-dependent. Application of different temperatures (T) at the nodes of a structural element results in a variable material property distribution within the element of isotropic FE models in the Abaqus program. However, two field variables, FV1 and FV2, are used in the anisotropic model to map the anisotropic and inhomogeneous bone mechanical properties onto the FE meshed model. Hence, temperatures (T) in isotropic models are used as auxiliary variables to apply inhomogeneous isotropic Young's modulus; and the field variables (FV1 and FV2) in the anisotropic models are used as auxiliary variables to apply inhomogeneous anisotropic Young's moduli and shear moduli to FE models. The algorithm to create an input file for isotropic and anisotropic FE models is mostly the same. In this study, the steps required for generating isotropic and anisotropic FE models are indicated by **Isotropic** and **Anisotropic**, respectively. Assignment of inhomogeneous isotropic and anisotropic elasticity constants for a given FE mesh is divided into several sub-steps.

a) Isotropic:

1) To read the nodal numbers and coordinates from the Node Matrix
2) To read the FE elements numbers and their corresponding node numbers from the Element Matrix and assign 8-node Brick (C3D8) element type to all of them.
3) To read isotropic Young's modulus from the Node Matrix and apply it as temperature in the finite element model. Set the relationship between Young's modulus and applied temperature in the form of E(T)=T in the finite element model. The isotropic Poisson's ratio of 0.3 was assigned to FE elements [43, 55, 85].

b) Anisotropic:

1) To read the nodal numbers and coordinates from the Node Matrix
2) To read the FE elements numbers and their corresponding node numbers from the Element Matrix and assign 8-node Brick (C3D8) element type to all of them.
3) To define material coordinates axes (principal anisotropic directions) for each element by reading the Element Matrix.
4) To read the anisotropic Young's moduli from the Node Matrix and apply them as FV1 and FV2 in the FE model. Set the relationship between Young's moduli and the applied field variables in the form of:
    - *Ea(FV1,FV2)=E1(FV1,FV2)=FV1*
    - *Ep(FV1,FV2)=E2(FV1,FV2)=FV2*
    - *Ep=E3(FV1,FV2)=FV2.*

5) To assign constant Poisson's ratios to the anisotropic EF models ($\upsilon_{ap} = \upsilon_{12} = \upsilon_{13} = 0.25$ and $\upsilon_P = \upsilon_{23} = 0.4$) [81].
6) To set the relationship between shear moduli and applied field variables using the set of Equations (3.12) in the form of:
    - *Ga(FV1,Fv2)=G12(FV1,FV2)=FV1/(2(1+0.25))*
    - *Ga(FV1,FV2)=G13(FV1,FV2)=FV1/(2(1+0.25))*
    - *Gp=G23(FV1,FV2)=FV2/(2(1+0.4)).*

The above procedure employs the in-house Matlab codes and the Abaqus input file to construct both the isotropic and anisotropic FE models.

4.2 Virtual Compression Tests

Nine virtual specimens were extracted from CT image of human femur head of female adult. The images were taken on 11th of July 2013 with SIMENS S5VB40B CT scan machine by WINNIPEG PET/CT Center. Figure 4.6 shows the approximate locations of the specimens in longitudinal and transverse views. As hip fractures mostly occur at three different locations of the femur – the femoral neck, intertrochanteric and subtrochanteric regions, the specimens are cut from those three regions. The dimensions of cubic specimens have been reported to be between 4.5 mm and 10 mm in compression tests in the literature [22, 91-93]. The dimensions of cubic specimens were selected to be 5 mm in this study.

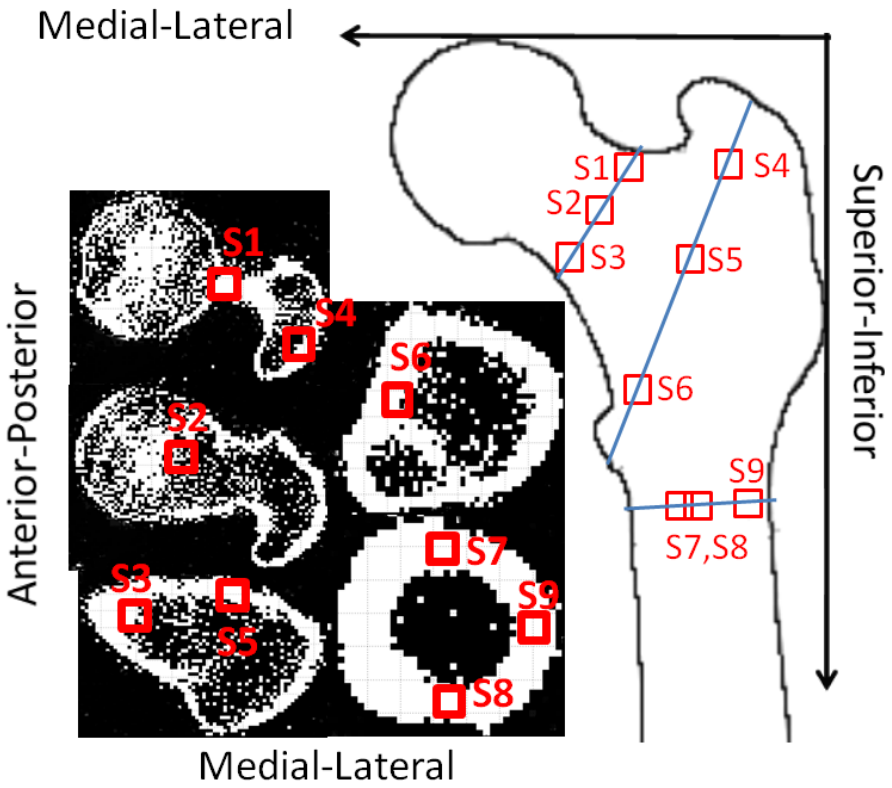

Figure 4.6: The locations of the specimens in longitudinal and transverse views. The virtual specimens were cut from neck, intertrochanteric and subtrochanteric parts of femur.

The isotropic and pointwise anisotropic material properties were assigned to the finite elements models. A displacement of 0.05mm in the compression direction was applied on three surfaces one by one. The nodes located in opposite surfaces were fixed in the direction of compression load as shown in Figure 4.7. The isotropic and pointwise anisotropic material properties were assigned to the finite elements models; the FE models were runned and the results were recoreded. In next chapter, the results are presented and discussed. To determine an adequate number of elements, a convergence study was also performed. In anisotropic FE models, sensitivity analysis was also performed to determine the number of material coordinate systems that represent pointwise transversely isotropic with a good approximation.

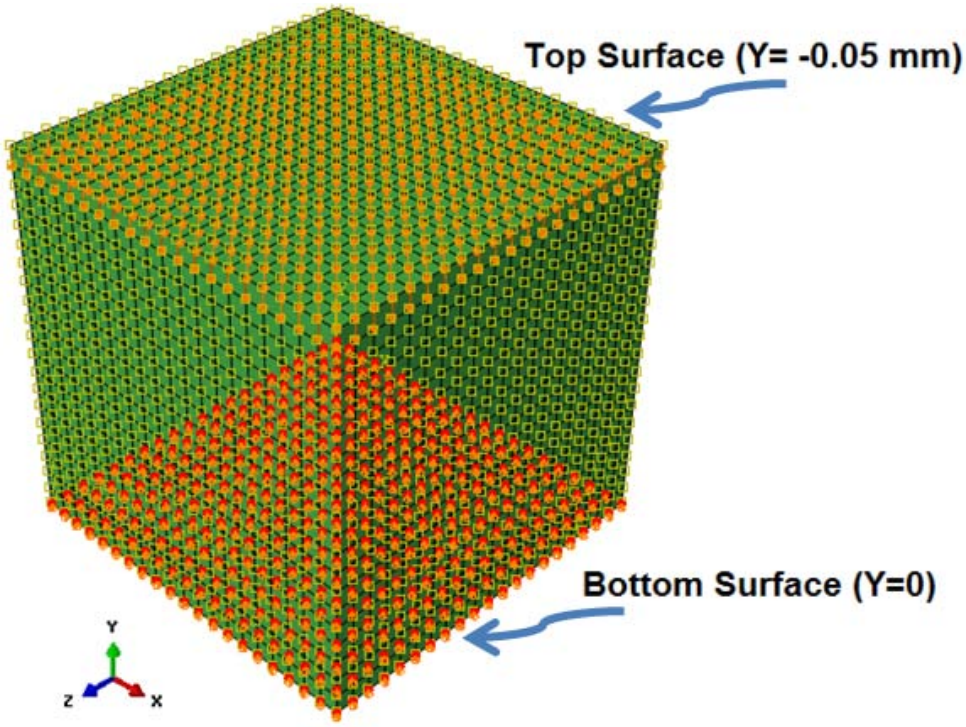

Figure 4.7: The node displacement (0.05 mm) is applied on the top surface of the specimen. For the nodes located on the bottom surface of the specimens, the degree of freedom in Y direction is fixed.

4.3 Accuracy evaluation of anisotropic versus conventional isotropic model

The material properties of a FE model constructed from high resolution of CT image is closer to real properties of bone in comparison with a FE model constructed from low resolution. Here, we construct the isotropic FE models of nine specimens from both a clinical CT image (high resolution) and a Coarse CT image (low resolution); and the results of FE analyses are recorded. The relative errors generated due to the low resolution of the Coarse CT image are calculated. Then, the anisotropic FE models of the same nine specimens are also constructed from the Coarse CT image. The results of the

FE analyses are recorded and compared with the isotropic FE models of clinical CT image. Reducing the relative errors due to the low resolution of the Coarse CT image by considering the anisotropy could proof the higher accuracy of the anisotropic model in comparison with the isotropic model as schematically is shown in Figure 4.8.

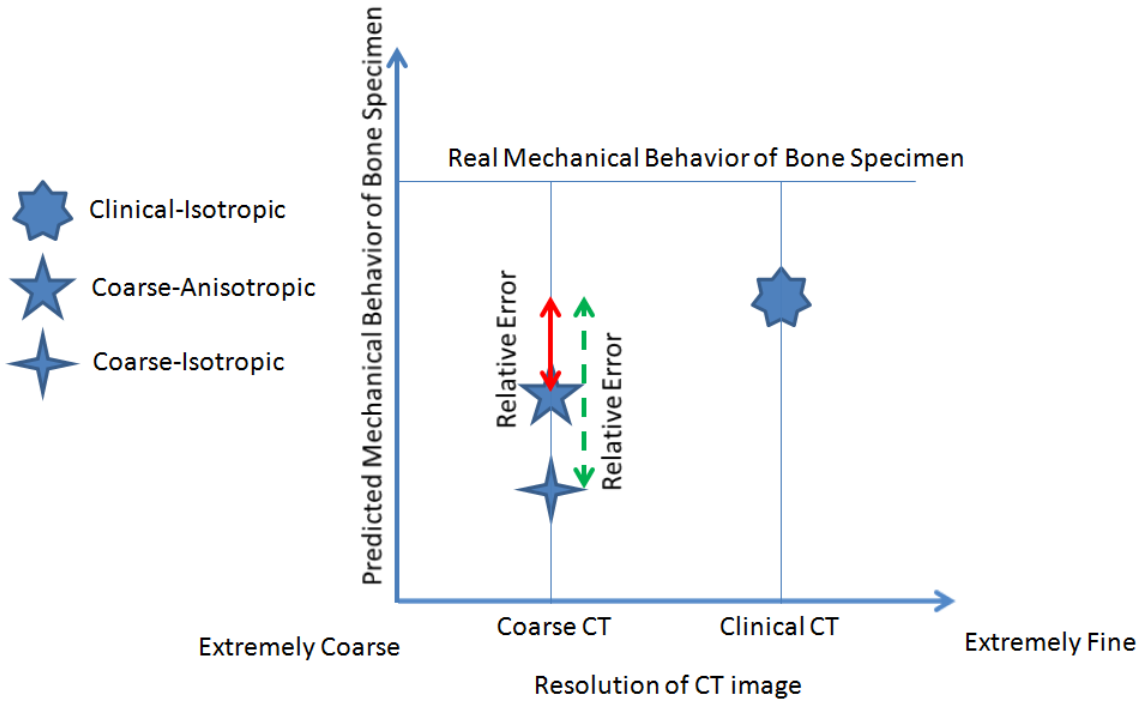

Figure 4.8: The predicated mechanical behaviour of bone specimens with respect to the resolution of CT images.

Here, a method is defined to create a coarse CT image from the clinical CT image, which was taken by WINNIPEG PET/CT Center as mentioned earlier. Each coarse voxel is constructed of eight voxels of the clinical CT image in the close proximity. The total masses of the combined clinical CT image voxels are assigned to the coarse voxel to conserve the total mass of the human femur head. As a linear correlation between a CT number and bone apparent density has been established, the following correlation is

derived to quantify the CT number of each coarse voxel as a function of the CT number of the clinical voxels:

$$CT_{Coarse\ Voxel}(HU) = \frac{CT_1(HU)+CT_2(HU)+\cdots+CT_8(HU)}{8}, \quad (4.16)$$

where $CT_1(HU)$, $CT_2(HU)$, …$CT_8(HU)$ represent a set of clinical image voxels which are used to construct the coarse voxel. The coarse voxel consisting of eight clinical voxels is shown in Figure 4.9. The voxels of the coarse CT image are rectangular hexahedron in shape with 0.2048×0.2048×1.4 mm in length (with dimensions twice of the clinical CT image voxel).

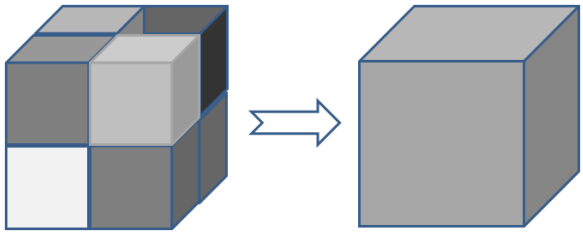

Figure 4.9: A small specimen constructed of a coarse voxel or eight clinical voxels

When the coarse CT image is constructed, the following procedure was developed to evaluate accuracy of the defined anisotropic model to predict mechanical behaviour of bone in comparison with the isotropic model:

(1) Nine small virtual specimens are cut from the clinical CT image of neck, intertrochanteric and subtrochanteric regions of femur head. The corresponding virtual specimens are also cut from the coarse CT image. The small virtual specimens are cubic shaped with 1.3 mm dimensions and each one of them is made of one coarse CT voxel or eight clinical CT voxels (Figure 4.9).

(2) Three types of finite element (FE) models are constructed for each small specimen. Isotropic and anisotropic types of FE models are generated from the virtual coarse CT

image (“Coarse-isotropic model” and “Coarse-anisotropic model”). The isotropic FE models of small specimens are constructed from the clinical CT image (“Clinical-isotropic model”).

(3) A displacement of 0.13 mm in the direction of compression is applied on a surface of each FE model of the specimens. The displacement is individually applied on all three main anatomical orientations.

(4) The results of “Clinical-isotropic” FE models are the reference values (the most accurate results). The maximum von Mises stresses and absolute principal strains obtained from Coarse-isotropic and Coarse-anisotropic FE analyses are compared with corresponding Clinical-isotropic FE analyses. The results of the comparison are used to verify the higher accuracy of the anisotropic model versus conventional isotropic model.

Chapter 5

Results and Discussion

In this chapter the following results are presented: (i) the principal anisotropic directions in the frontal, sagittal and transverse planes of the virtual specimens, (ii) the verification tests of the isotropic and anisotropic FE analyses of the specimens and (iii) comparison of the maximum von Mises stresses and the absolute principal strains in two types of FE analyses.

5.1 Anisotropy in Bone Specimens

In order to determine the principal anisotropic directions, the density gradient must be determined at each point of the virtual specimens using MATLAB. To assess the accuracy of the MATLAB codes to determine the gradient, it was applied to a grid data generated from a 3D analytical function. The results and relevant errors are discussed in next section.

5.1.1 Validation of the MATLAB Code

The gradient obtained using Equation (4.8) was compared with the gradient calculated based on the second-order finite difference method. A set of discrete grid data were garneted over the function domain (Equation (4.4)) with constant "0.1 unit" distance. Two hundred seventy evaluation points were selected among the generated discrete data; and both the analytical and the numerical gradients were calculated and compared. The root mean square error (RMSE) and the coefficient of variation of the RMSE (CV(RMSE)) are used to measure the relative errors of the numerical method with respect to the analytical method.

$$RMSE(\nabla f) = \sqrt{\frac{\sum_1^n (\nabla f_{numercial} - \nabla f_{analytical})^2}{n}} \text{ and} \tag{5.1}$$

$$CV(RMSE(\nabla f)) = \frac{RMSE(\nabla f)}{\nabla f_{analytical}}. \tag{5.2}$$

Figure (5.1) illustrates the gradient vectors based on both the analytical and the finite difference method. The results of analytical calculation are consistent with the results of the finite difference solutions. The dimensions of the gradient vectors of the two methods were also compared. The calculated $CV(RMSE(\nabla f))$ was 0.108 (10.8%), which shows fairly acceptable performance of the finite difference method to predict the magnitude of the gradient.

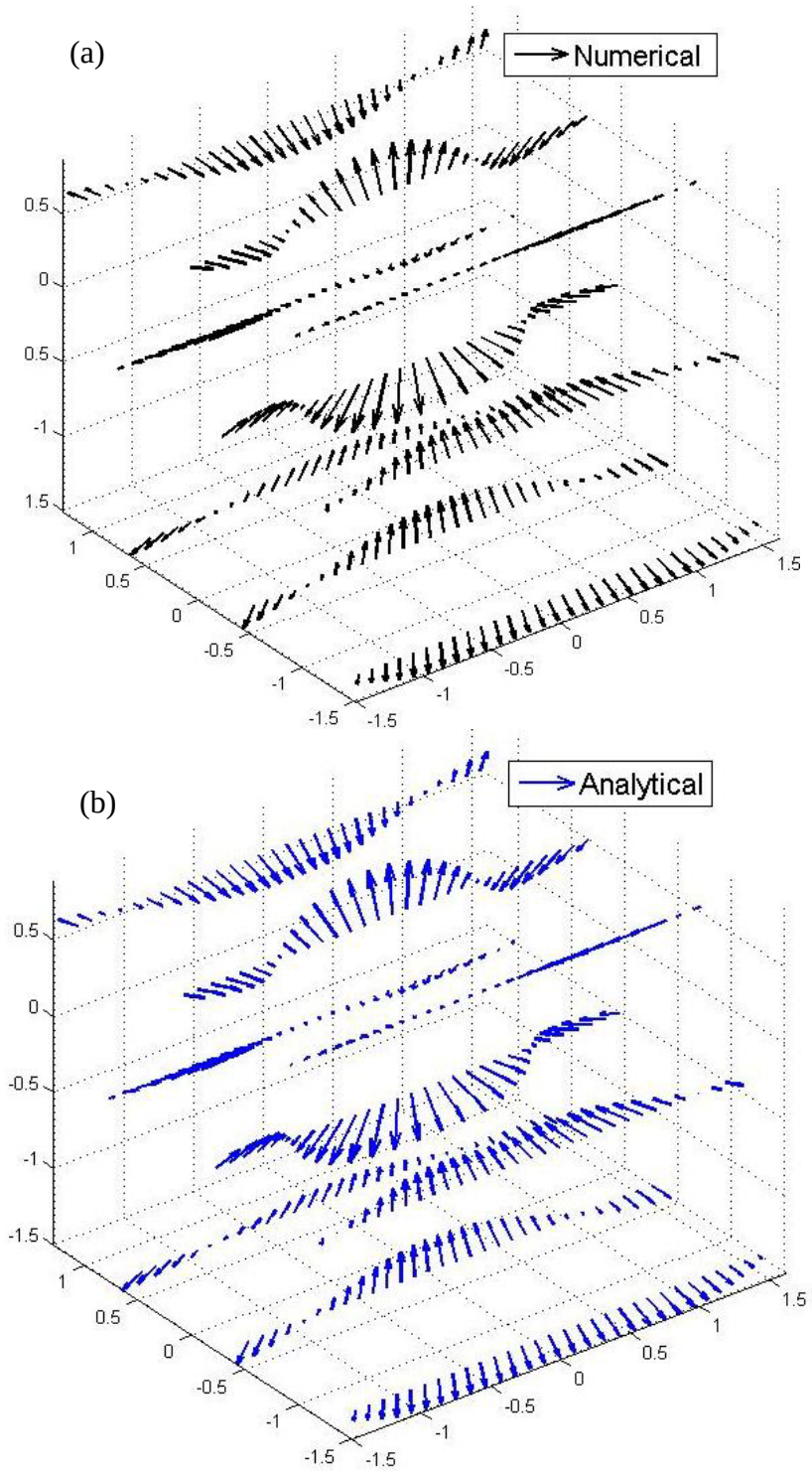

Figure 5.1: The vectors are represented the function gradient. The gradients are calculated using (a) the numerical and (b) the analytical methods.

5.1.2 Results of Principal Anisotropic Directions

The structural axis of symmetry and the orientation of the plane of isotropy (the principal anisotropic directions) are determined based on the calculation of density gradients in the midsections of specimens. The midsections of specimens are selected parallel to frontal, sagittal and transverse planes as shown in Figure 5.2.

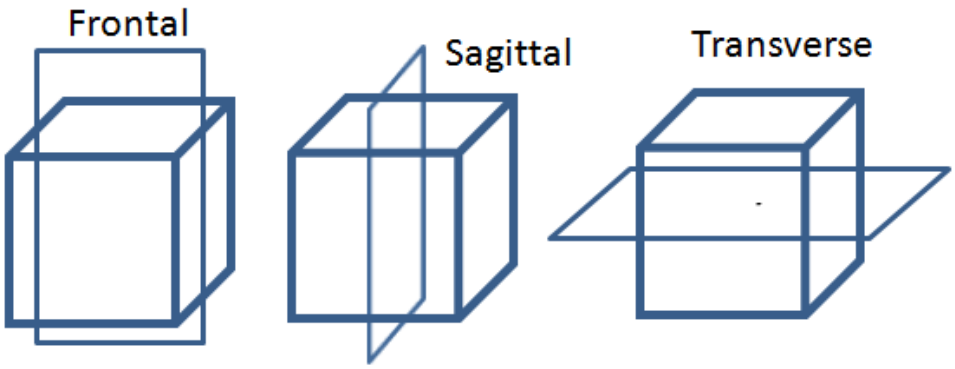

Figure 5.2: The midsections of bone specimens

The length of vectors represents the density gradient, whereas the directions of the vectors represent the orientations of the planes of isotropy in Figures 5.3, 5.4 and 5.5. The orientations and the density gradient are highly variable in the femoral neck specimens (S1, S2 and S3). The density gradients are significant in the proximity of the bone surface of the specimens donated by S1 and S2. The planes of isotropy are also parallel to the bone surface near the bone surface for the specimens represented by S1 and S2. Most of the planes of isotropy are parallel to the femur shaft axis in the inferior side of the femoral neck (S3). However, the majority of planes of isotropy are parallel to the neck axis in the superior side the femoral neck (S1).

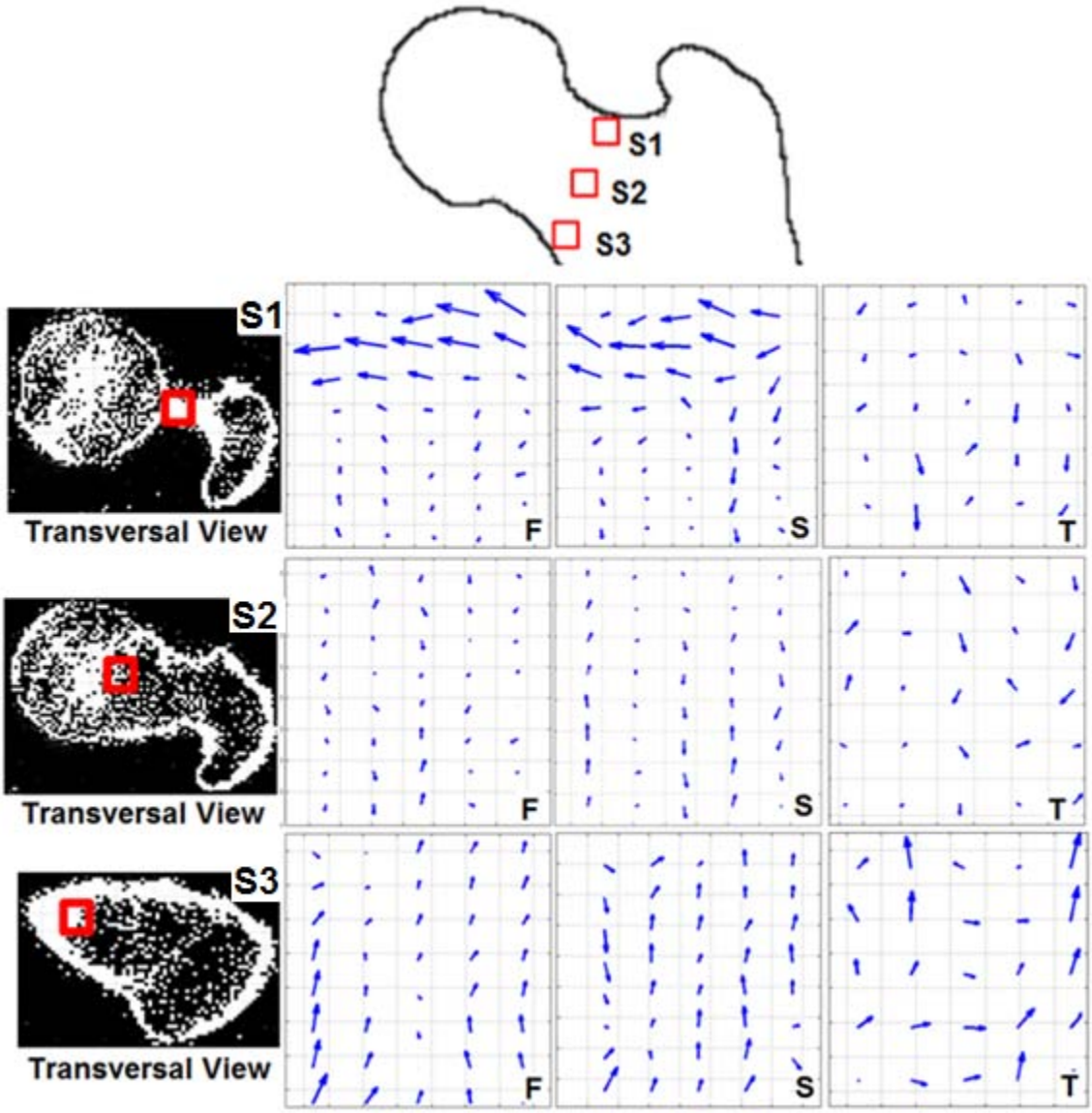

Figure 5.3: The plane of isotropy directions (the orientations of the blue vectors) and the density gradient dimension (the dimension of the blue vectors) are shown in three different sections of femoral neck specimens. F is Midsection of specimen parallel to frontal plane, S is Midsection of specimen parallel to sagittal plane and T is midsection of specimen parallel to transverse plane. Distance between every gridline was set to be 0.36 of a unit of density gradient.

Figure 5.4 illustrates the planes of isotropy directions and density gradient in intertrochanteric specimens. Similar to the neck specimens, the orientations of anisotropy are highly variable in the intertrochanteric specimens (S4, S5 and S6).

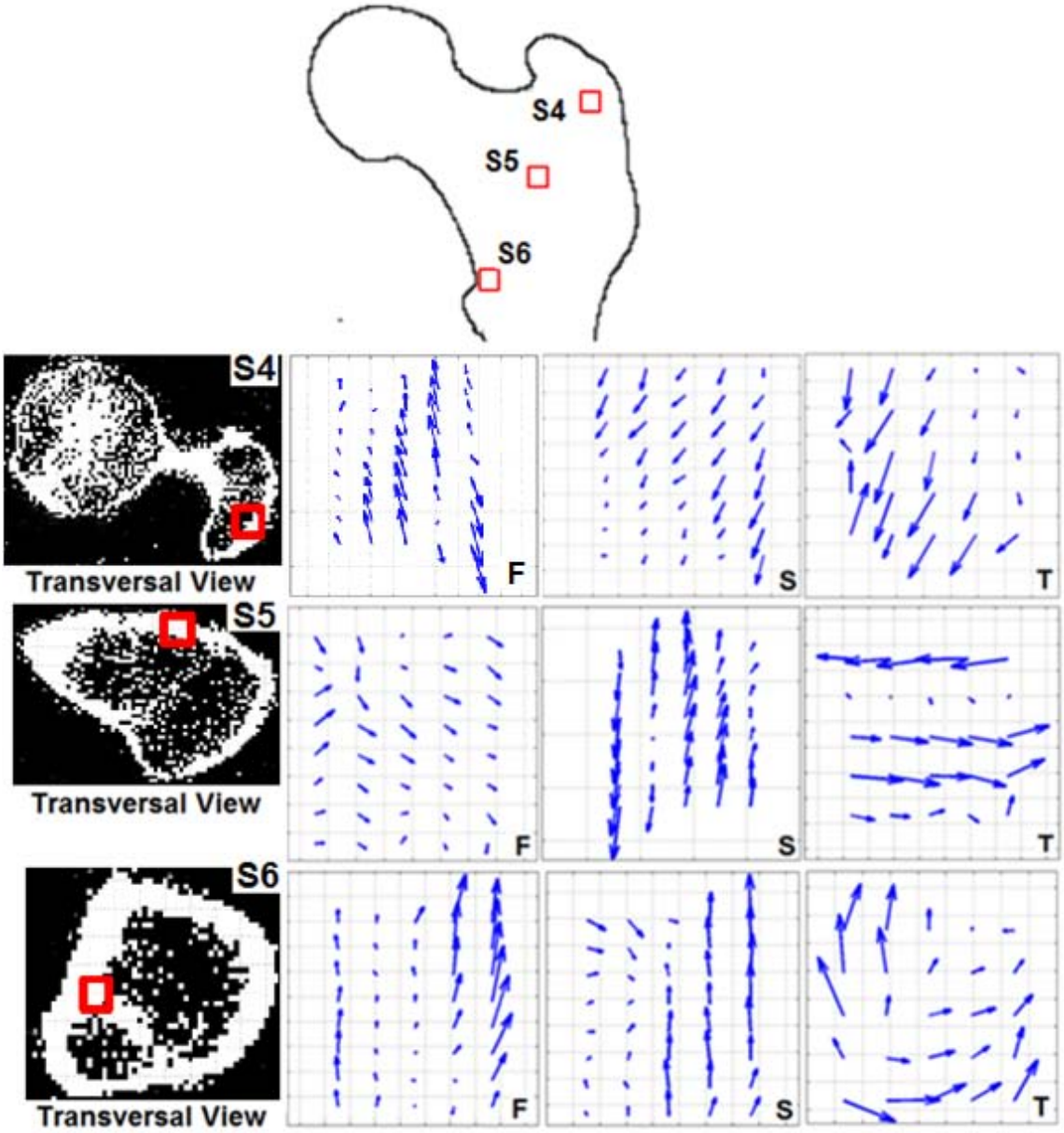

Figure 5.4: The plane of isotropy directions (the orientations of the blue vectors) and the density gradient dimension (the dimension of the blue vectors) are shown in three different sections of intertrochanteric specimens. F is Midsection of specimen parallel to frontal plane, S is Midsection of specimen parallel to sagittal plane and T is midsection of specimen parallel to transverse plane. Distance between every gridline was set to be 0.36 of a unit of density gradient.

In the superior part of intertrochanteric region of femur (S4), the planes of isotropy are pointed at the greater intertrochanteric axis in the longitudinal sections. However, the planes of isotropy are pointed at femur head in the center of intertrochanteric region (S5).

In the distal side of the region (S6), the planes of isotropy are parallel to the femur shaft in the longitudinal section, whereas the planes of isotropy are parallel to the bone surface in the transverse sections.

Figure 5.5 illustrates the planes of isotropy directions and the bone density gradient in subtrochanteric region. The orientations of anisotropy are less diverse in the subtrochanteric specimens in comparison with the other regions. Most of the planes of isotropy are parallel to the femur shaft in subtrochanteric specimens, whereas they were parallel to the circumferential direction of femur shaft in the transverse sections. The bone density gradient is larger close to the bone surface.

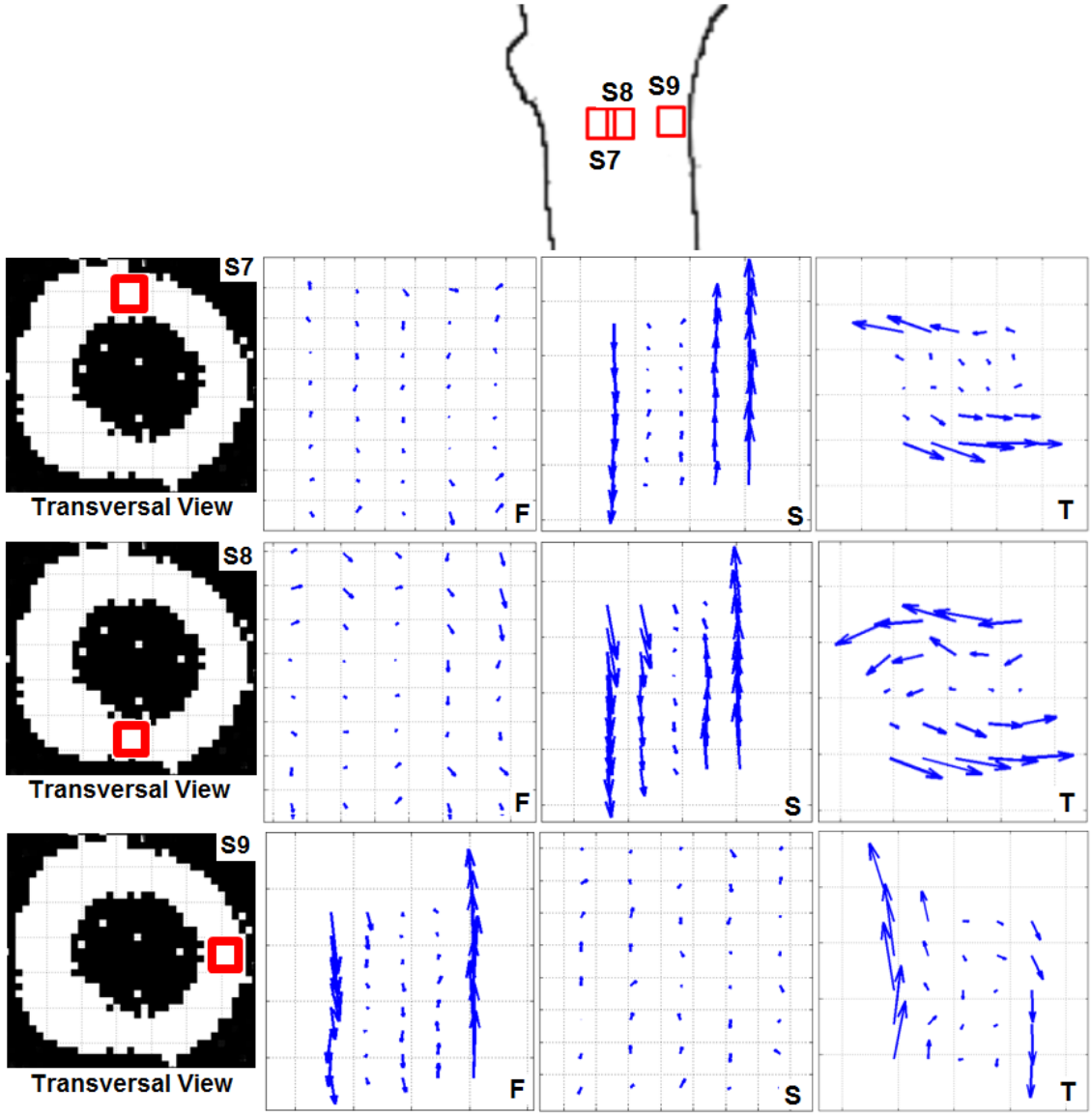

Figure 5.5: The plane of isotropy directions (the orientation of the blue vectors) and the density gradient dimension (the dimension of the blue vectors) are shown in three different sections of subtrochanteric specimens. F is Midsection of specimen parallel to frontal plane, S is Midsection of specimen parallel to sagittal plane and T is midsection of specimen parallel to transverse plane. Distance between every gridline was set to be 0.36 of a unit of density gradient.

5.1.3 The Magnitude of Young's Modulus in bone specimens

In the anisotropic FE model, Young's modulus in the direction of the plane of isotropy was calculated using the equation of isotropic Young's modulus. Isotropic Young's

modulus was calculated using Equations (4.13.2) and (4.14.2) as the function of bone density. In the anisotropic FE model, Young's modulus in the direction of the axis of symmetry was calculated as the function of bone density and density gradient using Equations (4.13.1) and (4.14.1).

To discuss the variation of Young's modulus, the variation of bone density was investigated in different regions in the first step. To quantify the variation of bone density, *relative difference* parameter was calculated for each specimen in Equation (5.3). The minimum, maximum and mean densities are required for each specimen to calculate the *relative difference* parameter. The results are recorded in Table 5.1.

$$Relative\ Difference = \left[\frac{(density_{min} - density_{mean})}{density_{mean}} \times 100 \ \ to \ \ \frac{(density_{max} - density_{mean})}{density_{mean}} \times 100\right], \quad (5.3)$$

Table 5.1: The minimum, maximum and mean nodal density; and relative differences of density in the specimens.

	Min. Density gr/cm^3	Max. Density gr/cm^3	Mean Density gr/cm^3	Relative differences (%)
Neck 1 (S1)	0.032	1.532	0.5859	[-94.5 to 161.5]
Neck 2 (S2)	0.032	0.7256	0.3356	[-90.5 to 116.2]
Neck 3 (S3)	0.032	1.3568	0.5957	[-94.6 to 127.8]
Int. 1 (S4)	0.032	2.1176	0.7896	[-95.9 to 168.2]
Int. 2 (S5)	0.0896	1.8608	1.0825	[-91.7 to 71.9]
Int. 3 (S6)	0.5	2.6516	1.5612	[-68 to 70]
Sub. 1 (S7)	0.824	2.4044	1.7651	[-53.3 to 36.2]
Sub. 2 (S8)	0.4736	2.0984	1.4396	[-67.1 to 45.8]
Sub. 3 (S9)	1.1168	2.4428	1.9308	[-42.2 to 26.5]

The highest mean density occurred in the subtrochanteric specimens (Table 5.1) and is in a good agreement with the values found in literature [26, 27]. The results also demonstrate that the maximum variation of bone density takes place in the femoral neck specimens.

The variation of bone density causes the variation of the nodal isotropic Young's modulus in each bone specimen, since an exponential (for cancellous bone) or linear (for cortical bone) elasticity-density correlation has been utilized to calculate the modulus. The *relative difference* of Young's modulus with respect to its mean value was calculated in each specimen and the results are provided in Table 5.2. The highest Young's modulus is in the subtrochanteric region and the lowest is in femoral neck regions.

Table 5.2: The minimum, maximum and mean nodal isotropic Young's modulus in the specimens

	Min. E. Mpa	Max. E. Mpa	Mean E. Mpa	Relative differences (%)
Neck 1 (S1)	10	8418	620	-98% to 1258%
Neck 2 (S2)	10	836	284	-96% to 194%
Neck 3 (S3)	10	5919	634	-98% to 833%
Int. 1 (S4)	10	16769	941	-99% to 1682%
Int. 2 (S5)	45	13107	1464	-97% to 795%
Int. 3 (S6)	496	24384	8834	-94% to 176%
Sub. 1 (S7)	999	20859	11742	-91% to 78%
Sub. 2 (S8)	460	16495	7100	-93% to 132%
Sub. 3 (S9)	1529	21407	14105	-89% to 52%

The mechanical anisotropy ratio is the ratio of the maximum to the minimum Young's modulus at a node. Table 5.3 lists the ranges of mechanical anisotropy ratios for all the specimens. Among all the specimens, the highest maximum anisotropy ratio (3.39) is in the femoral neck specimen (S3).

Table 5.3: The minimum, maximum, mean values of the mechanical anisotropy ratios in the specimens.

	Mean Mech. Aniso. Ratio	Max Mech.Aniso. Ratio
Neck 1 (S1)	1.3057	2.4567
Neck 2 (S2)	1.2987	2.6777
Neck 3 (S3)	1.2616	3.3936
Int. 1 (S4)	1.4469	3.3324
Int. 2 (S5)	1.3477	2.724
Int. 3 (S6)	1.2564	1.842
Sub. 1 (S7)	1.2109	1.824
Sub. 2 (S8)	1.3536	2.184
Sub. 3 (S9)	1.1541	1.915

5.2 Virtual Tests Using Finite Element Analysis

The verification results of the isotropic and anisotropic FE analyses are presented in this sub-section. The results of the virtual compression tests on the specimens using both the isotropic and anisotropic FE models are also tabulated and discussed in the following sub-sections. In addition, the results of the accuracy evaluations associated with the anisotropic vs. isotropic FE models are presented.

5.2.1 Verification of Isotropic Finite Element Analysis

To verify the isotropic FE analyses the following steps were performed: (i) convergence test, (ii) checking the force equilibrium and (iii) checking the accuracy of boundary conditions.

Convergence Test

The convergence tests of the FE models were performed as a part of the verification. A suitable mesh size should be determined based on the results of convergence tests. The variation of the maximum von Mises stresses and the maximum absolute principal strains with respect to the numbers of nodes in the specimen (S3) are shown in Figure 5.6. The results show that 9261 FE nodes and 8000 FE elements are sufficient to obtain acceptable results by the isotropic models of FE analyses.

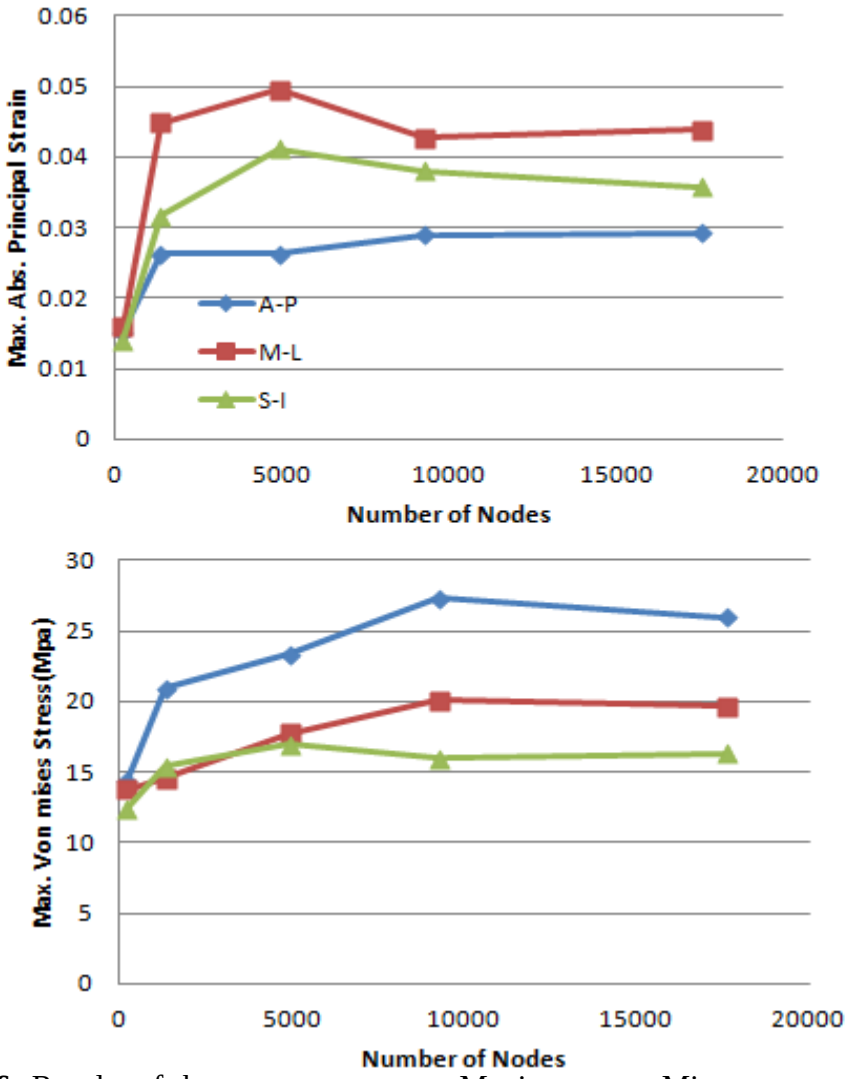

Figure 5.6: Results of the convergence test. Maximum von Mises stresses and absolute principal strains of the isotropic FE model of the specimen (S3) versus number of nodes.

Checking the force equilibrium

The force equilibrium must be satisfied. The reaction forces on the surfaces of the isotropic FE model of the specimen (S3) were calculated under the compression load in S-I direction (Z axis direction). The distribution of the nodal reaction forces in the bottom and top surfaces of the specimen (Z direction) is shown in Figure 5.7.

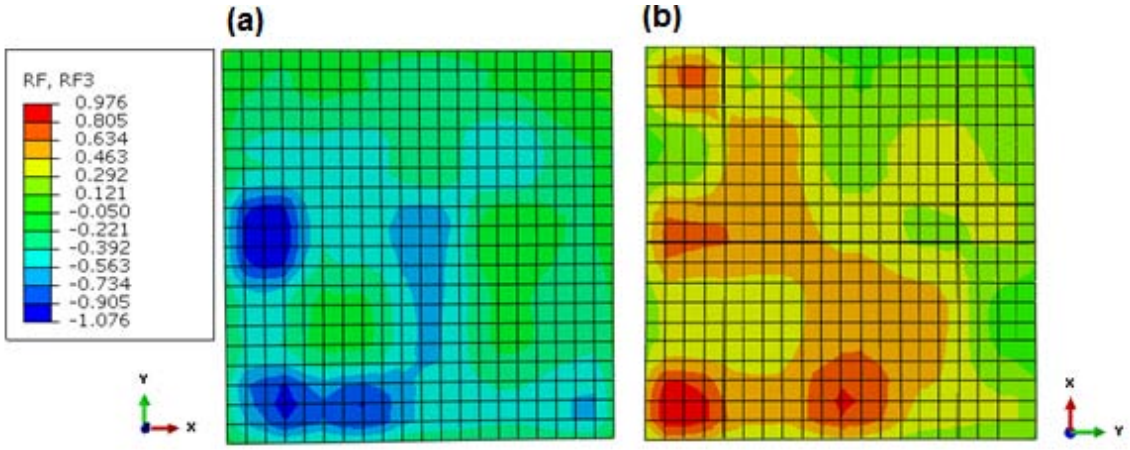

Figure 5.7: The contours show reaction forces in (a) the bottom and (b) the top surfaces of the specimen (S3).

The resultant reaction forces of the model in Z direction were equal to 163.581 N; and they were the same in the top and the bottom surfaces of the specimen. In addition, the resultant reaction forces on the top and the bottom surfaces were zero in X and Y directions. Therefore, the force equilibrium is satisfied in the FE model. The same procedure was also performed for all the specimens to check the force law of equilibrium.

Checking of boundary conditions

Figure 5.8 shows the nodal displacement of the specimen (S3) under virtual compression loading condition. The nodal displacement of the finite element model (Figure 5.8) verified that boundary conditions (Figure 4.7) were applied accurately. The displacements of the top and bottom surfaces were respectively -0.05mm and zero, which were consistent with the expectations.

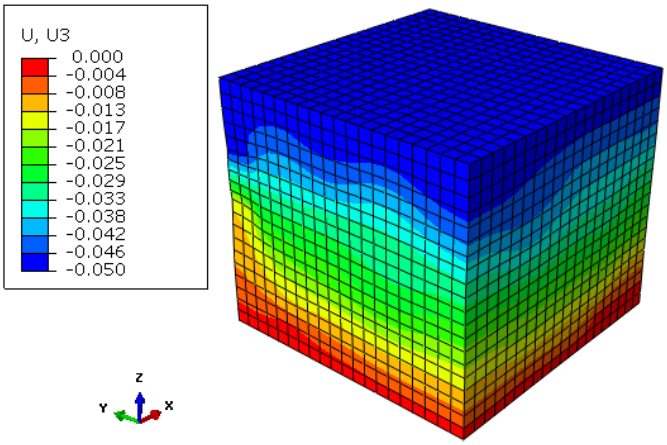

Figure 5.8: Nodal displacement of the specimen (S3) under the virtual compression load. The displacements of the top and bottom surfaces are respectively -0.05mm and zero.

5.2.2 Verification of the Anisotropic Finite Element Analysis

To verify the anisotropic FE analyses following steps were performed: (i) sensitivity analysis to find adequate numbers of material coordinate systems, (ii) convergence test, (iii) checking the force equilibrium and (iv) checking the accuracy of boundary conditions. Since third and fourth steps of the verification are the same in both isotropic and anisotropic FE analyses, only the first and the second steps are described here.

Sensitivity analysis to find adequate numbers of material coordinate systems

As it is explained in Section 4.1.1, sensitivity analysis is performed to evaluate the effects of using regime #1, regime #2 or regime #3 on the predicted stresses or strains. The maximum difference between the exact principal anisotropic directions of the elements versus the material coordinate system assigned to them is 7.5°, 5° and 2.5° by using regime #1, regime #2 and regime #3, respectively. Employing regime #1, regime #2 and regime#3 coordinate systems result in the assignments of different numbers of

independent material coordinate systems to the specimens (S3, S6 and S8) FE elements as it is shown in Table 5.4.

Table 5.4: The Number of element sets with independent material coordinates system.

	Regime#1 (Mat. Coor. Sys.)	Regime#2 (Mat. Coor. Sys.)	Regime#3 (Mat. Coor. Sys.)
S3 (Neck Spec.)	63	104	164
S6 (Int. Spec.)	51	89	156
S8 (Sub. Spec.)	42	69	129

Figures 5.9 and 5.10 show the predicted maximum von Mises stresses and the absolute principal strains obtained by employing the different regimes. The maximum difference between “regime#1 maximum principal strain” and “regime#2 maximum principal strain” is observed in the S6; and it is significant and equal to 45% (Figure 5.10). However, as it is shown in Figure 5.9 and 5.10, the “regime #2 maximum stress or strain” and the “regime #3 maximum stress or strain” is quite the same (The maximum difference is less than 6%). Therefore, regime#2 is a preferable choice for assignment of the pointwise anisotropy to optimize numerical calculations in this study.

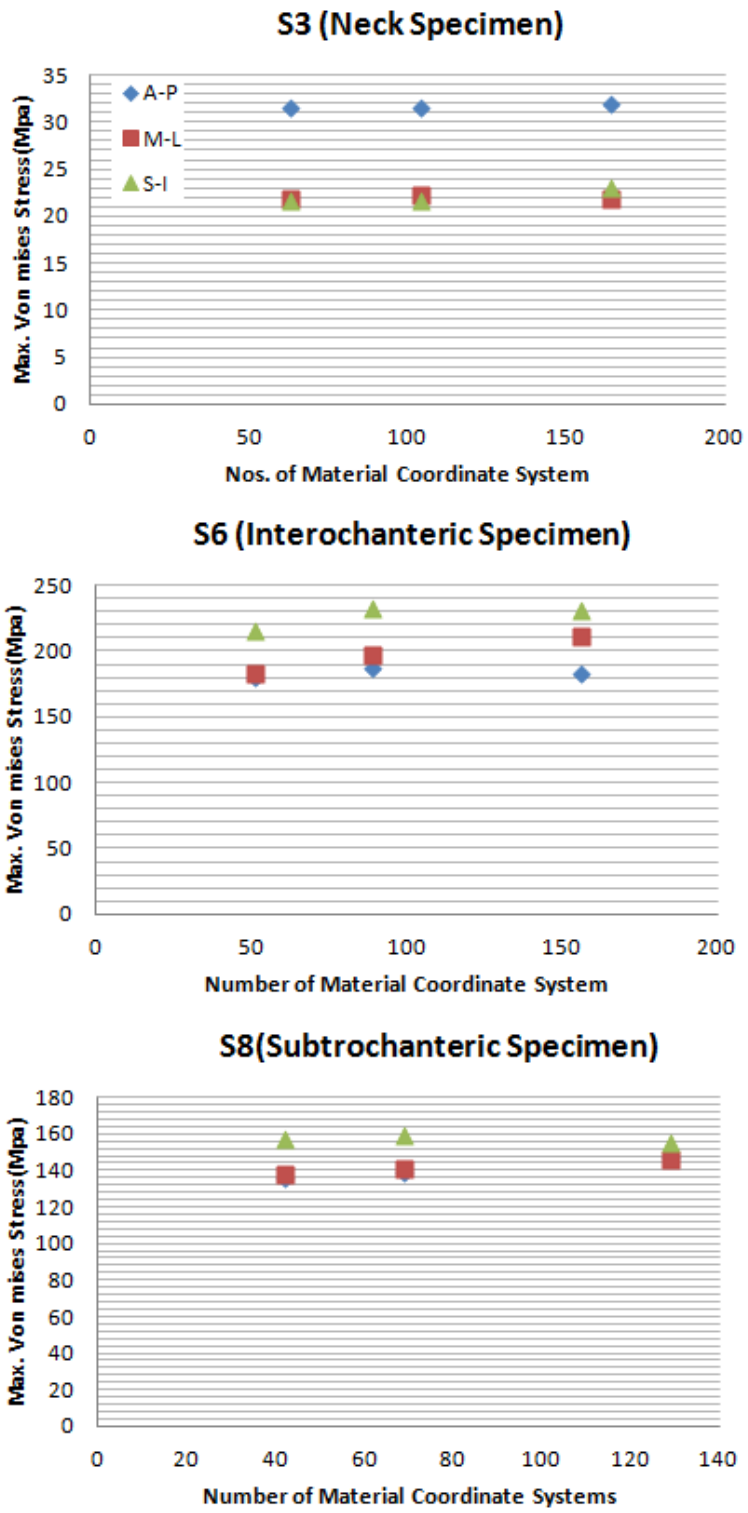

Figure 5.9: The maximum von Mises stresses versus the number of material coordinate systems for regime#1, regime#2 and regime#3.

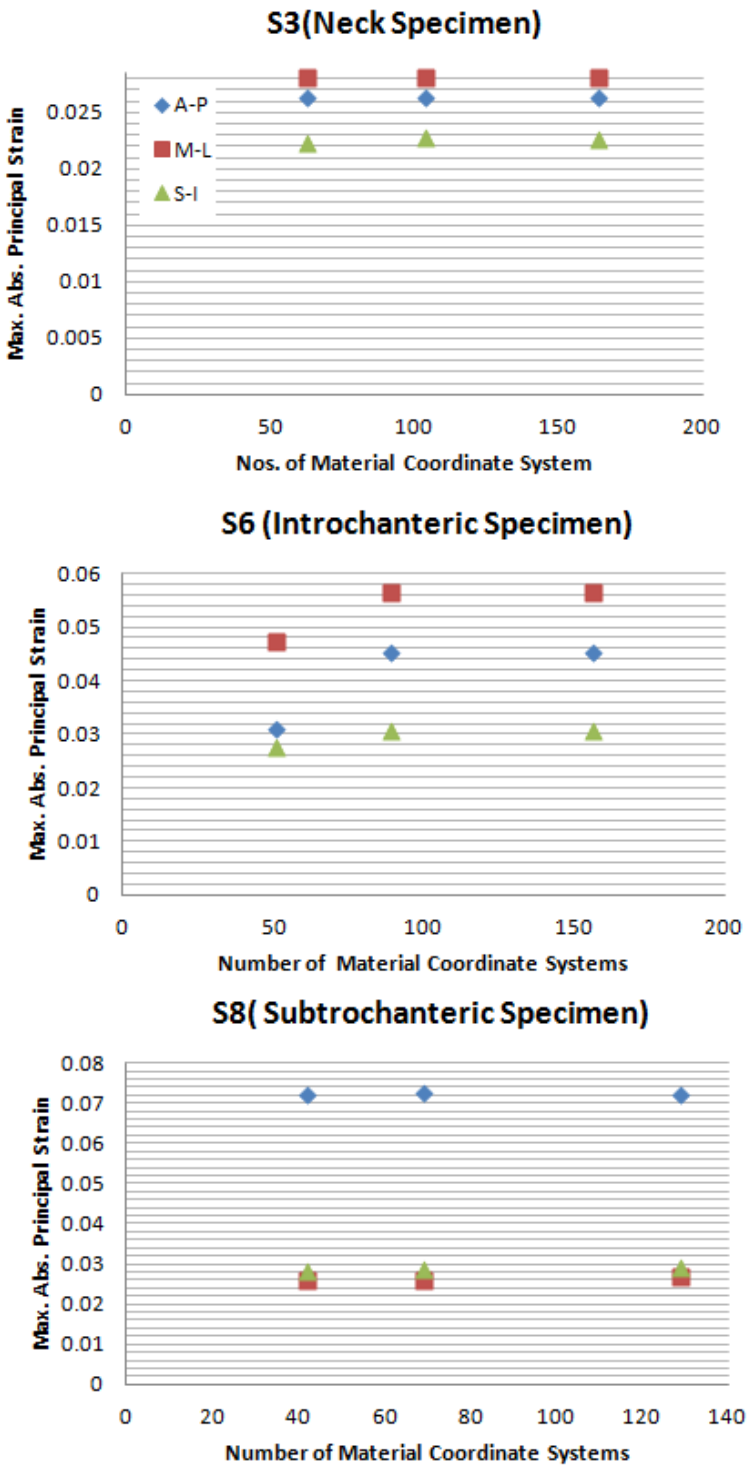

Figure 5.10: The maximum absolute principal strains versus the number of material coordinate systems for regim#1, regime#2 and regime#3.

Convergence Test

Similar to the isotropic FE models in the previous section, the convergence test must be performed in anisotropic FE models to determine the adequate numbers of FE nodes and elements to obtain precise results. The results show that 9261 FE nodes and 8000 FE elements are sufficient to obtain an acceptable value for the maximum von Mises stresses and the absolute principal strains in the anisotropic models of FE analyses as shown in Figure 5.11.

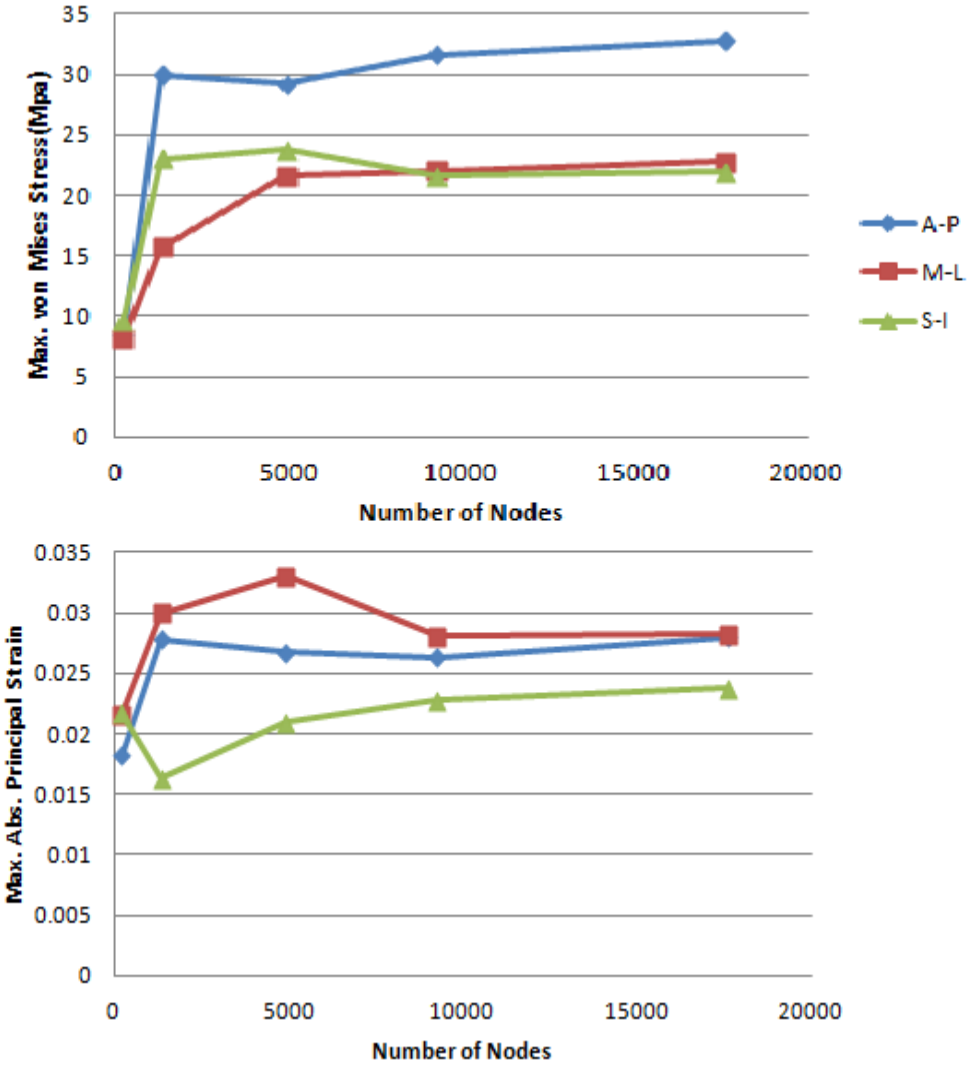

Figure 5.11: The Maximum von Mises stresses and absolute principal strains of the anisotropic FE model of the S3 specimen versus number of nodes.

5.2.3 The Maximum Absolute Principal Strains and von Mises Stresses of Virtual Specimens under Compression Load

Fifty four virtual tests were performed and the maximum von Mises stresses and the absolute principal strains were calculated and recorded in table 5.5, Table 5.6 and Table 5.7.

Table 5.5: The maximum von Mises stresses, maximum absolute principal strains and their *relative difference* in isotropic versus anisotropic FE analyses of femoral neck specimens.

Reg.	Dir.	Spec.	von Mises Stress [Mpa]		M.P.Strain		Percentage Diff.	
			ISO	ANISO	ISO	ANISO	Stress (%)	Strain (%)
Neck	A_P	1	76.3666	80.2826	0.0387	0.0323	5	-18
	M_L		92.2071	89.6229	0.0364	0.0343	-2.8	-6.1
	S_I		12.2775	13.5987	0.0447	0.0269	10.2	-49.7
	A_P	2	5.7674	7.1349	0.0327	0.0198	21.2	-49.1
	M_L		7.09981	7.4331	0.0315	0.0189	4.6	-50
	S_I		5.8532	6.83297	0.0385	0.0234	15.4	-48.7
	A_P	3	27.0876	31.4881	0.0290	0.0263	15	-9.7
	M_L		20.0141	22.3321	0.0427	0.0281	10.9	-41.2
	S_I		15.9622	21.6428	0.0380	0.0228	30.2	-50.1

Table 5.6: The maximum von Mises stresses, maximum absolute principal strains and their *relative difference* in isotropic versus anisotropic FE analyses of intertrochanteric specimens.

Reg.	Dir.	Spec.	von Mises Stress[Mpa]		M.P.Strain		Percentage Diff.	
			ISO	ANISO	ISO	ANISO	Stress (%)	Strain (%)
Intertrochanter	A_P	4	91.5113	101.099	0.0342	0.0327	10	-4.4
	M_L		25.8897	27.5382	0.0519	0.0379	6.2	-31.2
	S_I		95.1287	107.566	0.0407	0.0378	12.3	-7.4
	A_P	5	36.2008	36.775	0.0426	0.0549	1.6	25.2
	M_L		109.769	119.873	0.0249	0.0233	8.8	-6.6
	S_I		124.802	131.536	0.0705	0.0424	5.2	-49.8
	A_P	6	172.957	187.221	0.0303	0.0451	7.9	39.2
	M_L		173.414	190.166	0.0442	0.0563	9.2	24.1
	S_I		217.041	232.152	0.0241	0.0308	6.7	24.4

Table 5.7: The maximum von Mises stresses, maximum absolute principal strains and their *relative difference* in isotropic versus anisotropic FE analyses of subtrochanteric specimens.

Reg.	Dir.	Spec.	von Mises Stress[Mpa]		M.P.Strain		Percentage Diff.	
			ISO	ANISO	ISO	ANISO	Stress (%)	Strain (%)
Subtrochanter	A_P	7	187.815	186.209	0.0393	0.0615	-0.9	44
	M_L		181.841	180.443	0.0204	0.0204	-0.8	-0.2
	S_I		179.54	179.78	0.0155	0.0160	0.1	3.2
	A_P	8	146.748	139.183	0.0544	0.0724	-5.3	28.4
	M_L		132.335	140.538	0.0262	0.0260	6	-0.8
	S_I		146.748	159.078	0.0267	0.0288	8.1	7.5
	A_P	9	191.676	205.766	0.0204	0.0331	7.1	47.5
	M_L		190.125	205.488	0.0260	0.0424	7.8	48
	S_I		191.613	196.709	0.0170	0.0170	2.6	0.1

In order to study the generated differences in stresses and strains by neglecting the anisotropy, *relative difference* measurement is used. The *relative difference*, $d(\%)$, is a parameter defined to compare two numerical quantities as follow:

$$Relavtive\ Difference = d(\%) = \frac{|f_{aniso}| - |f_{iso}|}{\left(\frac{|f_{aniso}| + |f_{iso}|}{2}\right)} \times 100\ , \tag{5.4}$$

where f_{iso} and f_{aniso} are numerical quantities; and neither of f_{iso} and f_{aniso} can be considered the correct value. The *relative difference* with respect to "the average of isotropic and anisotropic results" was calculated for each virtual test using Equation (5.4). The positive values of *relative difference* show that anisotropic stresses or strains are larger than isotropic stresses or strains, and vice versa.

The maximum von Mises stresses and the absolute principal strains may significantly change when anisotropy is considered in comparison with isotropic models. The anisotropic model mostly results in larger maximum von Mises stresses. By considering

anisotropy, the maximum von Mises stress is increased up to 30.2% (Table 5.5, Table 5.6 and Table 5.7).

The maximum absolute principal strains vary from -50.1% to 48% in anisotropic model with respect to the isotropic model. In fifteen out of twenty seven virtual tests, a significant change in strains (more than 20% variation) takes place in the specimens by considering the anisotropy (Table 5.5, Table 5.6 and Table 5.7).

The largest difference between the anisotropic maximum von Mises stresses and the isotropic maximum von Mises stresses is in the femoral neck specimen (S3) and superior-inferior loading direction (Table 5.5). Figure 5.12 shows nodal elasticity moduli of the neck specimen (S3) in the plane of isotropy (or isotropic Young's modulus) and the axis of symmetry (density gradient) direction.

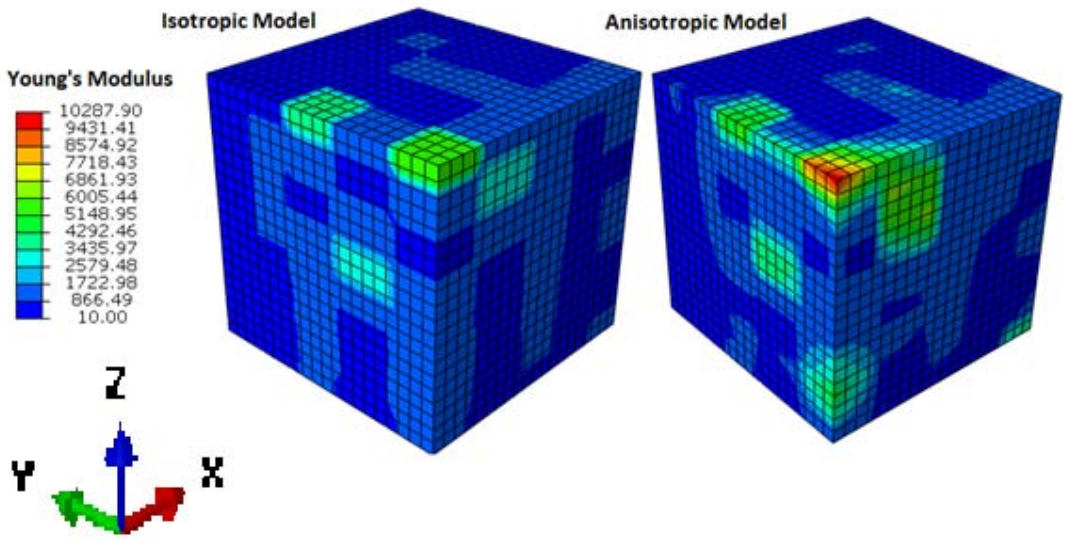

Figure 5.12: Nodal Young's modulus in the plane of isotropy (Isotropic) and the axis of symmetry (Anisotropic Model) directions in S3 specimen.

Nodal elasticity moduli in the plane of isotropy range from 10MPa to 5920MPa. They also range from 10MPa to 10288MPa in the direction of the axis of symmetry. The

difference between the isotropic and anisotropic von Mises stress is 5.7 MPa; and it is resulted in 30.2% difference as shown in Figure 5.13.

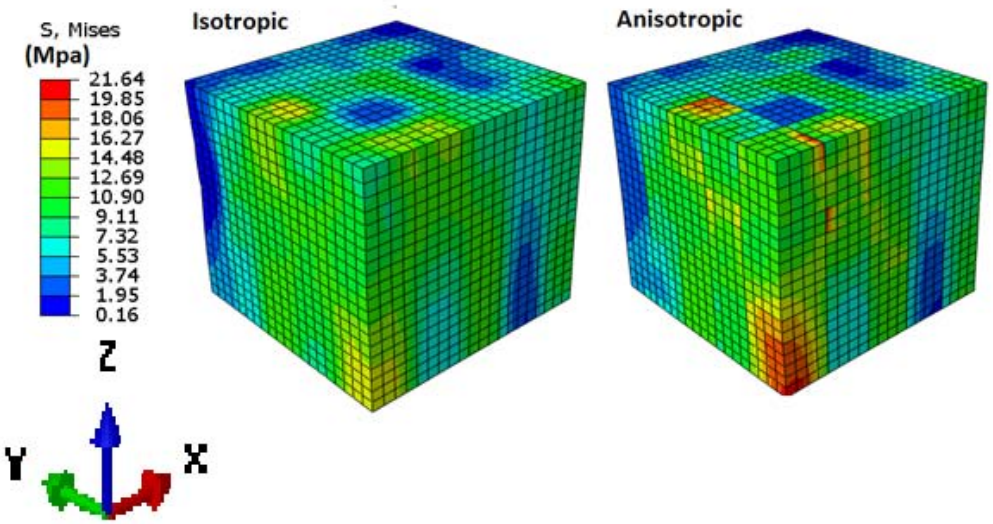

Figure 5.13: The maximum von Mises stress of the isotropic and anisotropic FE model of S3 specimen

The largest *relative difference* between the maximum absolute principal strains obtained from the anisotropic models and isotropic model is also found in the specimen (S3) in superior-inferior loading direction (Table 5.5). However, the FE nodes with the maximum von Mises stresses are different from the FE nodes with the maximum absolute principal strains as shown in Figure 5.13 and 5.14. The difference in the maximum absolute principal strain is 0.015, yielding 50.1% *relative difference* in the maximum absolute principal strain.

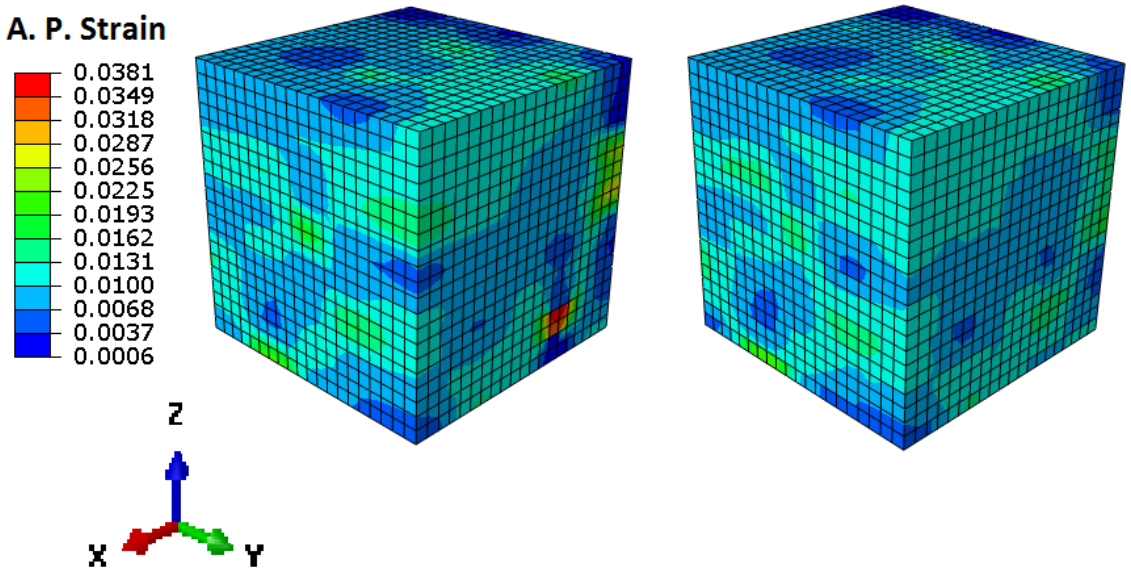

Figure 5.14: The maximum absolute principal strain of the isotropic and anisotropic FE model of S3 specimen

The virtual tests are divided to three groups based on the location of the specimens: femoral neck, intertrochanteric and subtrochanteric regions. The maximum, minimum and average values of *relative difference* for stresses are presented for each region of interest in Table 5.8. The maximum, minimum and average values of *relative difference* for strains are also presented for each region of interest in Table 5.9.

Table 5.8: Maximum , minimum and average *relative difference* of maximum von Mises stresses for different regions of interest.

von Mises stress	Region of Interest (d%)			
	Overall	Neck	Int.	Sub.
Maximum. d(%)	30.2	30.2	12.3	8.1
Minimum. d(%)	-5.3	-2.8	1.6	-5.3
Average d(%)	7.5	12.2	7.5	2.8

Table 5.9: Maximum , minimum and average *relative difference* of maximum absolute principal strain for different regions of interest.

Principal Strain	Region of Interest (d%)			
	Overall	Neck	Int.	Sub.
Maximum. d(%)	47.9	-6.1	39.2	47.95
Minimum. d(%)	-50.1	-50.1	-49.8	-0.8
Average d(%)	-4.9	-35.8	1.5	19.7

The *average of relative difference* was calculated from Equation (5.5). This parameter is defined to quantify an increase or a decrease in magnitude of the stresses or strains in a group of tests.

$$Average\ of\ Relative\ Difference = \overline{d(\%)} = \frac{\sum_1^n d(\%)}{n}, \quad (5.5)$$

where *n* is the number of specimens. The results (Table 5.8) show that the greatest overall increase in the maximum von Mises stresses is found in the femoral neck specimens.

The maximum absolute principal strain decreases in almost the half of the intertrochanteric virtual specimens using the anisotropic model in comparison with isotropic model (Table 5.5, Table 5.6 and Table 5.7). It contributes to a negligible value for the *average of relative difference* in the intertrochanteric specimens (Table 5.9). The maximum absolute principal strain increases up to 19.7% in the subtrochanteric specimens by considering the anisotropy. On the other hand, the maximum absolute principal strain is 35.8% lower in the neck specimens by considering the anisotropy (Table 5.9).

From another point of view, all the specimens are divided to two groups using their average density, cancellous and cortical bones (Table 5.10). The bone region with density less than 1.04 gcm^{-3} has been considered as cancellous bone [22, 26]. The region with density more than 1.04 gcm^{-3} has been considered as cortical bone [28].

Table 5.10: The specimens are categorized to cortical and cancellous bone based on the average bone density.

Spec. Nos.	S1	S2	S3	S4	S5	S6	S7	S8	S9
Average density (g/cm3)	0.59	0.34	0.60	0.79	1.08	1.56	1.76	1.44	1.93
Overall Bone Type	Can.	Can.	Can.	Can.	Can/Cor.	Cor.	Cor.	Cor.	Cor.

The *relative difference* was calculated for the virtual tests on cancellous and cortical samples as shown in Table 5.11. The results of the virtual tests show that both the maximum von Mises stress and the absolute principal strain increase in the cortical bone specimens using the anisotropic model compared with the isotropic model. However, in the cancellous bone specimens, the maximum von Mises stresses increase and the absolute principal strains decrease using the anisotropic model in comparison with the isotropic model. The results (Table 5.11) show that the changes in the mechanical behavior of cancellous and cortical bone by using the anisotropic FE models instead of the isotropic ones are not always the same [34-36].

Table 5.11: Maximum, minimum and average *relative difference* of maximum von Mises stresses and absolute principal strains in two groups of bone types.

	Bone Type			
	Cancellous		Cortical	
	von Mises	Principal Strain	von Mises	Principal Strain
Maximum. d(%)	30.2	-4.4	9.2	47.9
Minimum. d(%)	-2.8	-50.1	-5.3	-0.8
Average d(%)	10.25	-26.5	4.1	22.1

5.2.4 Accuracy Evaluation of the Anisotropic Versus the Isotropic FE models

The virtual compression tests were performed on three different FE models, Clinical CT isotropic, Coarse isotropic and Coarse anisotropic models of the small specimens. The small specimens were cut from neck, introchanteric, and subtrochanteric regions of femoral head. The maximum von Mises stresses and absolute principal strains of each FE analysis are presented in Figure 5.15.

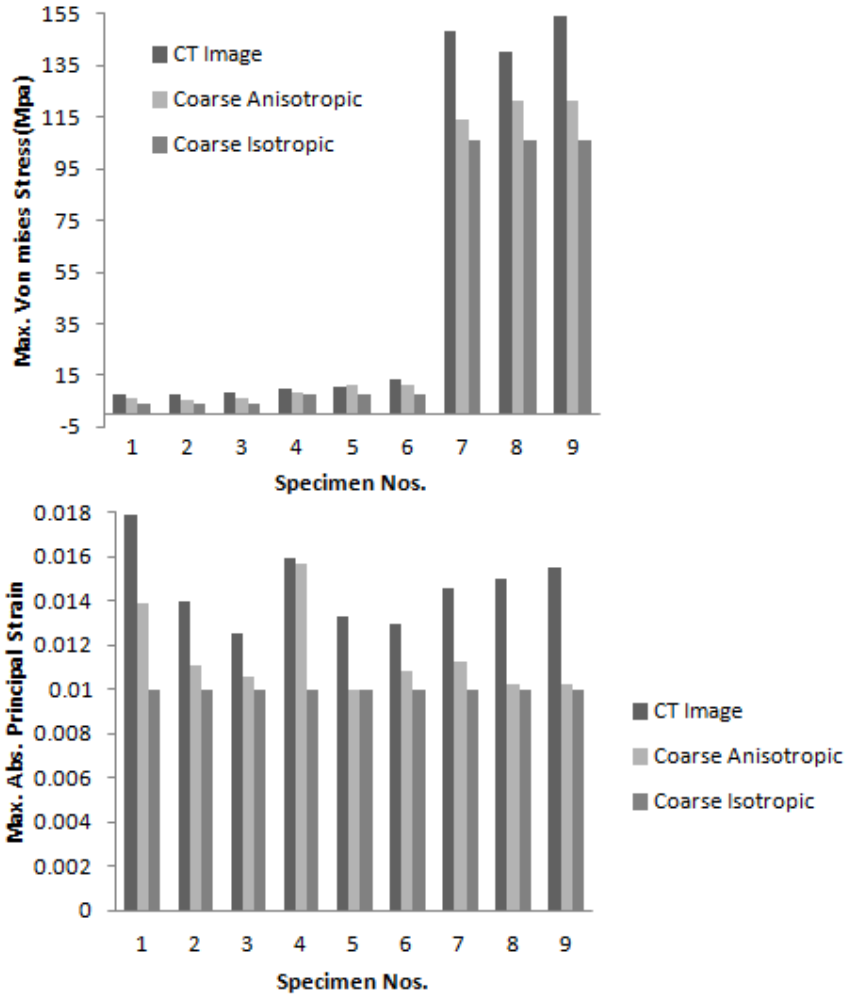

Figure 5.15: The maximum von Mises stress and absolute principal strain of nine FE analyses of three different small specimens.

The results of the analyses show that the differences between the results of Coarse FE models and Clinical CT FE models are reduced considering the anisotropic behavior. The maximum reduction of errors using the anisotropic model reaches to 27% in maximum von Mises stress and 36% in maximum absolute principal strain. The distribution of stresses or strains in the clinical isotropic models was also compared to coarse anisotropic models. The results show that the nodes with the largest stress or strain are in the same region for both the clinical isotropic and coarse anisotropic models. The obtained stresses

and strains distributions from both the clinical isotropic and coarse anisotropic FE analyses are also illustrated in Figure 5.16 and Figure 5.17, respectively.

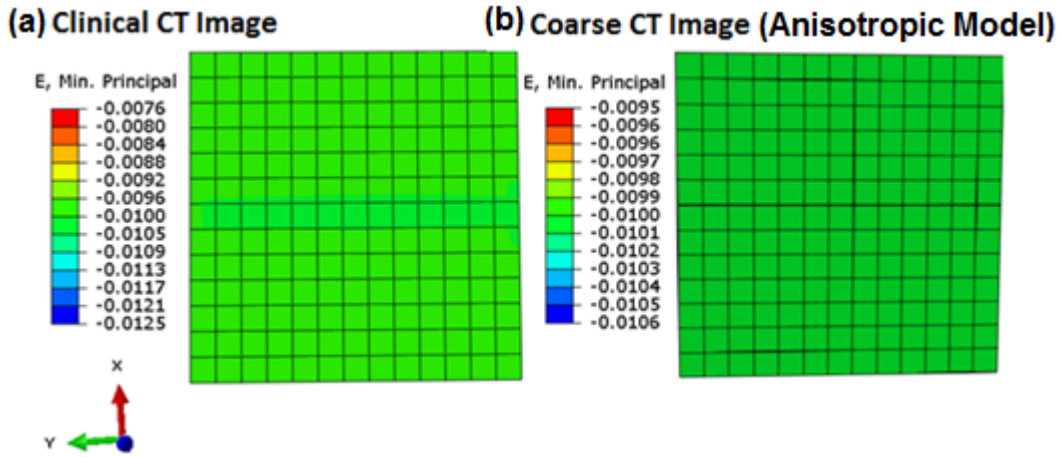

Figure 5.16: The maximum absolute principal strain distribution in the midsection of the small specimen cut from the femoral neck region.

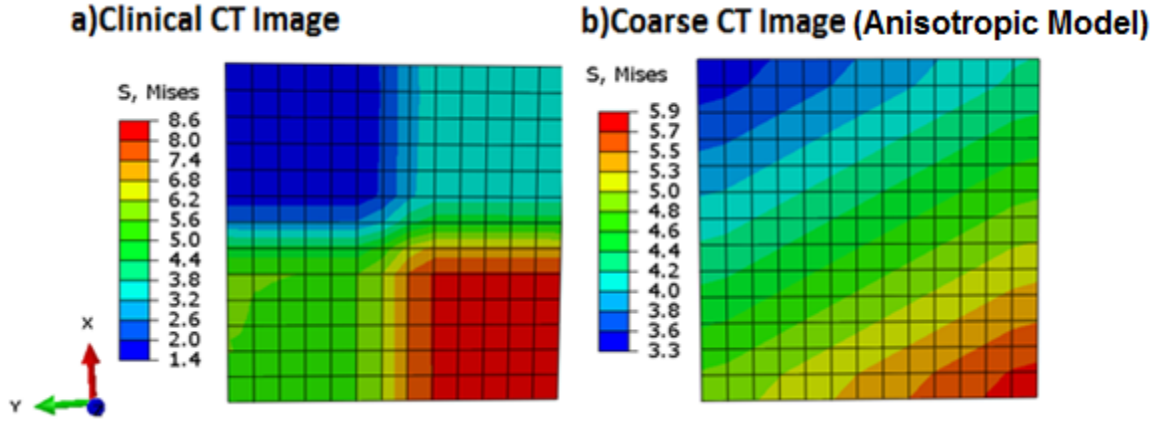

Figure 5.17: The maximum von Mises stress distribution in the midsection of the small specimen cut from the femoral neck region.

Therefore, the anisotropic FE model is more accurate to predict the magnitude and location of the maximum stresses and maximum absolute strains. It could be concluded that anisotropic FE models have more accuracy to predict the mechanical behavior of bone specimens in comparison with the conventional isotropic model.

5.3 Discussion

This section discusses the principal anisotropic directions and magnitudes in the bone specimens obtained from the density variation method. We have also compared the virtual tests results with the reported results in literature.

5.3.1 Principal Anisotropic Directions

Figure 5.3, 5.4 and 5.5 demonstrate that the most of the planes of isotropy were parallel to the bone surface in the proximity of bone surface in transverse section. It is evident from the aforementioned figures that the bone structures form rotated plywood [1] since the planes of isotropy could represent thin isotropic sheets of the plywood structure. In longitudinal sections, the planes of isotropy are mostly parallel to the femur neck axis in superior part of neck and it gradually deviates to bone shaft axis in inferior part of the neck (Figure 5.3). Similarly, majority of the planes of isotropy are parallel to the intertrochanteric line in the superior part of intertrochanteric region and it gradually orients to the axis of femur shaft in inferior part (Figure 5.4). In subtrochanteric region, the planes of isotropy are mostly aligned to the axis of femur shaft (Figure 5.5). Consequently, the results indicate that the principal anisotropic directions vary in different regions of femoral head. The results prove that considering the anisotropy axes parallel to the anatomical axes, i.e., the sagittal, coronal and axial axis, is oversimplified since the anatomical axes may considerably deviate from the actual principal anisotropic directions.

As the minimum density variation occurs in the orientations of trabecular structure, the orientations of the planes of isotropy (with minimum density variation) must follow the trabecular structure. According to wolff's law, trabecular pattern coincides with the directions of principal stresses. The directions of the planes of isotropy must also be aligned to the orientation of the principal stresses produced under physiological loading condition.

Figure 5.18(b) includes the radiographic scan of the proximal femur with highlighted trabecular groups, taken by San Antonie *et al*. [94]. The approximate locations of the specimens (red squares) and the directions of planes of isotropy (blue arrows) are depicted on Figures 5.18(a). The results show that the directions of planes of isotropy calculated from the density gradient approximately reproduce the trabecular structure.

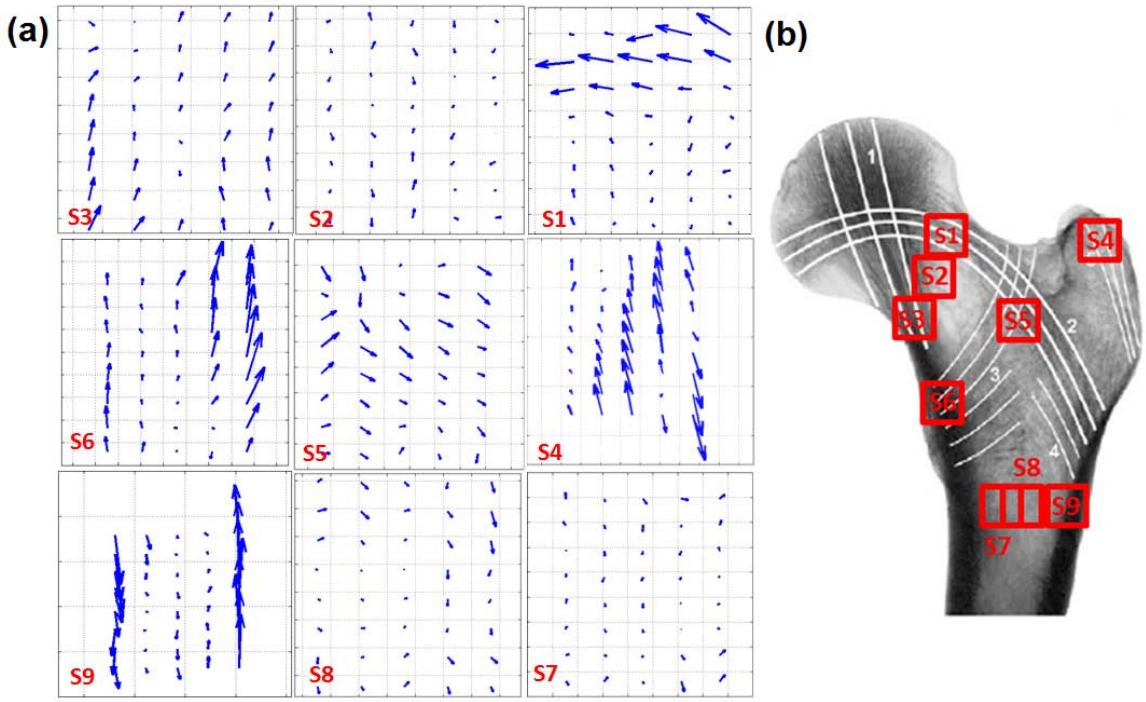

Figure 5.18: (a) Extension direction of planes of isotropy in frontal midsections of the bone specimens, which were produced using the density variation method. (b)The

radiographic scan of the proximal femur with highlighted trabecular groups taken by San Antonie et al.[94].

San Antonie *et al*. also used FE analysis to find the directions of the principal stresses produced by a physiological load scheme as shown in Figure 5.19(b) [94]. Figure 5.19(a) shows that the planes of isotropy are mostly follow the pattern of principal stress in frontal section of the femoral head.

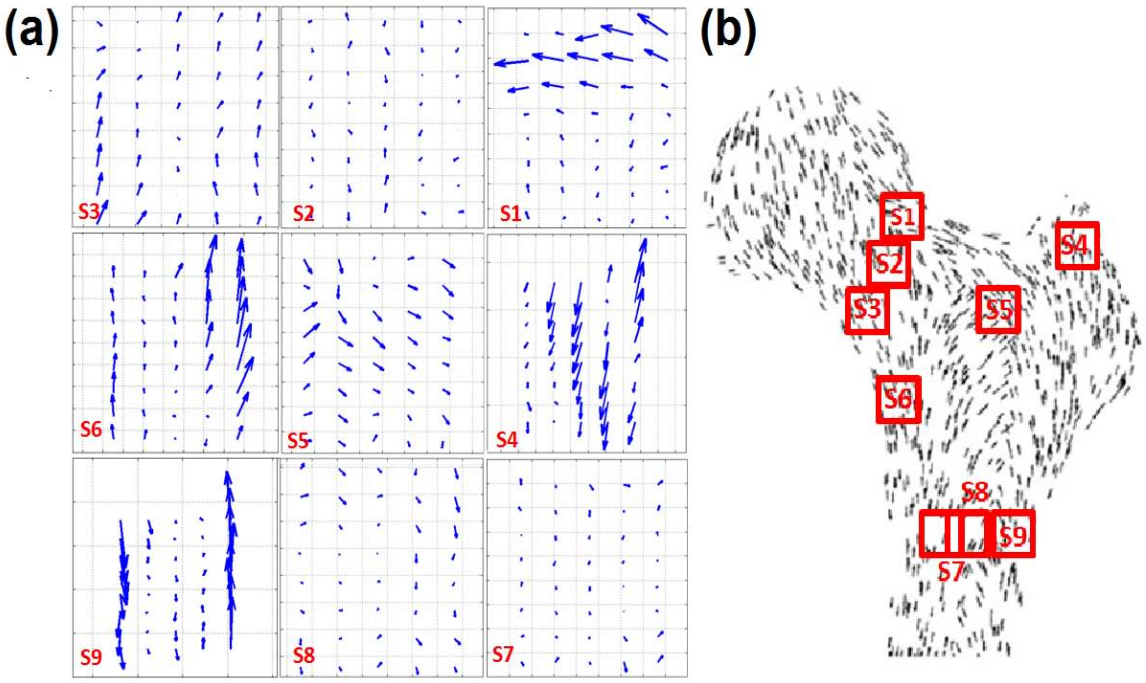

Figure 5.19: (a) The isotropic plane in frontal midsections of the bone specimens, which were produced using introduced method in this study. (a) The main principal stresses directions in a slice of femur model obtained by San Antonie et al.[94].

5.3.2 The Magnitudes of Young's Modulus

The results show that the nodal isotropic Young's modulus is highly varied in different nodes of the specimens (Table 5.2). Therefore, assignment of average Young's modulus to a specimen of bone could make significant errors in the FEA results.

In literature, anisotropic Young's moduli have been established as a function of bone density; and the variations of the anisotropic orientations have not been considered. However, the derived correlation in this study shows that the anisotropic Young's moduli are dependent on the voxel size, bone density and bone density gradient. Adding bone density gradient as an independent variable helps to consider the variations of the anisotropic orientations in the anisotropic elasticity constants.

5.3.3 The Virtual Compression Tests

The difference between anisotropic Young's moduli and isotropic Young's modulus is a result of the density gradient and the size of voxels. Since the voxel size is constant in all virtual tests, the density gradient is the only effective parameter in this study. As the density gradients were larger in introchanteric and femoral neck regions compared with subtrochanteric specimens (Table 5.3), the differences between the results of the anisotropic and isotropic FE analyses are also larger in the neck and intertrochanteric specimens in comparison with subtrochanteric specimens (Table 5.8 and Table 5.9). The large differences between the results of the anisotropic and isotropic FE analyses on the specimen (S3) underline that the anisotropy could significantly have influenced on the results of stress and strain prediction.

Significant amount of error reduction by using "Coarse anisotropic model" instead of "Coarse isotropic model" justifies the performance improvement of the anisotropic FE model in comparison with the conventional isotropic model (Figure 5.15).

The results show that the differences between the anisotropic and isotropic stresses are lower than the differences between the anisotropic and isotropic maximum strains as

shown in Table 5.8 and 5.9. The observed differences between anisotropic and isotropic nodal strains are originated from the differences in the elastic constants when both the anisotropic and isotropic models undergo the same loading condition. The strains obtained by the anisotropic models are higher than the isotropic models if effective elastic constants of the anisotropic models are lower. Conversely, the strains obtained by the isotropic models are higher than the anisotropic models if the effective elastic constants of the isotropic models are lower. In brief, strain is lower for higher effective elastic constants and vice-versa. As stress values are resulted from the production of strain and Young's modulus, the differences between the anisotropic and isotropic stresses are smaller compared to strains.

The anisotropy increases maximum stresses and strains in the small specimens which are made of one voxel (Figure 5.15). The boundary conditions are the same in the both isotropic and anisotropic models. The results show that the anisotropic maximum stresses or strains are higher than the isotropic ones if the boundary conditions are the same in the both models. However, the effect of anisotropy on the both maximum stresses and strains are different in the specimens with the size of actual compression tests. As these specimens are made of two hundred voxels, the boundary conditions are not the same in the corresponding voxels in the both isotropic and anisotropic models. In the cortical bone specimens with the size of actual compression tests, both the maximum stress and the strain increase by using the anisotropic model in comparison with isotropic model. However, in the cancellous bone specimens, the maximum stress increases and the strain decreases by using the anisotropic model compared with the isotropic model (Table 5.11). It may result in the higher effects of anisotropy in the boundary conditions of the

corresponding voxels in the both models in cancellous bone in comparison with the cortical bone due to the higher magnitude of the density gradient in cancellous bone.

Different studies have been conducted to compare the principal stresses and strains of the anisotropic model with the isotropic 3D FE models in different regions of body skeleton. Au AG *et al*. compared the anisotropic 3D FE models of an implanted tibial knee with physiologically representative loading conditions of the isotropic model [36]. They predicted higher cancellous bone stresses and lower cortical bone stresses for anisotropic bone models in comparison with isotropic bone models. Nevertheless, the results of 3D FE models of an implanted mandible with the isotropic bone predicted higher maximal stress and lower maximal strain values in both cortical and cancellous bones compared with the anisotropic models [35]. In another study, Mahony *et al*. showed that transverse isotropic elasticity of implanted mandible bones increased the maximal principal stresses from 20% to 30% in the cortical crests [34]. Hence, the different changes in the mechanical behavior of cancellous and cortical bone using the anisotropic FE models in comparison with the isotropic FE models have been also reported in different literature.

Based on the convergence tests performed in this study, both the anisotropic and the isotropic FE models converged at 8000 FE elements. Therefore, the consideration of anisotropy could not significantly influence on the computational operation since the number of FE elements is the most effective parameters in the computational cost of FEA [37]. Consequently, the anisotropic FEA in comparison with the isotropic FEA could increase the accuracy of the results without considerable increase in the computational operations.

Chapter 6

Conclusions and Future Work

This research introduced a method for constructing anisotropic bone FE models from CT images. The principal anisotropic directions were determined; and the empirical correlation between bone density and elasticity modulus in principal anisotropic directions was modified by the incorporation of the density gradient. The combination of the techniques to find the principal anisotropic directions and the modified correlation has resulted in a new anisotropic model of bone material. Then, a method was introduced to assign the anisotropic material properties to finite element models in Abaqus. Finally, fifty four finite element models were generated from both the anisotropic and the conventional isotropic material models. The obtained stresses and strains distributions using both material models were then recorded and discussed.

6.1 Contributions of the research

The major contributions of the current study can be stated as follows:

- Gradient of bone density is introduced as an effective parameter to describe anisotropic material properties of bone. The bone density gradient has been used to determine the principal anisotropic directions of both cortical and cancellous bones.
- Each point of bone possesses one axis of symmetry parallel to density gradient and a plane of isotropy at right angles to this axis. Since each point has independent bone density gradient, assignment of pointwise transversely isotropic type of anisotropy to bone material has been justified.
- The study shows that the principal anisotropic directions are varied in different regions of femoral head. Therefore, considering anisotropic directions parallel to anatomical axes – sagittal, coronal and axial axis – is oversimplified.
- Existing empirical functions that correlate bone isotropic Young's modulus and bone density are improved by incorporating information of the bone density gradient. The improved correlation is applied to calculate Young's moduli along the plane of isotropy and the axes of symmetry.
- The voxel size and the density gradient are two independent parameters which differentiate the anisotropic and isotropic Young's modulus of bone material. Therefore, the difference between the anisotropic and isotropic Young's modulus increases in femoral neck and intertrochanteric regions, having large variation of bone density. The difference reduces in subtrochanteric region, a bone region with a low variation of bone density. The errors generated due to the neglecting of

anisotropy are also expected to be reduced by increasing the resolution of the CT images and vice versa.

- Results of the virtual compression tests on the large specimens (with the size of actual compression tests) show that pointwise anisotropy could significantly change the maximum predicted stresses and strains. The maximum von Mises stresses obtained from finite element analysis are mostly larger in the anisotropic model than the isotropic model. Hence, it is more conservative and reasonable to consider anisotropy in order to predict femur fracture.
- The results of the virtual compression tests on the small specimens constructed from the coarse CT image show that the anisotropic model improves the accuracy of the results of finite element analysis.
- Based on the convergence tests performed in this study, the consideration of anisotropy could not significantly influence on the computational operation since the number of FE elements is the most effective parameters in the computational cost of the FEA.
- Based on wolff's law, the rate of bone remodeling and adaptation depend on the magnitude of applied stresses or strains. Therefore, relative errors between the anisotropic and the isotropic stresses or strains decrease the validity of bone remodeling prediction. Hence, bone anisotropy should be considered in finite element model of bones to achieve precise description of the bone mechanical behavior.

In conclusion, this study focuses on determination of bone material properties and construction of the bone anisotropic finite element model from Computed Tomography (CT) scans. The results of this research show that neglecting the anisotropic property of bone could underestimate fracture risk and decrease the validity of bone remodelling process under physiological loading condition.

6.2 Future Work

The precise definition of bone material properties is a prerequisite to predict the bone remodeling and fragility. Hence, the need to improve techniques to describe *in-vivo* bone anisotropic and heterogeneous material properties has received a significant attention. Although there is a good agreement between the results of this study and the findings of previous researches, there are several pathways as potential future works to improve current mechanical model of bones. In the following paragraphs, the suggested future works are discussed.

- To achieve more comprehensive results, 3D finite element model of *in-vivo* femoral head will be generated from CT image of *in-vivo* bone. Then, pointwise anisotropic material properties will be assigned to femoral head. Results of the finite element analysis will be compared with results of isotropic model of femoral head under physiological loading condition.
- The design of a process to automatically separate femoral head from pelvis and surrounded soft tissue is a prerequisite for creating the finite element model of

femoral head. Therefore, a precise method is required to be developed to isolate femoral head CT data from other parts.

- In this study, the anisotropic elasticity matrix has been defined in the local material coordinate system due to the restriction of Abaqus software. However, the definition of elasticity matrix with twenty one independent field variables would be an alternative way to assign pointwise anisotropic material properties to the finite element model. Therefore, a possible method to assign the elasticity matrix with twenty one independent field variables can be developed in future.
- In this study, the empirical correlation between bone elasticity modulus and bone density has been revised and the dimension of bone density gradient is also incorporated as an independent variable. Effects of the density gradient on the existing elasticity–density correlation would be validated by performing statistically significant numbers of standard mechanical tests on actual bone specimens.

Bibliography

1. Yuehuei H. An, M.D. and D.S. Robert A. Draughn, *Mechanical Testing of Bone and the Bone–Implant Interface*, ed. M.D. Yuehuei H. An and D.S. Robert A. Draughn. 1999: 2000 CRC Press LLC.
2. Middleton, J., M. Jones, and A. Wilson, *The role of the periodontal ligament in bone modeling: The initial development of a time-dependent finite element model.* American Journal of Orthodontics and Dentofacial Orthopedics, 1996. **109**(2): p. 155-162.
3. Kitamura, E., et al., *Biomechanical aspects of marginal bone resorption around osseointegrated implants: considerations based on a three-dimensional finite element analysis.* Clinical Oral Implants Research, 2004. **15**(4): p. 401-412.
4. Sevimay, M., et al., *Three-dimensional finite element analysis of the effect of different bone quality on stress distribution in an implant-supported crown.* The Journal of Prosthetic Dentistry, 2005. **93**(3): p. 227-234.
5. Mueller, T.L., et al., *Computational finite element bone mechanics accurately predicts mechanical competence in the human radius of an elderly population.* Bone. **48**(6): p. 1232-1238.
6. Hart, R.T., et al., *Modeling the biomechanics of the mandible: A three-dimensional finite element study.* Journal of Biomechanics, 1992. **25**(3): p. 261-286.
7. Jacobs, C.R., et al., *Numerical instabilities in bone remodeling simulations: The advantages of a node-based finite element approach.* Journal of Biomechanics, 1995. **28**(4): p. 449-459.
8. Keyak, J.H., et al., *Automated three-dimensional finite element modelling of bone: a new method.* Journal of Biomedical Engineering, 1990. **12**(5): p. 389-397.

9. Adachi, T., et al., *Trabecular Surface Remodeling Simulation for Cancellous Bone Using Microstructural Voxel Finite Element Models.* Journal of Biomechanical Engineering, 2001. **123**(5): p. 403-409.
10. Levenston, M.E., et al., *Computer simulations of stress-related bone remodeling around noncemented acetabular components.* The Journal of Arthroplasty, 1993. **8**(6): p. 595-605.
11. Gundersen, H.J.G. and E.B. Jensen, *Stereological estimation of the volume-weighted mean volume of arbitrary particles observed on random sections.* Journal of Microscopy, 1985. **138**(2): p. 127-142.
12. Cowin, S.C., *The relationship between the elasticity tensor and the fabric tensor.* Mechanics of Materials, 1985. **4**(2): p. 137-147.
13. Kabel, J., et al., *Constitutive relationships of fabric, density, and elastic properties in cancellous bone architecture.* Bone, 1999. **25**(4): p. 481-486.
14. Moreno, R., M. Borga, and O. Smedby, *Generalizing the mean intercept length tensor for gray-level images.* Medical Physics. **39**(7): p. 4599-4612.
15. Odgaard, A., E.B. Jensen, and H.J.G. Gundersen, *Estimation of structural anisotropy based on volume orientation. A new concept.* Journal of Microscopy, 1990. **157**(2): p. 149-162.
16. Odgaard, A., et al., *Fabric and elastic principal directions of cancellous bone are closely related.* Journal of biomechanics, 1997. **30**(5): p. 487-495.
17. Tabor, Z.a. and E. Rokita, *Quantifying anisotropy of trabecular bone from gray-level images.* Bone, 2007. **40**(4): p. 966-972.
18. Tabor, Z.a., *Estimating structural properties of trabecular bone from gray-level low-resolution images.* Medical engineering & physics, 2007. **29**(1): p. 110-119.
19. Inglis, D. and S. Pietruszczak, *Characterization of anisotropy in porous media by means of linear intercept measurements.* International Journal of Solids and Structures, 2003. **40**(5): p. 1243-1264.
20. Goulet, R.W., et al., *The relationship between the structural and orthogonal compressive properties of trabecular bone.* Journal of biomechanics, 1994. **27**(4): p. 375-389.
21. Lotz, J.C., T.N. Gerhart, and W.C. Hayes, *Mechanical Properties of Trabecular Bone from the Proximal Femur: A Quantitative CT Study.* Journal of Computer Assisted Tomography, 1990. **14**(1): p. 107-114.

22. Lotz, J.C., T.N. Gerhart, and W.C. Hayes, *Mechanical properties of metaphyseal bone in the proximal femur.* Journal of Biomechanics, 1991. **24**(5): p. 317-329.
23. Ashman, R.B., J.Y. Rho, and C.H. Turner, *Anatomical variation of orthotropic elastic moduli of the proximal human tibia.* Journal of Biomechanics, 1989. **22**(8): p. 895-900.
24. Ashman, R.B.a.R., J.Y.,, *Elastic moduli of trabecular bone material.* J. Biomech., 1988. **21**: p. 177.
25. Rho, J.-Y., *An ultrasonic method for measuring the elastic properties of human tibial cortical and cancellous bone.* Ultrasonics, 1996. **34**(8): p. 777-783.
26. Rho, J.Y., Hobatho, M. C.,Ashman, R. B., *Relations of mechanical properties to density and CT numbers in human bone.* Medical Engineering & Physics, 1995. **17**(5): p. 347-355.
27. Rho, J.Y., R.B. Ashman, and C.H. Turner, *Young's modulus of trabecular and cortical bone material: Ultrasonic and microtensile measurements.* Journal of biomechanics, 1993. **26**(2): p. 111-119.
28. Rho, J.-Y., L. Kuhn-Spearing, and P. Zioupos, *Mechanical properties and the hierarchical structure of bone.* Medical engineering & physics, 1998. **20**(2): p. 92-102.
29. Roberts, S.G., et al., *Noninvasive determination of bone mechanical properties using vibration response: A refined model and validation in vivo.* Journal of Biomechanics, 1996. **29**(1): p. 91-98.
30. Ashman, R.B., et al., *A continuous wave technique for the measurement of the elastic properties of cortical bone.* Journal of Biomechanics, 1984. **17**(5): p. 349-361.
31. Ciarelli, M.J., et al., *Evaluation of orthogonal mechanical properties and density of human trabecular bone from the major metaphyseal regions with materials testing and computed tomography.* Journal of Orthopaedic Research, 1991. **9**(5): p. 674-682.
32. Goldstein, S.A., *The mechanical properties of trabecular bone: Dependence on anatomic location and function.* Journal of Biomechanics, 1987. **20**(11â€“12): p. 1055-1061.
33. Homminga, J., et al., *Cancellous bone mechanical properties from normals and patients with hip fractures differ on the structure level, not on the bone hard tissue level.* Bone, 2002. **30**(5): p. 759-764.
34. O'Mahony, A.M., J.L. Williams, and P. Spencer, *Anisotropic elasticity of cortical and cancellous bone in the posterior mandible increases peri-implant stress and strain under oblique loading.* Clinical Oral Implants Research, 2001. **12**(6): p. 648-657.

35. Bonnet, A.S., M. Postaire, and P. Lipinski, *Biomechanical study of mandible bone supporting a four-implant retained bridge: Finite element analysis of the influence of bone anisotropy and foodstuff position.* Medical Engineering & Physics, 2009. **31**(7): p. 806-815.

36. Au, A.G., et al., *A parametric analysis of fixation post shape in tibial knee prostheses.* Medical Engineering & Physics, 2005. **27**(2): p. 123-134.

37. Peng, L., et al., *Comparison of isotropic and orthotropic material property assignments on femoral finite element models under two loading conditions.* Medical Engineering & Physics, 2006. **28**(3): p. 227-233.

38. Feldkamp, L.A., et al., *The direct examination of three-dimensional bone architecture in vitro by computed tomography.* Journal of Bone and Mineral Research, 1989. **4**(1): p. 3-11.

39. Lang, T.F., et al., *Volumetric quantitative computed tomography of the proximal femur: Precision and relation to bone strength.* Bone, 1997. **21**(1): p. 101-108.

40. Genant, H.K., et al., *Quantitative Computed Tomography of Vertebral Spongiosa: A Sensitive Method for Detecting Early Bone Loss After Oophorectomy.* Annals of Internal Medicine, 1982. **97**(5): p. 699-705.

41. Bundy, K.J., *Experimental studies of the nonuniformity and anisotropy of human cortical bone*. 1974, Stanford University.

42. Hodgskinson, R. and J.D. Currey, *Young's modulus, density and material properties in cancellous bone over a large density range.* Journal of Materials Science: Materials in Medicine, 1992. **3**(5): p. 377-381.

43. Helgason, B., et al., *Mathematical relationships between bone density and mechanical properties: A literature review.* Clinical biomechanics (Bristol, Avon), 2008. **23**(2): p. 135-146.

44. Shahar, R., et al., *Anisotropic Poisson's ratio and compression modulus of cortical bone determined by speckle interferometry.* Journal of biomechanics, 2007. **40**(2): p. 252-264.

45. Orías, A.A.E., *the relationship between the mechanical anisotropy of human cortical bone tissue and its microstructure*, in *Aerospace and Mechanical Engineering*. 2005, University of Notre Dame: Notre Dame. p. 1-13.

46. Katz and J.L., *Anisotropy of Young's modulus of bone.* Nature, 1980. **283**.

47. Morgan, E.F., H.H. Bayraktar, and T.M. Keaveny, *Trabecular bone modulus-density relationships depend on anatomic site.* Journal of Biomechanics, 2003. **36**(7): p. 897-904.

48. Whitehouse, W.J., *The quantitative morphology of anisotropic trabecular bone.* Journal of Microscopy, 1974. **101**(2): p. 153-168.

49. Smit, Schneider, and Odgaard, *Star length distribution: a volume-based concept for the characterization of structural anisotropy.* Journal of Microscopy, 1998. **191**(3): p. 249-257.

50. Sasaki, N., et al., *Orientation of bone mineral and its role in the anisotropic mechanical properties of bone Transverse anisotropy.* Journal of biomechanics, 1989. **22**(2): p. 157-164.

51. Harrigan, T.P. and R.W. Mann, *Characterization of microstructural anisotropy in orthotropic materials using a second rank tensor.* Journal of Materials Science, 1984. **19**(3): p. 761-767.

52. Raegsegger, P., B. Koller, and R. MAller, *A microtomographic system for the nondestructive evaluation of bone architecture.* Calcified Tissue International, 1996. **58**(1): p. 24-29.

53. Laib, A., et al., *3D micro-computed tomography of trabecular and cortical bone architecture with application to a rat model of immobilisation osteoporosis.* Medical and Biological Engineering and Computing, 2000. **38**(3): p. 326-332.

54. Martin Badosa, E., et al., *A method for the automatic characterization of bone architecture in 3D mice microtomographic images.* Computerized Medical Imaging and Graphics, 2003. **27**(6): p. 447-458.

55. Schneider, R., et al., *Inhomogeneous, orthotropic material model for the cortical structure of long bones modelled on the basis of clinical CT or density data.* Computer Methods in Applied Mechanics and Engineering, 2009. **198**(27): p. 2167-2174.

56. Bower, A.F., *Applied Mechanics of Solids.* 2012.

57. Sansalone, V., et al., *Determination of the heterogeneous anisotropic elastic properties of human femoral bone: From nanoscopic to organ scale.* Journal of Biomechanics. **43**(10): p. 1857-1863.

58. Kennedy, J.G. and D.R. Carter, *Long Bone Torsion: I. Effects of Heterogeneity, Anisotropy and Geometric Irregularity.* Journal of Biomechanical Engineering, 1985. **107**(2): p. 183-188.

59. Zysset, P.K., et al., *Elastic modulus and hardness of cortical and trabecular bone lamellae measured by nanoindentation in the human femur.* Journal of biomechanics, 1999. **32**(10): p. 1005-1012.

61. Ashman, R.B., *Ultrasonic Determination of the Elastic Properties of Cortical Bone: Techniques and Limitations*. 1982: Tulane University.

62. Hirsch, C.a.S., *The effect of orientation on some mechanical properties of femoral cortical specimens.* Acta Orthop. Scand, 1967: p. 38, 45.

63. Turner, C.H., A. Chandran, and R.M.V. Pidaparti, *The anisotropy of osteonal bone and its ultrastructural implications.* Bone, 1995. **17**(1): p. 85-89.

64. Weiner, S., T. Arad, and W. Traub, *Crystal organization in rat bone lamellae.* FEBS Letters, 1991. **285**(1): p. 49-54.

65. Turner, C.H., *On Wolff's law of trabecular architecture.* Journal of biomechanics, 1992. **25**(1): p. 1-9.

66. Odgaard, A., *Three-dimensional methods for quantification of cancellous bone architecture.* Bone, 1997. **20**: p. 315.

67. Goldstein, S.A., Goulet, R., and McCubbrey, D.,, *Measurement and significance of three-dimensional architecture to the mechanical integrity of trabecular bone.* Calcif. Tissue Int., 1993. **53**: p. S127.

68. Kabel, J., Odgaard, A., van Rietbergen, B., and Huiskes, R.,, *Connectivity and the elastic properties of cancellous bone.* Bone, 1999. **24**: p. 115.

69. Vahey, J.W., Lewis, J.L., and Vanderby, R., Jr.,, *Elastic moduli, yield stress, and ultimate stress of cancellous bone in the canine proximal femur.* J. Biomech., 1987: p. 20, 29.

70. Galante, J., Rostoker, W., and Ray, R.D.,, *Physical properties of trabecular bone.* Calcif. Tissue Res., 1970. **5**: p. 236.

71. Njeh, C.F., Hodgskinson, R., Currey, J.D., and Langton, C.M.,, *Orthogonal relationships between ultrasonic velocity and material properties of bovine cancellous bone.* Med. Eng. Phys., 1996. **18**: p. 373.

72. *What is Computed Tomography?*, Available from: http://www.fda.gov/radiation-emittingproducts/radiationemittingproductsandprocedures/medicalimaging/medicalx-rays/ucm115318.htm.

73. Barou, O., et al., *High-Resolution Three-Dimensional Micro-Computed Tomography Detects Bone Loss and Changes in Trabecular Architecture Early: Comparison with DEXA and Bone Histomorphometry in a Rat Model of Disuse Osteoporosis.* Investigative Radiology, 2002. **37**(1): p. 40-46.

74. Weiner, S., W. Traub, and H.D. Wagner, *Lamellar Bone: Structural Function Relations.* Journal of Structural Biology, 1999. **126**(3): p. 241-255.

75. Ketcham, R.A. and T.M. Ryan, *Quantification and visualization of anisotropy in trabecular bone.* Journal of Microscopy, 2004. **213**(2): p. 158-171.

76. Lespessailles, E., et al., *Imaging techniques forÂ evaluating bone microarchitecture.* Joint Bone Spine, 2006. **73**(3): p. 254-261.

77. Smit, T.H., *The Mechanical Significance of the Trabecular Bone Architecture in a Human Vertebra*. 1996: Shaker Verlag.

78. Smit, T.H., A. Odgaard, and E. Schneider, *Structure and Function of Vertebral Trabecular Bone.* Spine, 1997. **22**(24): p. 2823-2833.

79. Fondrik, M., Bahniuk, E., Davy, D.T., and Michaels, C., Some, *Some viscoelastic characteristics of bovine and human cortical bone.* J. Biomech, 1988. **21**: p. 623.

80. Reilly, S.B., Burstein, A.H., and Frankel, V.H., *The elastic modulus of bone.* J. Biomech., 1974. **7**: p. 271.

81. Taylor, W.R., et al., *Determination of orthotropic bone elastic constants using FEA and modal analysis.* Journal of Biomechanics, 2002. **35**(6): p. 767-773.

82. Williams, J.L. and W.J.H. Johnson, *Elastic constants of composites formed from PMMA bone cement and anisotropic bovine tibial cancellous bone.* Journal of Biomechanics, 1989. **22**(6): p. 673-682.

83. Van Rietbergen, B., et al., *Relationships between bone morphology and bone elastic properties can be accurately quantified using high-resolution computer reconstructions.* Journal of Orthopaedic Research, 1998. **16**(1): p. 23-28.

84. *Bone cement fatigue ASTM F2118 / ISO 16402.* ENDOLAB.

85. Helgason, B., et al., *A modified method for assigning material properties to FE models of bones.* Medical Engineering & Physics, 2008. **30**(4): p. 444-453.

86. Turner, C.H., Cowin, S.C., *Errors induced by off-axis measurement of the elastic properties of bone.* J. Biomech., 1988. **110**: p. 213–215.

87. Baca, V., et al., *Comparison of an inhomogeneous orthotropic and isotropic material models used for FE analyses.* Medical Engineering & Physics, 2008. **30**(7): p. 924-930.

88. Atkinson, K. and W. Han, *Finite Difference Method*, in *Theoretical Numerical Analysis*. 2009, Springer New York. p. 253-275.

89. Baca, V. and Z. Horak, *Comparison of isotropic and orthotropic material property assignments on femoral finite element models under two loading conditions.* Medical Engineering & Physics, 2007. **29**(8): p. 935.

90. A.I.Lurie, *Foundation of Engineering Mechanics (Theory of Elasticity).* 2005: Springer.

91. Simkin, A. and G. Robin, *The mechanical testing of bone in bending.* Journal of biomechanics, 1973. **6**(1): p. 31-39.

92. Hvid, I. and S.L. Hansen, *Trabecular bone strength patterns at the proximal tibial epiphysis.* Journal of Orthopaedic Research, 1985. **3**(4): p. 464-472.

93. Keller, T.S., *Predicting the compressive mechanical behavior of bone.* Journal of biomechanics, 1994. **27**(9): p. 1159-1168.

94. San Antonio, T., et al., *Orientation of orthotropic material properties in a femur FE model: A method based on the principal stresses directions.* Medical Engineering & Physics. **34**(7): p. 914-919.